INFLUENCE OF INELASTIC PHENOMENA ON THE ACTUATION CHARACTERISTICS OF HIGH TEMPERATURE SHAPE MEMORY ALLOYS

A Dissertation

by

PARIKSHITH K. KUMAR

Submitted to the Office of Graduate Studies of
Texas A&M University
in partial fulfillment of the requirements for the degree of

DOCTOR OF PHILOSOPHY

December 2009

Major Subject: Materials Science and Engineering

INFLUENCE OF INELASTIC PHENOMENA ON THE ACTUATION CHARACTERISTICS OF HIGH TEMPERATURE SHAPE MEMORY ALLOYS

A Dissertation

by

PARIKSHITH K. KUMAR

Submitted to the Office of Graduate Studies of
Texas A&M University
in partial fulfillment of the requirements for the degree of

DOCTOR OF PHILOSOPHY

Approved by:

Chair of Committee,	Dimitris C. Lagoudas
Committee Members,	Ibrahim Karaman
	Amine Benzerga
	Karl Hartwig
Intercollegiate Faculty Chair,	Tahir Cagin

December 2009

Major Subject: Materials Science and Engineering

ABSTRACT

Influence of Inelastic Phenomena on the Actuation
Characteristics of High Temperature Shape Memory Alloys. (December 2009)
Parikshith K. Kumar, B.E., Madras University;
M.S., Texas A&M University
Chair of Advisory Committee: Dr. Dimitris C. Lagoudas

Most efforts on High Temperature Shape Memory Alloys (HTSMAs), have focused on improving their work characteristics by thermomechanical treatment methods. However, the influence of transformation induced plasticity (TRIP) and viscoplasticity during actuation has not been studied. The objective of this dissertation work was to study the influence of plasticity and viscoplasticity on the transformation characteristics that occur during two common actuation-loading paths in TiPdNi HTSMAs. Thermomechanical tests were conducted along different loading paths. The changes in the transformation temperature, actuation strain and irrecoverable strain during the tests were monitored. Transmission Electron Microscopy (TEM) studies were also conducted on select test specimens to understand the underlying microstructural changes.

The study revealed that plasticity, which occurs during certain actuation load paths, alters the transformation temperatures and/or the actuation strain depending on the loading path chosen. The increase in the transformation temperature and the irrecoverable strain at the end of the loading path indicated that the rate independent irrecoverable strain results in the generation of localized internal stresses. The increased transformation temperatures were mapped with an equivalent stress (which corresponds to an internal stress) using the as-received material's transformation phase diagram. A trend for the equivalent internal stress as a function of the

applied stress and accumulated plastic strain was established. Such a function can be implemented into thermomechanical models to more accurately capture the behavior of HTSMAs during cyclic actuation.

On the contrary, although the viscoplastic strain generated during the course of constant stress thermal actuation could significantly reduce actuation strain depending on the heating/cooling rate. Additional thermomechanical and microstructural tests revealed no significant change in the transformation behavior after creep tests on HTSMAs. Comparing the thermomechanical test results and TEM micrographs from different cases, it was concluded that creep does not alter the transformation behavior in the HTSMAs, and any change in the transformation behavior can be attributed to the retained martensite which together with TRIP contributes to the rate independent irrecoverable strain. As a consequence, a decrease in the volume fraction of the martensite contributing towards the transformation must be considered in the modeling.

To my teachers, family and friends who have inspired and supported me till this stage

ACKNOWLEDGMENTS

I would like to thank the committee, the Department of Materials Science and Engineering and funding agencies, Schlumberger and NASA Glenn for supporting my studies and research while attending Texas A&M University. I am deeply indebted to my advisor, Dr. Dimitris C. Lagoudas, who inspired, guided and encouraged me to high standards and saw to it that I completed my requirements. He has taught me many virtues on life and research, which I hold dearly. I would also like to thank Dr. Ibrahim Karaman for the interesting and useful discussions, insight and recommendations during the course of my Ph.D. work. Special thanks to Dr. Zhiping Luo for his help with the Electron Microscopy.

I would also like to thank my colleagues, Darren J. Hartl, Bjoern Kiefer, Luciano Machado, Gary Seidel, Brent Volk, Francis Phillips, Olivier Bertachinni, George Chatzegeorgiou, Justin Schick, Piyush Thakre, Amnay Awasthi and Uri Desai, who have been an incredibly supportive, a source of inspiration, comfort and a family away from my home all through these years. I would specially like to thank Darren Hartl, who has been with me all these years as a friend and colleague whose company I have absolutely enjoyed. I would also like to thank Rodney Inmon, who was always available to provide assistance with equipment, machining and supplies. He has been a great friend and of incredible help through these years.

Finally I would like to thank my family and relatives. They have provided me with all the right ingredients for success and have been waiting endlessly and have encouraged me the most. I would like to dedicate this to my family and hope I can provide them with the kind of support they have provided me.

TABLE OF CONTENTS

CHAPTER Page

LIST OF TABLES

TABLE Page

LIST OF FIGURES

FIGURE Page

FIGURE Page

FIGURE Page

FIGURE Page

FIGURE Page

FIGURE Page

FIGURE Page

FIGURE Page

CHAPTER I

INTRODUCTION TO HIGH TEMPERATURE SMAS

Shape Memory Alloys (SMAs) belong to the class of materials called active materials. These active materials have a capability to undergo a shape change when subject to an external electric, magnetic or thermal field. Some examples of such materials include piezoelectric, magnetostrictive, shape memory alloys and shape memory polymers. In the case of conventional SMAs, the large recoverable strains of 6-10% is due to the reversible nature of the martensitic product phase transformation from the austenitic parent phase. The nature of such a phase transformation in these alloys leads to two unique behaviors namely the shape memory effect and the pseudoelastic effect. These unique characteristics have made SMAs widely popular for a variety of applications in a wide range of industries. However most applications have been limited to operational temperatures of $\simeq 100°C$ due to the low transformation temperatures of conventional Nickel-Titanium alloy systems. However, the demand for actuators in high temperature environments, typically experienced in the aerospace and the oil industries has led to the development of a new class of SMAs called High Temperature Shape Memory Alloys (HTSMAs) with austenitic transformation temperatures that exceed 100°C. HTSMAs are typically created by alloying the binary NiTi system with a third element such as Palladium (Pd), Platinum (Pt), Hafnium (Hf), Zirconium (Zr) or Gold (Au) [1, 2, 3, 4, 5]. Addition of a ternary alloying element can shift the transformation temperatures in these alloys as high as 1000°C [2]. The high transformation temperatures of the alloys make them potential candi-

---

The journal model is *Acta Materialia.*

date materials for actuation in elevated temperature environments. In the following sections we will trace the history of past work done on HTSMAs and highlight the key developments in processing and thermomechanical treatment performed towards improving the performance of these alloys.

A. History of HTSMAs and Past Work

This section traces the history of past work done on HTSMAs leading from the initial discovery to the development of newer alloy systems. Thermomechanical and microstructural studies performed on these alloys following the discovery and experimental observations from the tests are summarized in this section.

1. Discovery of HTSMAs and Preliminary Testing

The first account that motivated the development of HTSMAs was the work by Doonkersloot et al. [6]. They studied the crystallographic structure of the martensitic and the austenitic phases as well as investigated the effect of composition on the martensitic phase transformation temperatures for Au-Ti, Pd-Ti and Pt-Ti binary alloy systems. The studies indicated a shift in the phase transformation temperatures to several hundreds of degrees above room temperature for all the alloys. The small thermal hysteresis associated with the thermally induced phase transformation in these alloys led to the possibility of observable thermoelastic transformation. Following this discovery, in 1979 Khachin and co-workers showed that the Ti-Pd system can be treated as a binary NiTi system with Pd substituting for Ni thereby increasing the transformation temperatures depending on the quantity of Pd replacing Ni [7]. An earlier investigation on NiTi ternary systems was performed by combining a third element such as Copper for which the atomic radii, electrochemical and ionic radii are

similar to those of either Ni or Ti. The solubility of Cu in NiTi without the loss of the shape memory behavior encouraged researchers to explore other elements in the same column of the periodic table (i.e. Au, Pd, Pt, Zr, Hf) to gain the advantage of high transformation temperatures without the loss of shape memory behavior [1]. Their study of the microstructure and thermomechanical behavior of the TiNiAu system did indeed confirm the existence of shape memory behavior in these alloy systems. This initial breakthrough led to the study and development of several new ternary NiTi based HTSMAs. Since NiTiPd ternary HTSMAs will be the focus of the proposed work, the literature review will primarily focus on the developments in this system.

Although some early work was performed on thermomechanical testing of some Pd based high temperature SMAs [8, 9], the first comprehensive work to study the thermomechanical recoverable behavior of these HTSMAs was done by Lindquist and Wayman [2]. In their work, they studied the variation of the transformation temperatures and the associated phase structures (i.e. monoclinic, tetragonal or orthorhombic martensite to cubic) when increasing quantities of ternary elements, Pd and Pt, were added to binary NiTi. Fig. 1 shows the variation of the austenite and martensite transformation finish temperatures with addition of palladium to binary NiTi. Shape memory effect tests were also conducted by loading individual specimens to incremental levels of applied strain in the martensitic state followed by unloading and heating the specimen in the stress free condition to record the recoverable strain generated in these ternary alloy compositions. Similar tests were conducted in 1993 by Otsuka and co-workers on a binary $Ti_{50}Pd_{50}$ composition [10]. The study revealed poor SME behavior with the material generating large irrecoverable strains as the martensitic test temperature increased. The poor SME behavior of the alloy was attributed to low critical stress for slip of the material as the test temperature was increased. Based on the observations, recommendations such as alloying with a ternary element, age hard-

ening and thermomechanical treatment were suggested to improve the SME behavior of the alloy.

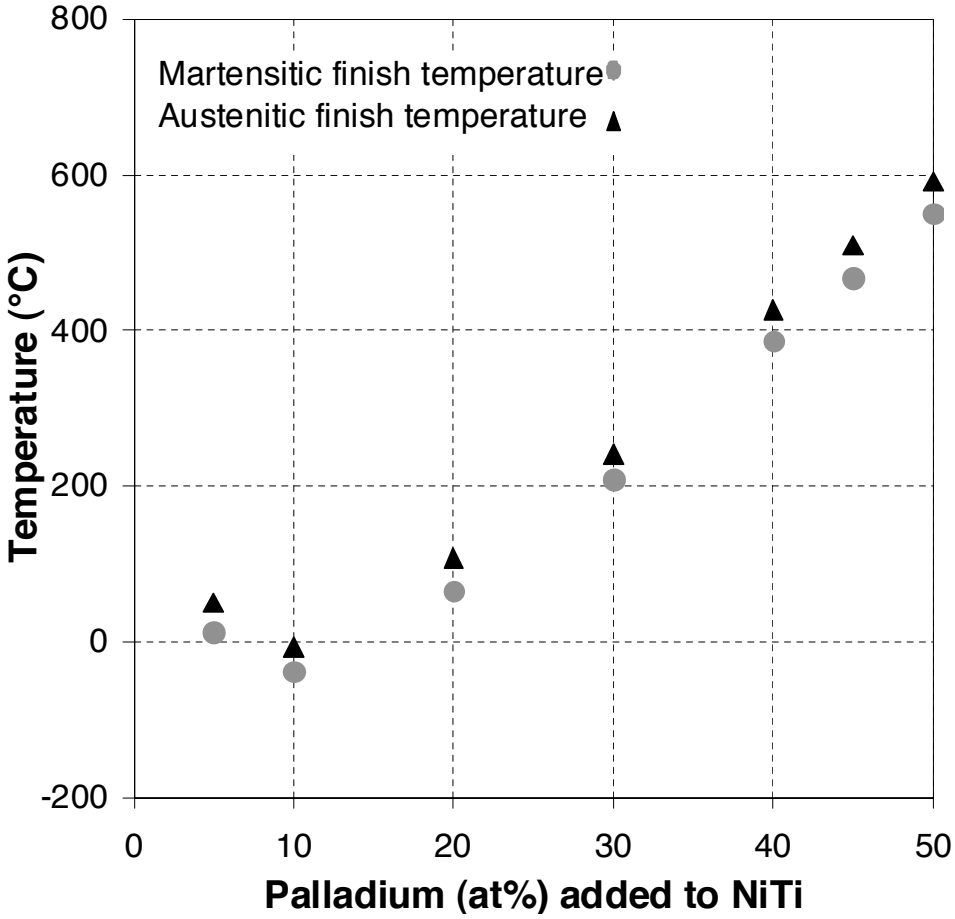

Fig. 1. Effect of Palladium addition on the transformation temperatures when added to binary NiTi (Lindquist.etal.1990 [2]). Palladium replaces Nickel when added to NiTi.

2. Methods Adopted to Improve the HTSMA Behavior

Based on the recommendations made by Otsuka, Golberg and co-workers did a detailed study on $Ti_{50}Pd_{50-X}Ni_X$ compositions where X = 10, 15 and 20, represented the quantity of Nickel substituting for Palladium [11, 12]. The effect of varying Pd compositions and different thermomechanical treatments on the SME behavior was

the primary focus of the work. Ingots were fabricated by plasma melting, hot rolling and subsequently cold rolling with 25-27% reduction in total thickness. Tensile specimens, machined from the rolled bar were either heat treated between $400 - 500°C$ to partially relieve the internal stress due to cold rolling (also know as "Recovery treatment") or were heat treated at 900°C to completely relieve all the effects of rolling (also known as "Solution treatment"). The results indicated higher recoverable strain upon heating to A_f for total applied strain in the specimens that underwent recovery treatment in the martensitic state (below the re-crystallization temperature) as compared to the solution treated or specimens that underwent recovery treatment in the austenitic state. Higher annealing temperatures (as performed in the solution treatment) resulted in partial or complete recrystallization thereby destroying the dislocations/internal stresses induced during the rolling process and reduced the critical stress level for slip to occur.

In addition to the studies to improve the shape memory behavior, some work focussed on the study of pseudoelastic behavior of $Ti_{50}Pd_{30}Ni_{20}$ HTSMAs [13, 14, 15]. Studies of TiPdNi HTSMAs indicated poor or no pseudoelastic response in most compositions. Further, in the compositions that exhibit partial pseudoelasticity, excessive hardening and very small strains due to phase transformation were observed [13]. Other efforts to improve the shape memory behavior included alloying the $Ti_{50}Pd_{30}Ni_{20}$ composition with small quantity of boron to form $Ti_{50}Pd_{30}Ni_{19.8}B_{0.2}$ [16]. Boron was primarily added to form small intermetallic precipitates, 5-200 nm in size, that could strengthen the matrix (by distorting the lattice and thereby causing elastic stress fields that could help pin dislocations) and thereby increase the critical stress for slip. Although the effect of alloying did not show any improvement in the shape memory behavior, a marked increase in the ductility of the TiPdNi alloy was observed. This increase in ductility and ultimate tensile strength was attributed to

the TiB_2 precipitates which form within grains and strengthen the matrix. While most of the preliminary work of HTSMAs focused on studying the shape recovery behavior, the work/actuation characteristics or the ability of the alloy to do work utilizing the SME behavior was not characterized mainly due to the complexity of the experimental setup for high temperature testing.

3. Studying the Work Characteristics of HTSMAs

One of the earliest efforts to study the actuation characteristics of TiPdNi HTSMAs was by Sawaguchi and co-workers. In the study of Ti-rich TiPdNi thin films, Sawaguchi and co-workers noticed that the formation of Ti_2Pd precipitates, of 100μm size, distributed in the grains were responsible for the enhanced shape memory behavior [17]. The thermomechanical testing on the $Ti_{51.2}Pd_{27}Ni_{21.8}$ and $Ti49.5Pd_{28.5}Ni_{22}$ thin films also served as an early study on the actuation characteristics of this alloy. Isobaric thermal cycling tests were conducted on thin strips under various different applied stresses. Transformation strains of 3% were generated under a stress of 400 MPa.

Following this initial work, an extensive study on various TiPdNi HTSMAs for development of actuators was performed by the NASA Glenn research center. The effort aimed at studying and improving the actuation characteristics of these alloys. A range of compositions with palladium varying from 15 to 46 at.% were studied as a part of this effort [18]. All the alloys were typically fabricated by induction melting followed by extrusion at $900 - 1200$°C after encapsulating it in an evacuated steel cylinder. The specimen areas was reduced by a 7:1 ratio. Specimens for both tension and compression testing were fabricated from the processed bar. Composition analysis indicated Ti_2Ni and Ti_2Pd oxides precipitated out of the Ti-rich matrix in addition to some TiC precipitates that were introduced from the graphite crucible

during fabrication. However, the oxide precipitates of Ti_2Ni and Ti_2Pd were of the micron scale, too large to produce coherent stress fields (which is cause by elastic lattice distortion) that would strengthen the alloy. Preliminary uniaxial tests were performed on all the alloy compositions under different isothermal conditions between the martensitic and austenitic transformation temperatures. The results indicated that for palladium compositions greater than 37 at.%, the yield stress of the parent austenitic phase dropped below the yield stress of the martensitic phase [18].

As a result, the work at NASA Glenn concentrated on compositions below 37 at.% palladium. Among these alloys, the actuation behavior of a Ti-rich composition of 30% palladium alloy was the most extensively studied under tensile and compressive loading by performing constant stress thermal cycling tests. From the thermal cycling conducted at each constant stress level, the work output was calculated as the product of the strain generated upon heating and the stress level at which the test was conducted. The study indicated no significant difference in the work output of the alloy in tension and compression for a given stress level. A maximum work output of 10 J/cm^3 corresponded to 2.5% recoverable strain at a stress level of 400 MPa. The work output showed an increase with increasing stress level and began decreasing after reaching a maximum at 400 MPa. In addition, an irrecoverable strain accumulation after thermal cycling at every stress level (due to viscoplasticity, transformation induced plasticity or the presence of retained martensite) was observed. However, the nature of this irrecoverable strain was not investigated.

Plasticity (due to yield) and Transformation Induced Plastic (TRIP) strains in SMAs have been studied extensively [19, 20, 21, 22, 23, 24, 25, 26, 27, 28, 29, 30, 31] and have shown to cause internal stresses in the material which can, in turn affect the materials behavior in subsequent cycles [32, 33]. While plastic phenomena can occur at lower stress levels in HTSMAs than in conventional SMAs due to the lower

stress level for slip, the influence of plasticity in subsequent loading/actuation cycles in HTSMAs has not been studied.

4. Viscoplasticity in SMAs

In addition to phenomena such as the phase transformation and plasticity (due to yield or TRIP) that occur in SMAs, it is also important to consider the influence of vicoplastic phenomenon in HTSMAs. This is particularly important because unlike conventional SMAs, the transformation temperatures of certain HTSMAs can lie within 0.3-0.5 times the melting temperature of the alloy, a range where viscoplastic phenomenon in metals begin to occur.

Studies have been performed investigating the viscoplastic behavior in binary NiTi [34, 35, 36, 37]. Most of these studies have focussed on understanding the creep mechanisms that occur at high temperatures during material fabrication. Standard creep tests on these alloys were performed at temperatures ranging from 470°C to 1100°C under stress levels of 5 to 180 MPa. The resulting steady state creep rates based on the test temperatures, range from 2 x 10^{-9} to 6 x 10^{-3}/sec [37]. Table I and Table II show a list of the different studies performed of the viscoplastic behavior on binary NiTi along with a list of test conditions used in each study. In this table n is the stress exponent and Q is the activation energy during secondary steady state creep. Microstructural studies conducted on the Ni-rich creep specimens have shown an initial decrease in the creep rate associated with the formation of Ni_4Ti_3 coherent precipitates that act as barriers to the motion of dislocations followed by an increase in the creep rate due to the coarsening of the precipitates with the increase in the exposure time at the test temperature [38]. However, the temperatures for phase transformation and the region where creep occurs do not overlap in binary NiTi and as a result, these studies do not provide an understanding of the interaction between the

viscoplastic and transformation behavior. In the present case, as the transformation temperatures in the NiTi alloy increase with the addition of palladium, the phase transformation regime begins to overlap with the temperatures where viscoplastic phenomena occurs. Under such a scenario, constant exposure to the high temperature and/or the rate of actuation could impact the performance of the actuator.

Table I. A comprehensive list of creep tests performed on NiTi alloy along with test parameters (Oppenheimer.etal.2007 [37]).

Investigation	Year	Sample diameter (mm)	Ni content (at.%)	Processing
Mukherjee	1968	6.35	50.6	Hot-swaged rod, annealed at 1000°C
Kato et al.	1999	0.9	49.5,50,50.5	Drawn wires, annealed at 900°C
Eggeler et al.	2002	13	50.7	Rods, solutionized at 850°C
Kobus et al.	2002	-	50.7	Annealed at 500-560°C
Lexcellent et al.	2005	18.5	50.0	Hot drawn bars
Oppenheimer et al.	2007	12.7	50.8	Bars annealed at 950-1100°C

Table II. Continuation of the creep properties listed for work shown in the table above, listed in the same order.

Temp. (°C)	Strain rate (s^{-1})	Stress (MPa)	n	Q (kJ mol^{-1})	Grain size μm
700-1000	$6x10^{-5}$- $6x10^{-3}$	6-178	3±0.2	251±13	-
628-888	$1x10^{-5}$- $2x10^{-2}$	11-81	1	230-253	15
470-530	$2x10^{-9}$- $8x10^{-6}$	90-150	2	334	35
500-560	$2x10^{-7}$- $3x10^{-5}$	120-180	5	421	-
597-897	$3x10^{-3}$- $4x10^{-2}$	10-35	3	222 ± 30	-
950-1100	$1x10^{-6}$- $1x10^{-5}$	4.7-11	2.7±0.2	155±14	48-140

B. Objective for the Current Work

The objectives of the current work are summarized in the sections listed below.

1. The focus of the current work is to study how plasticity, during two commonly used actuation loading paths along which HTSMAs operate, affects the actuation characteristics (i.e. actuation strain, transformation temperatures and irrecoverable strain) and the cyclic actuation behavior. For this purpose the most widely studied palladium based composition, $Ti_{50}Pd_{30}Ni_{20}$, is chosen. Preliminary tests were conducted on compression specimens to determine the composition, transformation temperatures and the monotonic behavior. Following this, the impact of plasticity that occurs during the course of transformation and detwinning along different chosen loading paths was studied. Thermally induced phase transformation tests (with and without pre-strain) were conducted on the HTSMA specimens. The testing was limited to ten consecutive thermal cycles. The irrecoverable and actuation strains from each cycle, for both cases were plot and compared. Additional tests were conducted to try and quantify the effect of plasticity (during the detwinning process) as a function of the maximum applied stress.

2. In palladium based HTSMAs with transformation temperatures between 300-500°C, viscoplastic behavior can occur simultaneously with transformation during an actuation cycle. However, the simultaneous interaction of these two mechanisms and the impact of viscoplasticity on the actuation behavior of HTSMAs has not been studied. To study the impact on viscoplasticity on transformation, a $Ti_{50}Pd_{40}Ni_{10}$ HTSMA was selected for investigation, fabricated, and thermally induced transformation cycles at different stress levels/heating-cooling rates were conducted on compression specimens. The simultaneous evolution of rate dependent viscoplastic strains with the rate independent transformation behavior is recorded and the actuation and irrecoverable strains gener-

ated at the end of the test cases are compared. Following the tests, the specimen microstructure is analyzed using an electron microscope to study the underlying microstructural changes.

3. The actuation behavior of the $Ti_{50}Pd_{40}Ni_{10}$ HTSMA was also studied under tensile loading. Preliminary tests were conducted studying the tensile actuation behavior of $Ti_{50}Pd_{40}Ni_{10}$ HTSMA. During the first thermally induced phase transformation cycle under a constant stress, a unique two stage expansion was observed during heating and cooling. Upon unloading, a two stage contraction was observed recovering the strain generated at the higher stress level. To investigate this transformation in further detail and study the tensile actuation characteristics, isobaric thermal cycling tests were conducted at different stress levels. The phase transformation was also studied using X-Ray Diffraction (XRD) at different stages during the transformation to understand the associated microstructural changes. The cyclic actuation behavior was also investigated for a limited test cycle.

   A flowchart showing the different aspects of the current work is shown in Fig. 2.

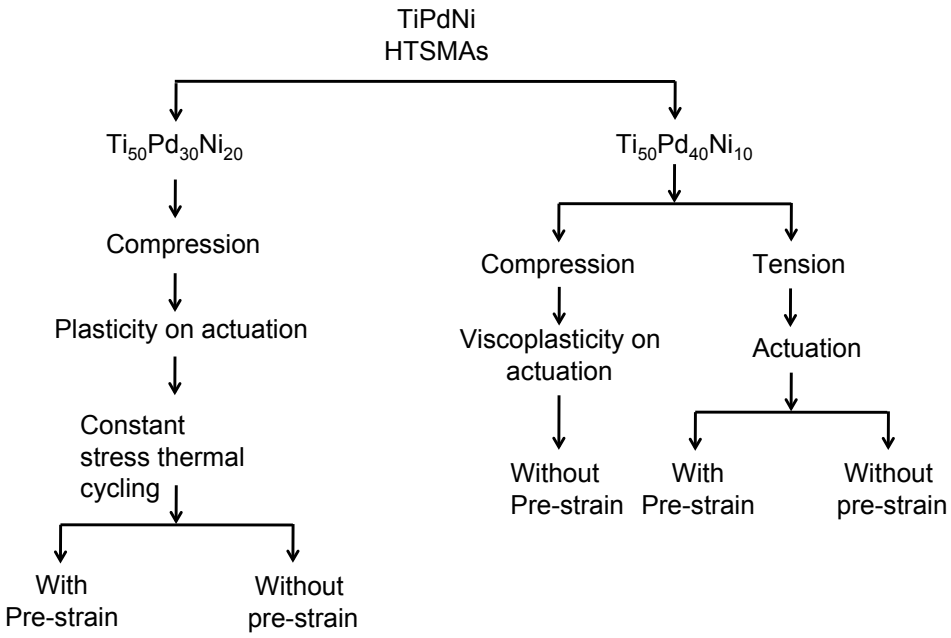

Fig. 2. Flowchart representing the objective of the present effort.

CHAPTER II

EFFECT OF IRRECOVERABLE STRAINS ON THE PHASE TRANSFORMATION BEHAVIOR IN $TI_{50}PD_{30}NI_{20}$ HIGH TEMPERATURE SHAPE MEMORY ALLOY

For actuation applications using SMAs, the shape memory effect is predominantly utilized. The most common methodology involves designing an actuator around the generated actuation strain under a desired design stress level. For such design requirements, thermal cycling under a constant applied stress is the most commonly adopted loading path to characterize the actuation behavior of an SMA. Such a loading path is also called a constant stress thermal cycling path.

Constant stress thermal cycling tests have been conducted in the past on $Ti_{50}Pd_{30}Ni_{20}$ HTSMAs under tension and compression and their cyclic actuation behavior has been studied [39, 40]. However, in certain cases, design inflexibilities can force the requirement for a minimum actuation strain under a given operational stress level. One such example is when the design requires the SMA to initiate actuation from a stress free state and then make contact and move a part. In such a scenario a constant stress thermal cycling load path may not be completely effective.

Furthermore, for a design where an SMA replaces an existing component, a modified SMA operating mechanism may be a cheaper alternative when compared to a redesign of the entire part. In such constrained design scenarios a constant strain SME loading path can be chosen, where the specimen is detwinned to a specific constant applied strain, unloaded to the desired stress and subsequently actuated. Although such design constraints are not commonly encountered in mainstream applications, in demanding environments such as seen by the aerospace and the oil industry, the

harsh operating conditions can eliminate other options-leaving such loading paths as the only viable design alternative.

This chapter investigates two different SME loading paths and summarizes the effects of inelastic phenomena that occur during loading along these paths on the performance of the actuator. For this purpose an ingot of $Ti_{50}Pd_{30}Ni_{20}$ alloy is vacuum arc melt, cast and hot rolled and then compression test specimens are machined from the bar. The actuation behavior of the SMA is investigated under constant applied strain and constant applied stress loading paths. The influence of the different loading paths with cycles is studied by measuring the shift in the transformation temperatures, actuation and the irrecoverable strain generated. Suitable conclusions are drawn based on the observations.

A. Materials and Methods

1. Fabrication and Calorimetry

An ingot (0.75 inch x 0.75 inch x 5 inch in dimension) with a nominal composition of $Ti_{50}Pd_{30}Ni_{20}$ was fabricated by vacuum arc melting individual quantities of Titanium, Palladium and Nickel in a water-cooled copper hearth. The composition of the cast bar was determined (using vapor absorption spectroscopy) to be 49.9/30.2/19.9 at.% of Ti/Pd/Ni respectively. Uniformity of the composition was ensured by measuring samples from different regions of the cast bar which showed 0.05-0.1 at.% variation. The ingot was then homogenized in vacuum at 1000°C for five hours and the homogenized bar was hot rolled at 900°C through multiple steps with 30% total reduction in thickness (5% reduction in each step). A picture of the as-cast and hot rolled bars is shown in Fig. 3a.

From the hot rolled bar, cylindrical compression specimens (12 mm in length

and 6 mm in diameter) were cut by Electrical Discharge Machining (EDM) along the rolling direction (Fig. 3b). Thin sections were cut from the rolled bar were cut for measuring the transformation temperatures using a Differential Scanning Calorimeter (DSC). The sample pan and the empty reference pan are heated simultaneously to maintain the same temperature in both pans and the difference in the heat supplied to maintain the same temperature is measure. Fig. 4 shows a picture of the DSC chamber indicating the sample and the reference pan in the heating/cooling chamber. The pan containing the SMA will absorb more heat to maintain the same temperature as the reference pan during the course of a reverse phase transformation (due to the latent heat of transformation), and this difference shows up as a peak on the heat flow axis. The transformation temperatures of the hot rolled bar measured by DSC are shown in Fig. 5. The transformation temperatures M_f, M_s, A_s and A_f of the rolled bar are 222°C, 247°C, 254°C and 273°C respectively. These temperatures were determined by the tangent intersection method.

2. Thermomechanical Testing

Thermomechanical tests were conducted on a custom high temperature test setup. Compression grips machined from Inconel were chosen to avoid softening at high test temperatures. The heating was performed using a water cooled quad lamp furnace. The temperature of the specimen was held constant using a thermocouple mounted on the specimen's surface to record the sample temperature and then send it to a feedback controller, which in turn controlled the intensity of the furnace lamps to maintain a user set temperature. The strain was measured using an high temperature water cooled extensometer whose ceramic leads were mounted on the Inconel grips. The strain due to the SMA was calculated by subtracting the strain due to the thermal expansion of the grips from the total strain measured by the extensometer

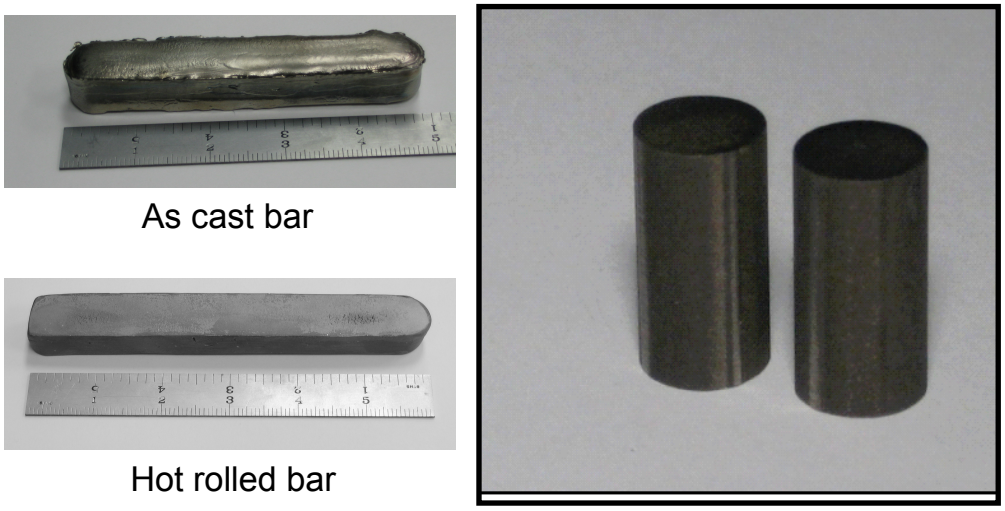

(a) (b)

Fig. 3. **(a)** Picture of the as-cast and the hot rolled $Ti_{50}Pd_{30}Ni_{20}$ HTSMA bar. **(b)** Compression specimen 6 mm diameter x 12 mm length machined along the rolling direction from the hot rolled bar.

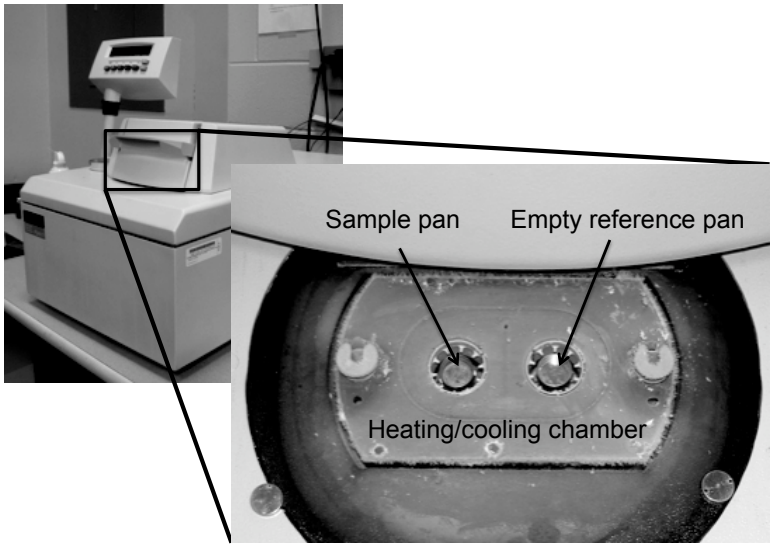

Fig. 4. Picture showing the DSC and a close up of the sample and the empty reference chamber.

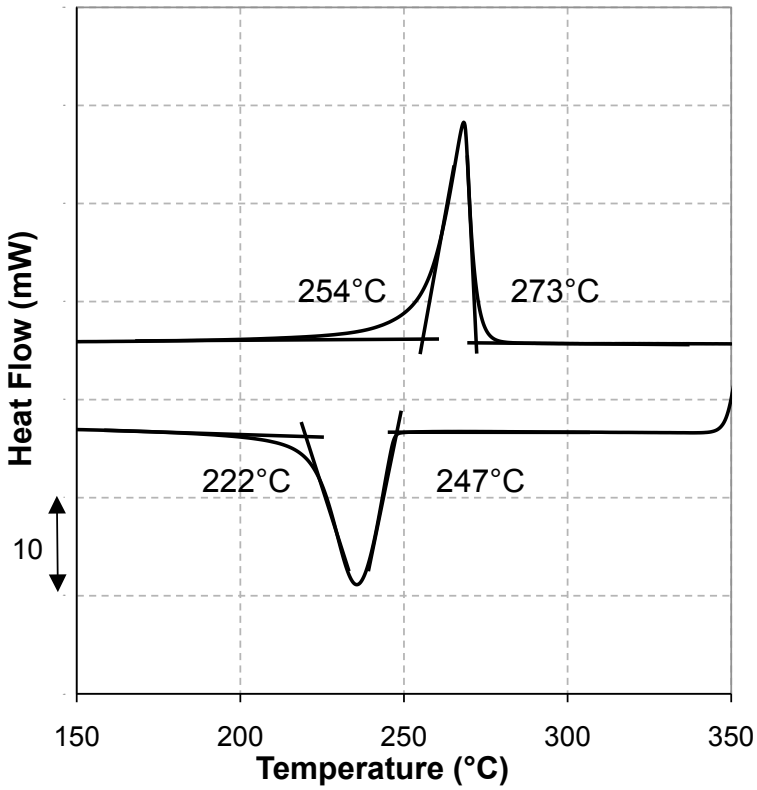

Fig. 5. DSC results for the rolled material indicating martensite and austenite start and finish transformation temperatures.

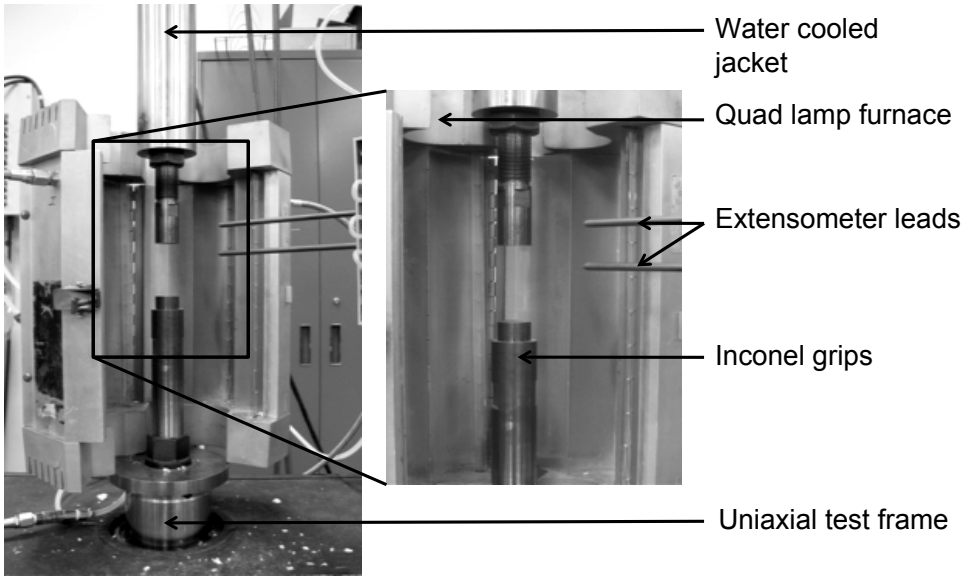

Fig. 6. Thermomechanical setup for compression testing of HTSMAs.

(details pertaining to the calculation of strain are shown in Appendix A). The load cell measuring the force was isolated from the furnace by a water cooled jacket. The complete setup was assembled on a MTS uniaxial frame and the force, strain and temperature were recorded through the MTS software. The assembled test setup with a zoomed image of the grips and extensometer leads is shown in Fig. 6.

a. Uniaxial Testing

Preliminary uniaxial compression loading was performed on the compression specimens at 40°C above and below the A_f and M_f temperatures (as determined by the DSC), to determine the uniaxial response of the martensite and austenite phases (tests 1 and 2 in Table III). For the uniaxial test, the specimen was held at a stress of 10 MPa and gradually heated to the test temperature. Holding the temperature constant, the specimen was loaded at a rate of 10^{-4}/sec (quasi-statically) until yielding

was observed.

For use in actuators, SMAs typically need to be trained. Training is the process of repeating a thermomechanical loading path to stabilize the generation of irrecoverable strain. In the use of SMAs for actuator applications, the two methods of training, include constant stress training (i.e. thermal cycling under a constant stress level) and pre-strain training (i.e. thermal cycling under a constant stress level after initial prestrain). The testing procedures and the operating conditions for the two loading paths are described in detail below.

b. Constant Load Thermal Cycling

The material behavior is first studied along the constant load thermal cycling loading path. Since no change in the specimen cross section is observed over the duration of the test the constant load test can be called a constant stress test when normalized by the initial specimen cross section. Test stresses of 100, 200 and 500 MPa were used for testing. The stress levels of 100 and 200 MPa were chosen because most SMA actuators typically operate under these stress levels. To observe the SMA performance at a stress level much higher than those typically studied, an additional stress level of 500 MPa was chosen. These tests, 3,4 and 5 are shown in the test matrix (Table III). A schematic of the loading path is shown in Fig. 7. The temperature for loading was chosen such that under the applied stress the specimen was completely in the austenitic state (point A). For each test case, a preliminary thermal cycle was performed on the SMA holding a constant compressive stress of 10 MPa and the transformation temperatures and transformation strain was measured (not shown in the schematic). A heating cooling rate of 5°C/min was chosen because the heating cooling rate did not significantly alter the transformation temperatures suggesting a relatively uniform specimen temperature through the cross section (see Appendix A).

The specimen was subsequently loaded to the test stress level B, isothermally to the austenitic state. The stress was held constant and specimen was cooled to martensite (point C) and subsequently heated to austenite again (point D). Ten thermal cycles were conducted on the specimen (not shown in the schematic). The number of cycles were limited to ten since the actuation strain and the irrecoverable strain stabilized and remained constant within 10 cycles. Additionally at 5°C/min each heating/cooling cycle took approximately 1.5 hours. Restricting the test to ten cycles limited to testing time per specimen. After the thermal cycling, the specimen was unloaded to 10 MPa (point E) and a thermal cycle was performed (E-F-E) to record any changes in the reference transformation temperatures or transformation strain. The first cycle from the strain-temperature result at each stress level was used to generate a preliminary stress-temperature phase diagram.

Table III. Test matrix for the preliminary uniaxial tests and constant stress thermal cycling tests on the $Ti_{50}Pd_{30}Ni_{20}$ compression specimens.

Test #	Test type	Applied stress/strain	Temperature	Loading rate
1	Uniaxial loading	-	180°C	10^{-4}/sec
2	Uniaxial loading	-	330°C	10^{-4}/sec
3	Thermal cycling	10 MPa	180-380°C	5°C/min
	Thermal cycling	100 MPa	180-380°C	5°C/min
	Thermal cycling	10 MPa	180-380°C	5°C/min
4	Thermal cycling	10 MPa	180-380°C	5°C/min
	Thermal cycling	200 MPa	180-380°C	5°C/min
	Thermal cycling	10 MPa	180-380°C	5°C/min
5	Thermal cycling	10 MPa	180-380°C	5°C/min
	Thermal cycling	500 MPa	180-380°C	5°C/min
	Thermal cycling	10 MPa	180-380°C	5°C/min

c. Constant Load Thermal Cycling after Initial Pre-strain

To understand the effects of pre-straining on the constant load thermal cycling, the experimental study was performed in two stages. Similar to the previous case no

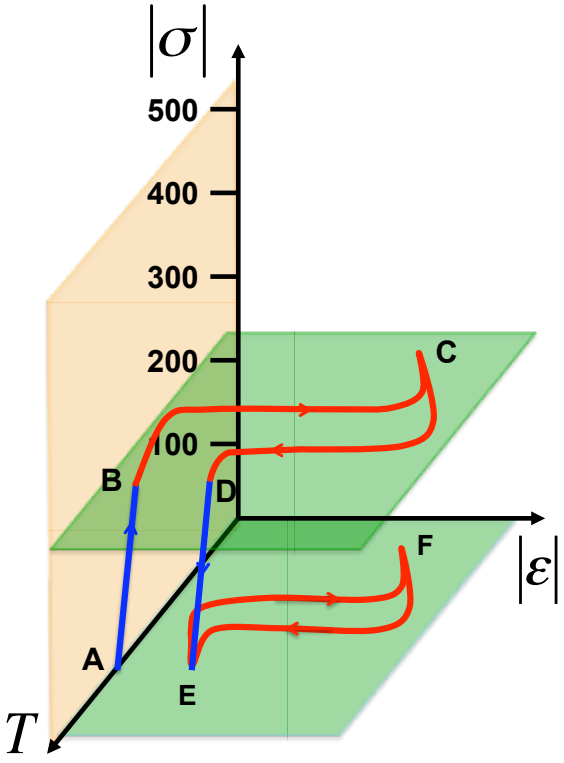

Fig. 7. A schematic of the constant stress thermal cycling loading path.

Table IV. Test matrix for $Ti_{50}Pd_{30}Ni_{20}$ compression test specimens. Constant applied strain followed by constant stress thermal cycling tests.

Test #	Test type	Applied stress/strain	Temperature	Loading rate
6	Thermal cycling	10 MPa	180-380°C	5°C/min
	Uniaxial loading	2%	180°C	10^{-4}/sec
	Thermal cycling	10 MPa	180-380°C	5°C/min
	Uniaxial loading	4%	180°C	10^{-4}/sec
	Thermal cycling	10 MPa	180-380°C	5°C/min
	Uniaxial loading	6%	180°C	10^{-4}/sec
	Thermal cycling	10 MPa	180-380°C	5°C/min
7	Uniaxial loading	4%	180°C	10^{-4}/sec
	Thermal cycling	100 MPa	180-380°C	5°C/min
	Thermal cycling	10 MPa	180-380°C	5°C/min
	Uniaxial loading	4%	180°C	10^{-4}/sec
	Thermal cycling	150 MPa	180-380°C	5°C/min
	Thermal cycling	10 MPa	180-380°C	5°C/min
	Uniaxial loading	4%	180°C	10^{-4}/sec
	Thermal cycling	200 MPa	180-380°C	5°C/min
	Thermal cycling	10 MPa	180-380°C	5°C/min

change in the specimen cross section is considered and the test the constant load test are interpret at constant stress test after being normalized by the initial specimen cross section. The first stage was to understand the effect of pre-strain on the no load phase transformation behavior. For this purpose, tests were conducted by applying different pre-strain levels to a specimen (in the martensitic state) and studying the subsequent transformation upon heating under a constant stress of 10 MPa. The loading path for this first stage of testing is given in the test matrix (Table IV, test 6). A schematic of the loading path is shown in Fig. 8. The specimen was initially held under a compressive stress of 10 MPa in the martensitic state (point A) and one thermal cycle was conducted to determine the as-received phase transformation temperatures and strain in the alloy, as a reference state of the material (not shown in the schematic). Following this a 2% strain (point B) was applied to the specimen at a constant temperature of 180°C (in the martensitic state) and was subsequently

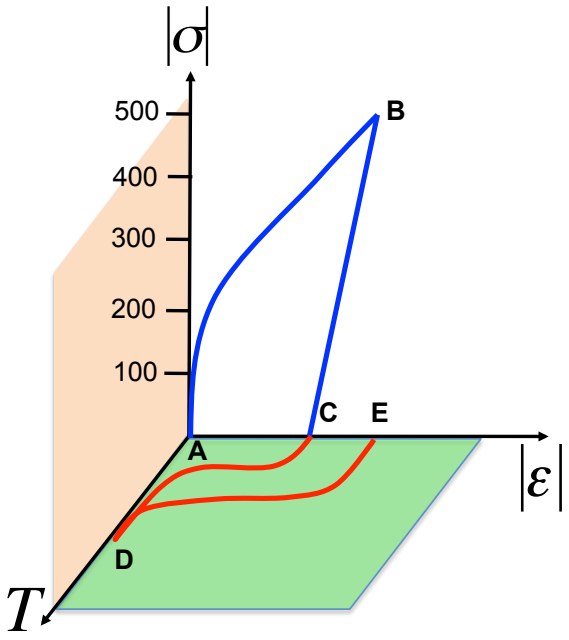

Fig. 8. A schematic detwinning or pre-straining loading path.

unloaded back to 10 MPa (point C). After unloading a second thermal cycle was conducted (C-D-E) at a constant stress of 10 MPa and any shift in the transformation temperatures and/or the recoverable strain was recorded. The loading path was repeated for applied strain levels of 4% and 6% followed by subsequent unloading and a thermal cycle at a constant stress of 10 MPa. From the test results, the shift in the transformation temperatures at 10 MPa was recorded and plotted against the applied strain and maximum stress level achieved (in each applied strain level case). The effects of applied strain were studied by comparing the shift in the transformation temperatures to the preliminary phase diagram established from the first constant stress thermal cycling tests.

The study was then extended to study how the pre-strain affected the actuation behavior at different stress levels. Three pre-strain levels, 4%, 4/5% and 5% were

chosen because the specimen showed maximum actuation strain with 4-5% prestrain). The schematic of the stress strain temperature diagram for this loading path is shown in Fig. 9. In this study, the specimens were pre-strained (from A to B in Fig. 9) and unloaded to actuation stress levels (B to C) of 100, 150 and 200 MPa and thermally actuated under constant stress conditions (C-D-E). The specimen was then unloaded to the point F and one thermal cycle was conducted to recover any residual martensite (F-G-F). A loading path for such a test is given in the test matrix (Table IV, test 7). In test 7 the specimen, initially under a 10 MPa compressive stress, was pre-strained to 4% in the martensitic state at a constant temperature of 180°C. The specimen was then elastically unloaded to a stress of 100 MPa and thermally cycled through the transformation region to determine the actuation strain (i.e. strain generated during heating). The specimen was then cooled back to 180°C and unloaded to 10 MPa. Holding the stress constant, a thermal cycle was conducted through the transformation temperatures to recover any residual detwinned martensite. Following this, the specimen was pre-strained again to 4% and the loading path was repeated for actuation stress levels of 150 and 200 MPa. The above described loading path was also conducted for pre-strain levels of 4.5% and 5%. The actuation strain at different constant stress levels for each pre-strain case is recorded.

Based on the results from the actuation behavior for different applied strains at different actuation stress levels, a specific applied strain and actuation stress level combination is taken to study the cyclic actuation behavior. The stress-strain behavior over the 10 cycles is recorded and the actuation and irrecoverable strain in each cycle is plotted over the 10 consecutive cycles.

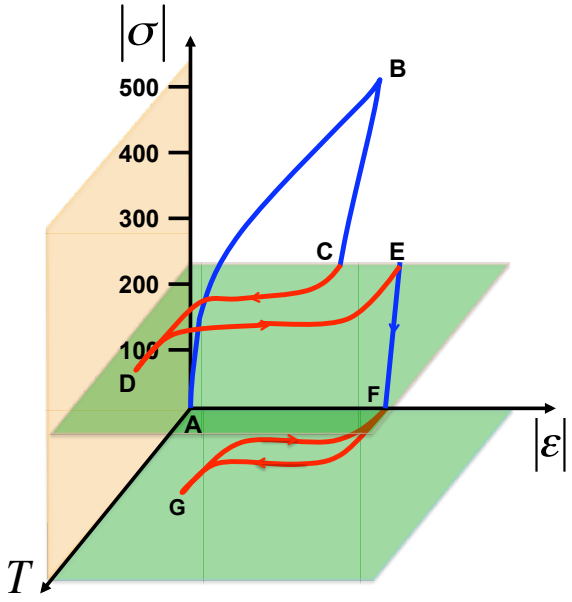

Fig. 9. A schematic of the constant stress thermal cycling loading path after pre-strain.

B. Results and Discussion

1. Uniaxial Testing

The uniaxial stress-strain results for the $Ti_{50}Pd_{30}Ni_{20}$ compression specimens in the martensitic and austenitic states are shown in Fig. 10. The uniaxial result for the loading in martensite (performed at 180°C) indicates the start of the detwinning process at approximately 200 MPa. Upon continued loading no clear end point of detwinning is observed and the stress continues to increase until the specimen yields at approximately 1100 MPa. From the uniaxial behavior of austenite conducted at 330°C, stress induced martensitic transformation initiates at approximately 390 MPa and yielding is observed at approximately 700 MPa.

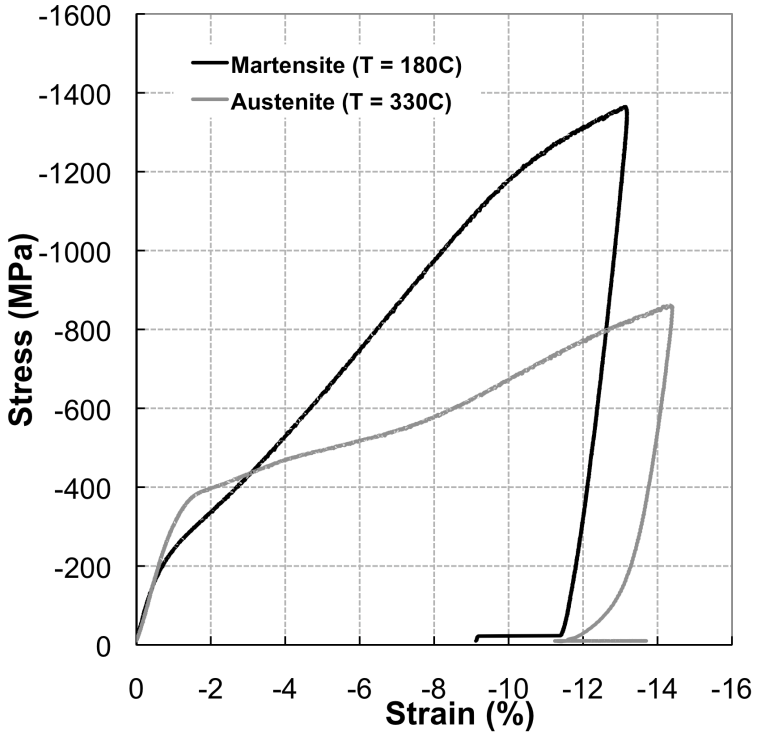

Fig. 10. Uniaxial test result in the martesite and austenite phase.

2. Constant Load Thermal Cycling

The results from the constant stress thermal cycling conducted at 100, 200 and 500 MPa, along with the intermediate thermal cycles conducted at 10 MPa at a heating/cooling rate of 5°C/min, are shown in Fig. 11, Fig. 12 and Fig. 13, respectively. From the training under different applied stress levels, the actuation strain and the irrecoverable strain in each cycle is calculated and shown in Fig. 14a and Fig. 14b, respectively. The irrecoverable strain is calculated as the strain between the start of two consecutive thermal cycles and the actuation strain is calculated as the difference in the strain values at the start and the end of the heating cycle.

The results from the thermal cycling at 100 MPa shows that the irrecoverable strain generated in each cycle gradually decreases until a complete stabilized behavior

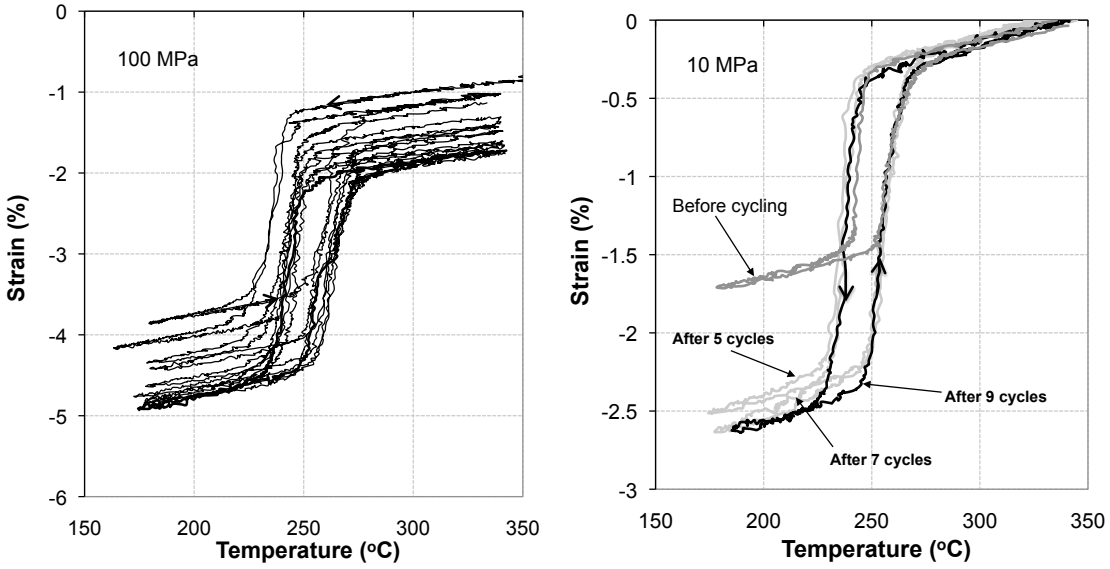

(a) (b)

Fig. 11. Strain-temperature behavior **(a)** at 100 MPa showing stabilization of irrecoverable strain after 9 cycles; **(b)** at 10 MPa showing the evolution of the TWSME at intermediate stages during the thermal cycling at 100 MPa.

is observed after 9 thermal cycles (Fig. 14b). The cycles for training is significantly less than what is observed in conventional NiTi SMAs which typically take 100-200 cycles. From the strain temperature behavior, it is noticed that the actuation strain at 100 MPa (Fig. 14a) increases from 2.9% to 3.1% over the 9 thermal cycles and the irrecoverable strain, starting at 0.15%, gradually decreases over the course of cycling. This decrease in the irrecoverable strain is associated with the stabilization of the dislocations caused by transformation induced plasticity (TRIP) that orient certain preferred martensitic variants along a specific path thus allowing for stabilized actuation behavior. The effect of the generated TRIP strain and the associated stabilization of select martensitic variants can also be seen in the TWSME which increases from $\simeq$ 1.0% before training to $\simeq$ 2.0% after training at 100 MPa.

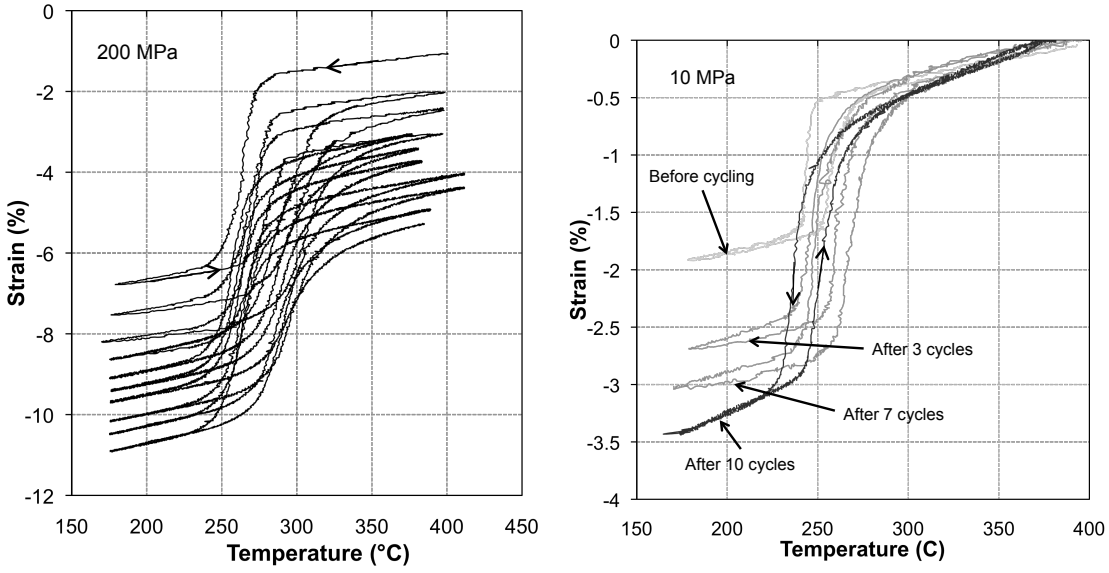

(a) (b)

Fig. 12. Strain-temperature behavior **(a)** at 200 MPa showing stabilization of irrecoverable strain after 9 cycles; **(b)** at 10 MPa showing the evolution of the TWSME at intermediate stages during the thermal cycling at 200 MPa.

If we look at the actuation strain evolution for the 200 MPa thermal cycling case, it is noticed that the actuation strain increases from an initial 4.8% to 5.6% towards the 9th cycle (Fig. 14a). The irrecoverable strain appears to remain constant (at a non zero value) with each consecutive cycle. The increase in the actuation strain can be attributed to the elastic stress field due to the generated dislocations that reorient additional martensitic variants favorably under the bias stress. Similar to the 100 MPa case, the generation of TRIP strain results in permanently reorienting certain martensitic variants which causes an increase in the TWSME behavior from $\simeq 1.0\%$ to $\simeq 2.3\%$. Stabilization of the actuation was not observed after the 9 cycles indicating the requirement of additional cycles for repeatable actuation behavior.

For the 500 MPa case, no stable actuation is observed after the thermal cycles

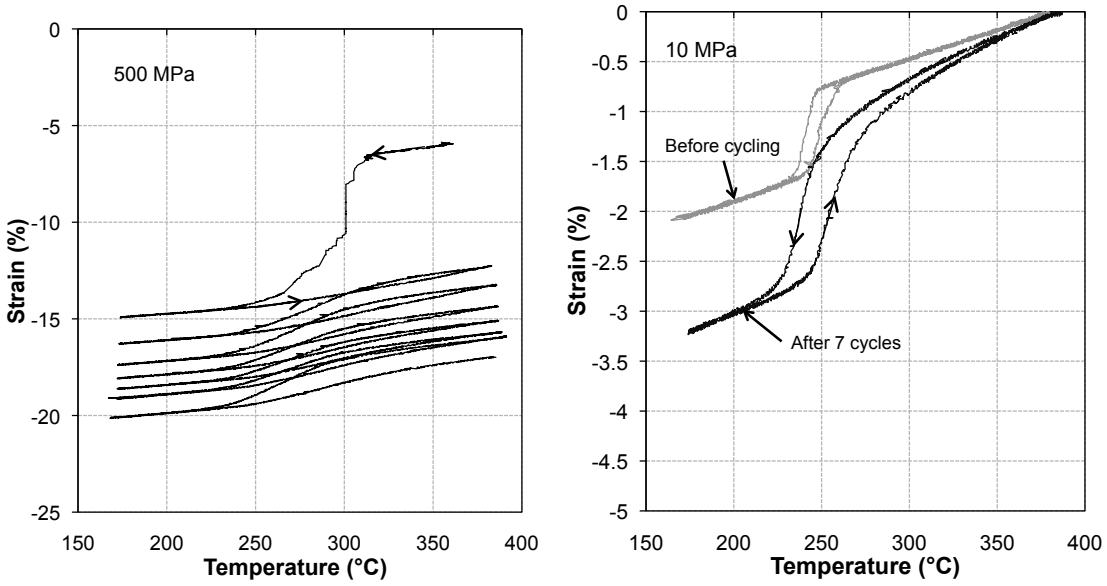

(a) (b)

Fig. 13. Strain-temperature behavior **(a)** at 500 MPa showing stabilization of irrecoverable strain after 9 cycles; **(b)** at 10 MPa showing the TWSME at start and the end of the thermal cycling at 500 MPa.

and after a large irrecoverable strain generated in the first cycle, the irrecoverable strain appears to remain constant with each consecutive cycle. The actuation strain (Fig. 14a) is only 3.1% for the 500 MPa. The corresponding TWSME after the thermal cycling at 500 MPa is 1.9%. The low actuation strain and the decrease in the TWSME compared to the 200 MPa case (even after training at a higher stress level) may be associated with the formation of retained martensite along with TRIP resulting in a lower actuation strain and TWSME. The retained martensite formed in the material does not contribute to subsequent transformation resulting in a decrease in the transformation strain observed.

A preliminary phase diagram was generated from the 1st thermal cycles at stress levels of 10, 100 and 200 MPa as shown in Fig. 15. The slopes in the phase diagram

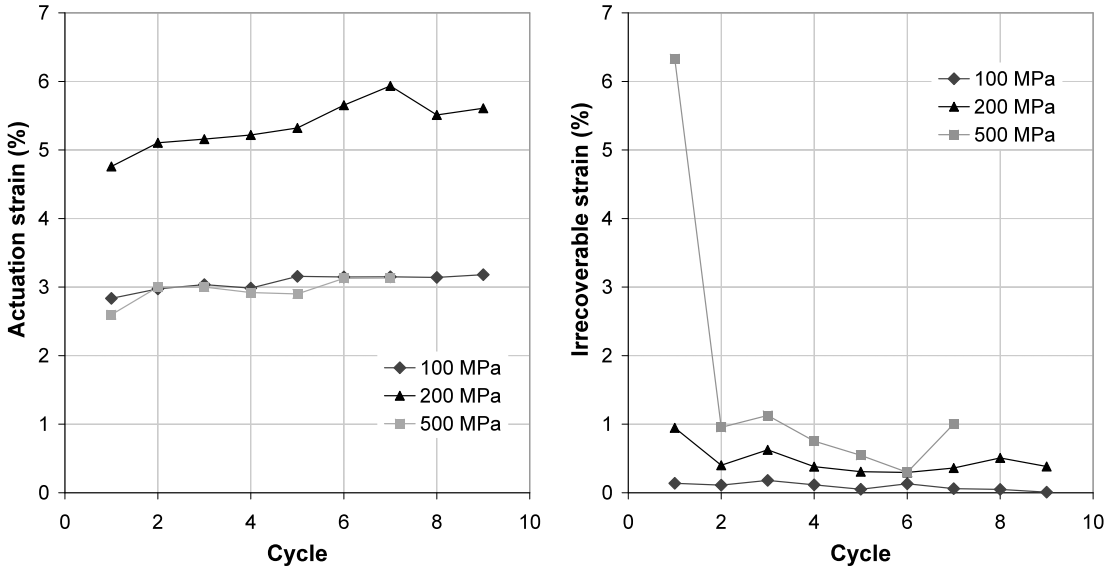

(a) (b)

Fig. 14. Strains measure in each cycle for thermal cycling at each constant stress level **(a)** Actuation strain in each cycle; **(b)** irrecoverable strain in each cycle.

represents the Clausius-Clayperon relationship for the as-processed SMA without influence from thermomechanical testing.

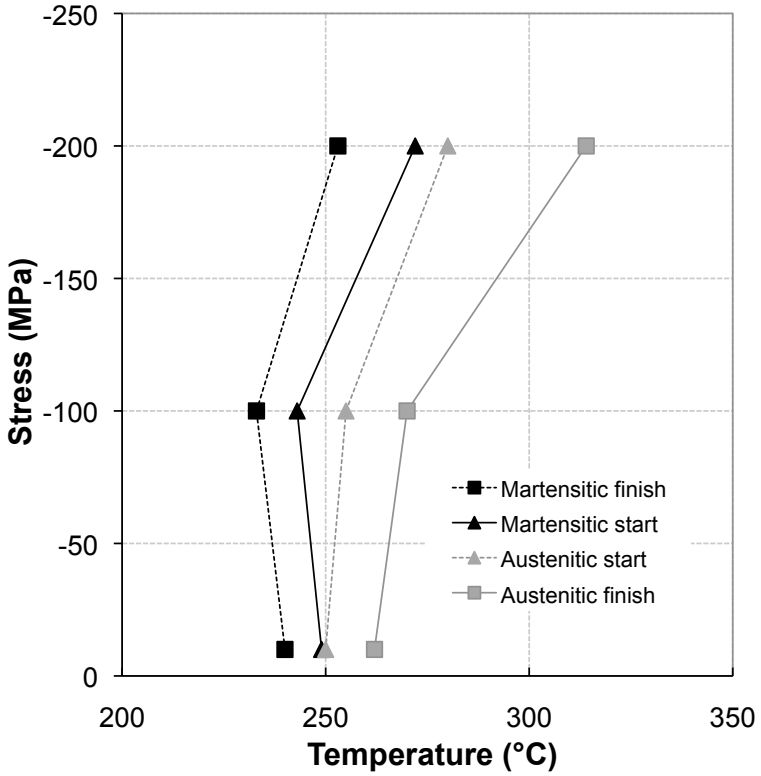

Fig. 15. As-received stress-temperature phase diagram for $Ti_{50}Pd_{30}Ni_{20}$ HTSMA generated from 1st thermal cycle under each stress level.

3. Constant Load Thermal Cycling after Initial Pre-strain

From the pre-strain test results, the strain-temperature and the stress-strain behavior from test 6 will be presented in detail. Following this the results from test 7 will be presented. In test 6, a preliminary thermal cycle was conducted at a stress of 10 MPa, following which the specimen was loaded to a 2% applied strain. The associated strain-temperature and stress-strain behaviors are shown in Fig. 16a and Fig. 16b, repsectively. From Fig. 16a, it is noticed that the HTSMA exhibits a fully recoverable

0.5% transformation strain. Following this the HTSMA was detwinned to 2% strain and a second thermal cycle was conducted at 10 MPa again. The strain-temperature behavior for this second thermal cycle is shown in Fig. 16c and the transformation temperatures from the strain-temperature response are measured by the tangent intersection method. The specimen was then loaded to 4% and 6% applied strain levels (Fig. 17a). After detwinning to each strain level, the specimen was subsequently unloaded and heated at 10 MPa stress and the shift in the transformation temperature after each loading was calculated and plotted against the maximum stress achieved during each applied strain cycle (Fig. 17b).

Comparing the shifted austenite start and finish temperatures from Fig. 17b, with the preliminary phase diagram established in Fig. 15, the internal stress caused after each applied strain case due to the detwinning can be calculated. The presence of the same martensitic finish temperature and the shift of the austenitic temperatures suggests the presence of an stress gradient causing the reverse transformation to initiate at the stress free state or at an internal stress below 100 MPa (since up to 100 MPa, M_s and M_f remain constant) and finish in the stress induced martensitic state.

Since the material already exhibits transformation behavior at 10 MPa, in the case of no plastic strain accumulation during the detwinning, the recoverable strain after unloading must be a sum of the TWSME and the inelastic part of the applied strain after unloading. A schematic representing the strains from the test and the calculation method is shown in Fig. 18. By comparing the recovered strain upon heating with the inelastic strain remaining after unloading plus TWSME, the plastic strain (the difference between the two) is calculated. The calculated plastic strain after each cycle is cumulatively plotted against the measured cumulative internal stress at the end of each detwinning cycle (Fig. 19). From Fig. 19, it is noticed

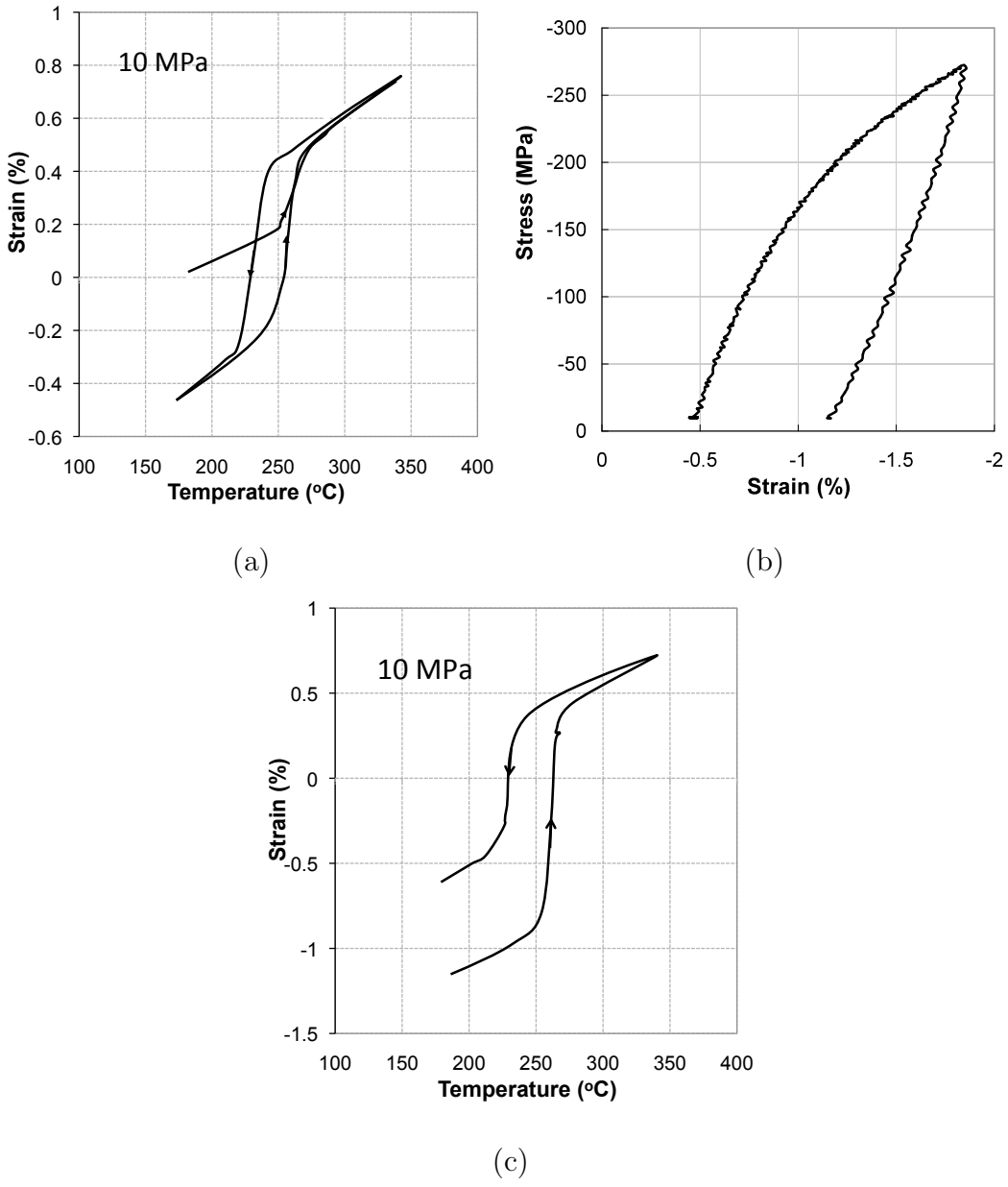

(a) (b)

(c)

Fig. 16. Plots showing **(a)** the strain-temperature transformation observed in the as-processed specimen; **(b)** the detwinning to 2% strain following one thermal cycle at 10 MPa; **(c)** the strain-temperature transformation at 10 MPa after the detwinning to 2% strain.

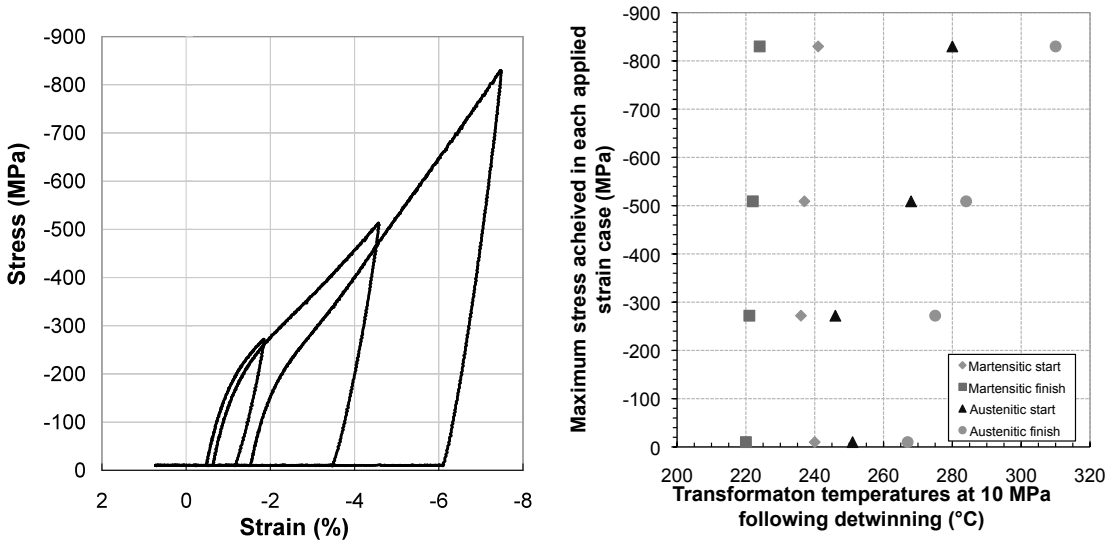

(a) (b)

Fig. 17. **(a)** Stress-strain diagram showing the detwinning to 2%, 4% and 6% strain followed by a subsequent unloading and a thermal cycle at at 10 MPa; **(b)** A stress-temperature diagram showing the maximum stress obtained during each detwinning case (i.e. 2% strain, 4% strain etc.) plot against the transformation temperatures measured from the thermal cycle at 10 MPa after each detwinning case.

that the internal stress in the material exhibits an increase with the accumulation of plastic strain. The simultaneous development of plasticity during the detwinning of the material (even below the yield stress) leads to internal stress which is accounted for by measuring the shift in transformation temperatures.

To quantify the internal stress generated in the material and implement it in a model, the calculated internal stress during each detwinning cycle is plotted as a function of the maximum applied stress in each case (although the control parameter in each case was the applied strain). The maximum applied stress, obtained from the stress-strain data (Fig. 17a) is plotted against the internal stress as shown in Fig. 20. It must be noted that the internal stress and the maximum stress are cumulative data by nature since the history due to a previous cycle is already included in the measured data. From Fig. 20, it is noted that the internal stress continues to increase with the increase in maximum applied stress.

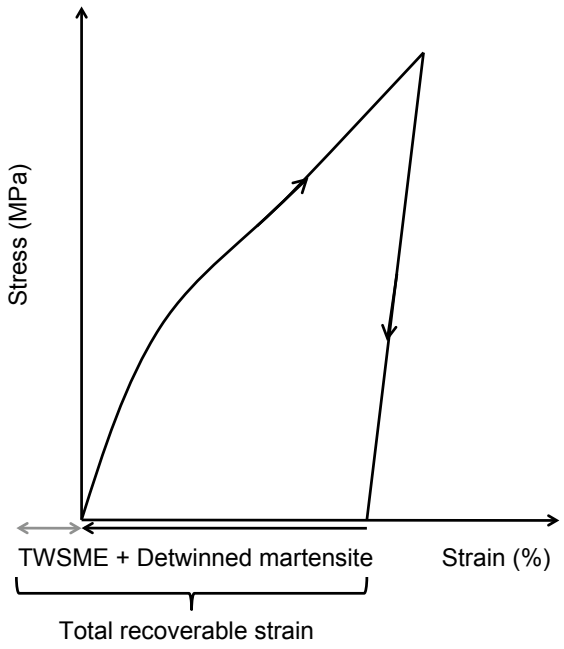

Fig. 18. Schematic of the stress-strain behavior showing the different strains associated with the material in a loading cycle.

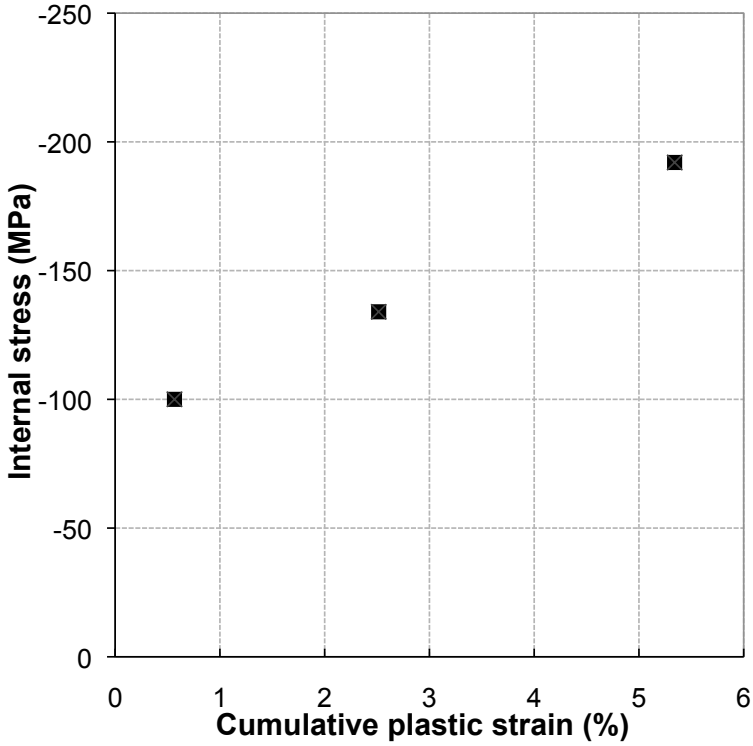

Fig. 19. A stress-strain plot indicating the internal stress generated for each detwinning cycle (specimen 6) plot against the plastic strain generated at the end of each detwinning cycle.

To verify the impact of the internal stress accumulated due to detwinning on the actuation behavior along an applied strain loading path, a specimen was detwinned by applying 4% strain and was then unloaded to a 100 MPa stress level. Holding a constant stress of 100 MPa, one thermal cycle was conducted and the transformation temperatures were noted. The stress-strain diagram corresponding to the loading and the thermal cycle at 100 MPa are shown in figures Fig. 21a and Fig. 21b, respectively. The austenitic finish transformation temperature from Fig. 21b was measured and compared with the preliminary phase diagram, Fig. 21c. From Fig. 21c, it is observed that the measured A_f transformation temperature corresponds to an internal stress of approximately 200 MPa. This is consistent with the expected behavior

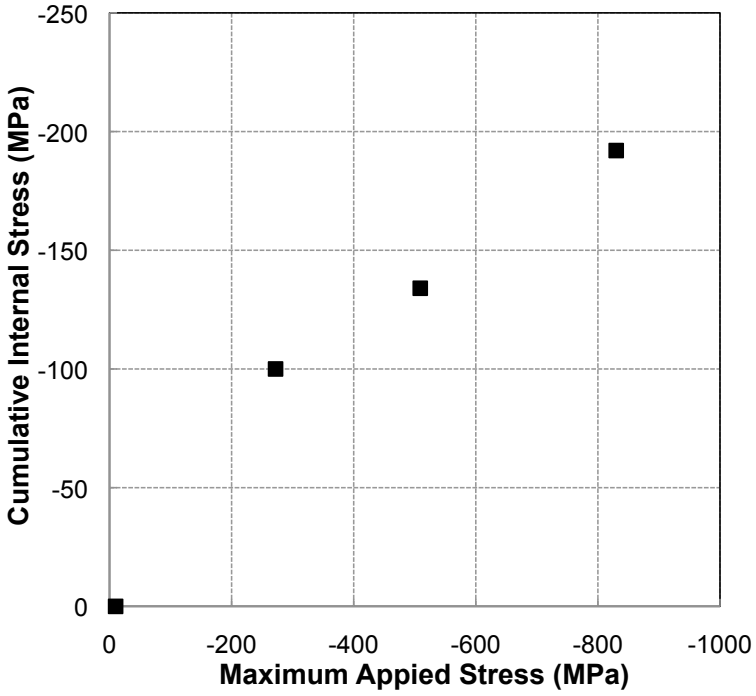

Fig. 20. A stress-stress diagram showing the internal stress generated after each detwinning cycle versus the maximum stress applied, in each detwinning cycle.

since from Fig. 19, it is already known that applying a strain of 4%, causes a shift in the transformation temperatures which corresponds to an internal stress of 100 MPa. An additional externally applied stress of 100 MPa over the existing 100 MPa internal stress causes the A_f transformation temperature to correspond to a 200 MPa applied stress level. This shift in the transformation temperatures both at 10 MPa, as noted from Fig. 19, as well as at 100 MPa, as shown from the current test shows that the plasticity due to detwinning does not cause a shift in just the transformation temperatures but in the entire phase transformation surfaces of the alloy. Additionally, it must also be noted that in the case of non-uniform stress distribution within the material, all the transformation temperatures in the phase diagram will not shift equally.

This shift in the phase transformation surfaces along this loading path shows that

the internal stress due to detwinning must also be accounted for during the thermally induced phase transformation to predict the correct transformation start and finish temperatures. The shift of the transformation surfaces due to detwinning can be determined by calibrating the internal stress (from the transformation temperatures) as a function of the applied stress in the material.

To study the effect of different applied strains on the subsequent material actuation strain generated at different stress levels, a parametric study was conducted. Under applied strains of 4%, 4.5% and 5%, the actuation behavior at 100, 150 and 200 MPa was studied. A typical stress-strain diagram for such a loading path is shown in Fig. 22. The case shown in Fig. 22 is for the 4% applied strain case followed by actuation at 100 MPa. In subsequent cycles, following detwinning, thermal actuation occurs at 150 and 200 MPa. The stress-strain data for all the other actuation test cases (different applied strains followed by actuation at different stress levels) is shown in Appendix B.

The actuation strain for different applied strains at different actuation stress levels is shown in Fig. 23. From Fig. 23, it is noticed that the actuation strain for an applied strain of 3.5% is the least at all stress levels. This low actuation strain may be associated with the insufficient variant reorientation that occurs with a 3.5% strain. For strain values of 4, 4.5 and 5%, the actuation strains remain constant for stress levels of 100 and 150 MPa but, for the 4.5 and 5% strain values, decreases at 200 MPa. The decrease in actuation at 200 MPa may be associated with the irrecoverable plastic strains that occur due to dislocations (when detwinned to 4.5 and 5%) that hinder variant reorientation resulting in a decreased actuation strain. Based on the observed actuation response, the 4% applied strain was chosen for the cyclic actuation study along this loading path.

From the parametric study, actuation at 100 MPa following a prestrain to 4% was

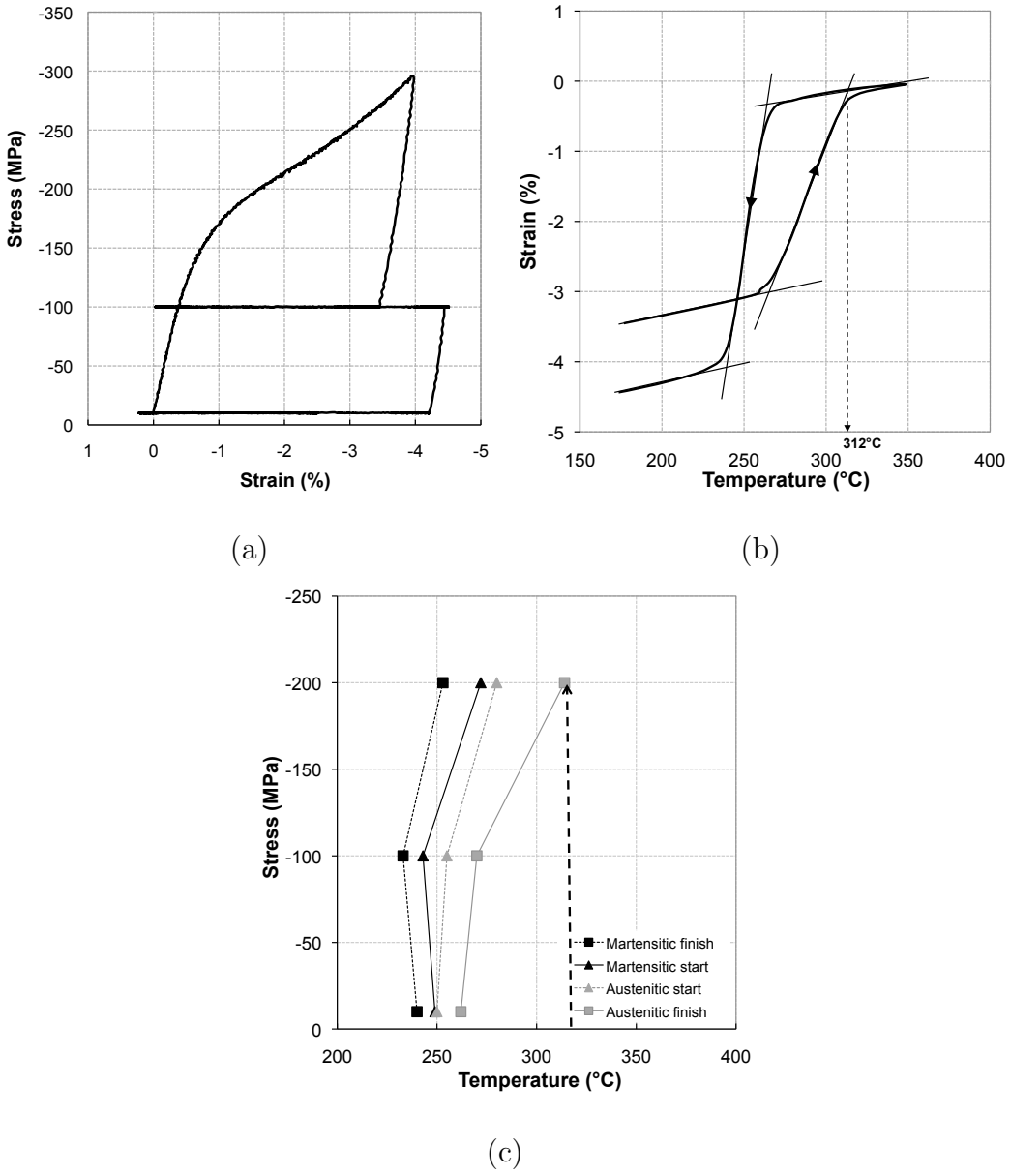

Fig. 21. Data from the 4% applied strain followed by unloading and actuation at 100 MPa; **(a)** Stress-strain diagram showing the detwinning to 4% strain followed by the unloading to 100 MPa and thermal actuation under constant stress; **(b)** strain-temperature diagram showing the actuation cycle at 100 MPa and the measured A_f temperature from the cycle; **(c)** Phase diagram with the A_f temperature measured at 100 MPa mapped to the corresponding internal stress, which for the current temperature is approximately 200 MPa.

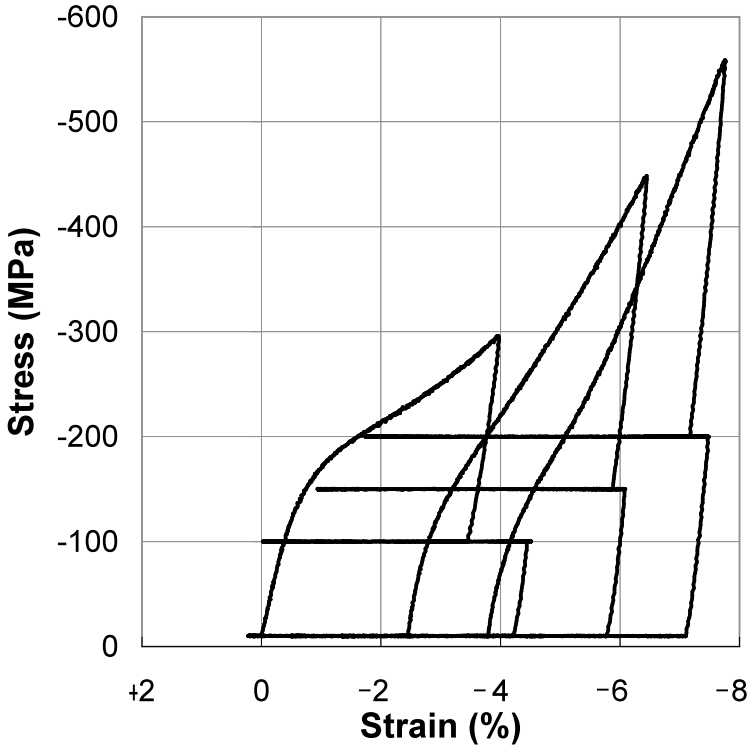

Fig. 22. Stress-strain diagram showing the detwinning by a 4% applied strain followed by unloading and actuation at 100 MPa. Following the actuation the specimen is unloaded to 10 MPa and one thermal cycle is conducted to recover any remnant detwinned martensite. The loading path is then repeated with subsequent actuation cycles at 150 and 200 MPa.

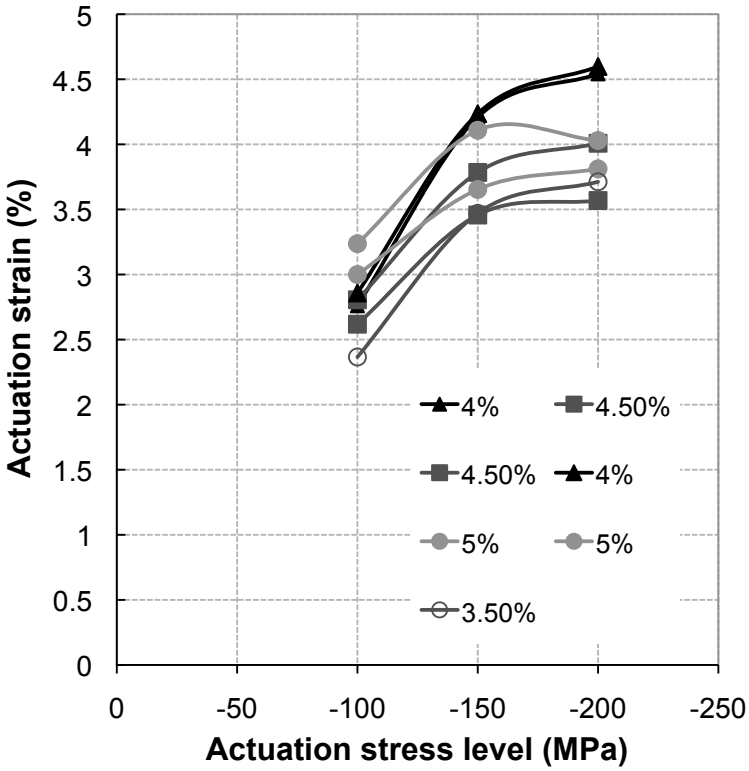

Fig. 23. Actuation strain values from the parametric study for different applied strain values of 4%, 4.5% and 5% strain and actuation stress levels of 100, 150 and 200 MPa.

chosen and the cyclic actuation studies were conducted. Following the pre-straining to 4%, the specimen was unloaded to 100 MPa stress and thermally actuated under constant stress. The specimen was then unloaded and one thermal cycle was conducted to recover any residual martensite. The described loading path was repeated for 10 consecutive thermal cycles and the stress-strain behavior is shown in Fig. 24a. The actuation strain and the irrecoverable strain at the end of the each thermal cycle was recorded and is shown in Fig. 24b. From the result it is observed that the specimen generates a consistent 4% actuation strain for 9 cycles following which the actuation strain begins to decrease. The actuation strain of 4% is 1% higher than what was observed in the constant stress, thermal cycling behavior. This is because

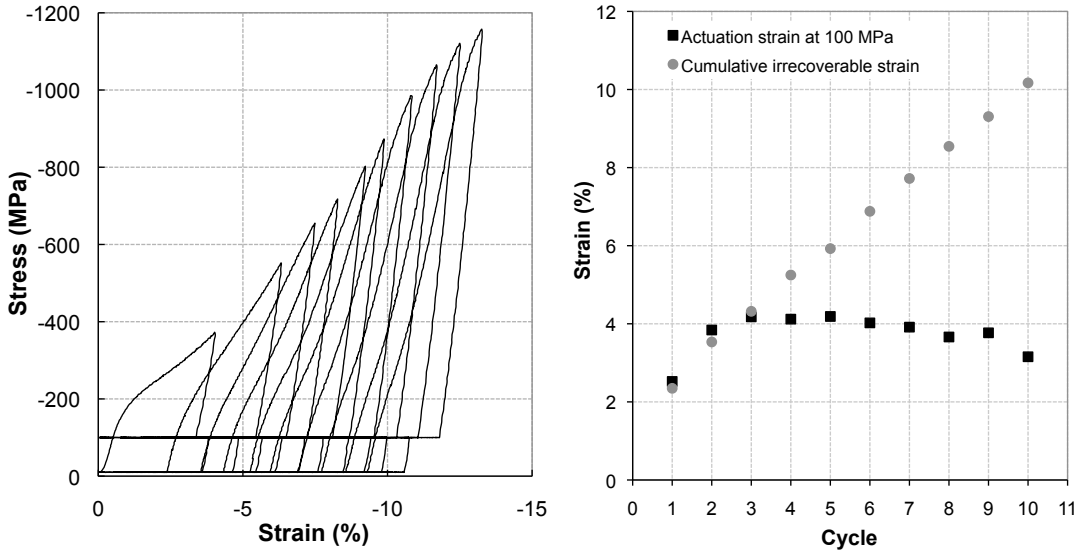

(a) (b)

Fig. 24. Cycling actuation behavior; **(a)** Stress-strain diagram showing 10 consecutive cycles of detwinning to 4% strain followed by unloading and actuating at 100 MPa; **(b)** The actuation strain generated in each cycle along with the cumulative plastic strain in the material after each cycle.

the pre-strain applied to the specimen helps in re-orienting additional martensitic variants, thus providing a higher actuation strain for the same actuation stress level. However, the cyclic detwinning of the alloys causes accumulation of plastic strain, which in turn results in hardening and an increase in the maximum stress achieved in each subsequent cycle. As a result, towards cycle 10, yielding begins to occur leading to a decrease in the actuation strain.

C. Summary and Conclusions

Thermomechanical tests were conducted on $Ti_{50}Pd_{30}Ni_{20}$ HTSMA along two different actuation loading paths. The study revealed that constant stress, thermal cycling

leads to a stabilization of the actuation behavior rapidly at a lower stress level (100 MPa) and at higher stress levels of 200 and 500 MPa stabilization in the actuation behavior was not observed over the duration of the cycles performed. Additionally an increase in the transformation temperatures is observed, signifying an accumulation of internal stresses with the increase in thermal cycles. A consequence of the constant stress thermal cycling is the increase in the stable TWSME. The TWSME behavior saturates to a fixed value with the stabilization of the actuation behavior under constant stress.

In the case of the constant strain loading path, a higher actuation strain is attainable for a given actuation stress level when compared to the constant stress, thermal cycling loading path. But it is noticed that the plasticity that occurs simultaneously with the pre-straining (i.e. detwinning) causes not just a shift in the transformation temperatures but in all the transformation surfaces in the phase diagram. Additionally the hardening caused due to the plasticity increases the stress level achieved for the same applied strain in subsequent cycles. This results in fewer actuation cycles compared to the constant stress thermal cycling path, because the stress level reaches the yield stress. Further, the accumulation of internal stresses leading to a shift in the transformation surfaces necessitates a knowledge of the variation of the transformation temperatures with accumulated internal stresses in order to determine the end point of heating during a certain actuation cycle. This accumulated internal stress can be quantified by plotting the internal stress generated during detwinning as a function of the maximum stress applied during detwinning.

CHAPTER III

EFFECT OF VISCOPLASTIC BEHAVIOR ON THE ACTUATION BEHAVIOR $TI_{50}PD_{40}NI_{10}$ HIGH TEMPERATURE SHAPE MEMORY ALLOY[1]

In this chapter, the influence of viscoplasticity on the transformation behavior of a HTSMA (in this case $Ti_{50}Pd_{40}Ni_{10}$) is studied using thermomechanical testing and transmission electron microscopy. For this purpose, an ingot of the alloy is fabricated by vacuum arc melting, hot rolling and then cutting cylindrical specimens for compression tests from the rolled bar. Standard creep tests to determine the creep behavior of the alloy and thermally induced phase transformation tests are conducted to observed the simultaneous viscoplastic and transformation behavior usinga custom high temperature test setup. Thin sections from the as-received material are prepared and test specimens for examining the microstructure by transmission electron microscopy. Based on the thermomechanical tests and the microstructural observations, the impact of transformation induced plasticity (TRIP) and viscoplasticity on the actuation behavior of the HTSMA is discussed.

A. Material Selection and Experimental Method

To capture the simultaneous viscoplastic and transformation behavior, it was necessary to choose an alloy in which creep mechanisms would occur during the course of transformation. For this purpose $Ti_{50}Pd_{40}Ni_{10}$ was chosen for the study because of its

[1]Portions of this chapter have been reproduced from "P. K. Kumar and D. C. Lagoudas, Experimental and Microstructural Characterization of Simultaneous Creep, Plasticity and Phase Transformation in $Ti_{50}Pd_{40}Ni_{10}$ High Temperature Shape Memory Alloy", Acta Materialia, 2009 (in print), with permission from Elsevier.

transformation temperatures which lie between 350-500°C. This is essential as these transformation temperatures lie within 0.3 to 0.5 of its melting temperature (1600K), a range where viscoplastic behavior typically initiates in metallic systems, suggesting the possibility of creep occurring during transformation [41, 42]. An ingot of the alloy was fabricated by melting individual quantities of metals with purity 99.99% Ti, 99.95% Pd and 99.95% Ni in a water cooled copper hearth. The vacuum arc melt alloy was cast and homogenized for 5 hours at 1000°C in vacuum. The cast bar was then hot rolled at 900°C such that its thickness was reduced by 30%. The phase transformation temperatures of the rolled alloy were measured by examining a small section of the alloy (cut with a low speed diamond saw) using a Differential Scanning Calorimeter (DSC). The transformation temperatures determined from the DSC data by the tangent intersection method are, martensitic finish=360°C, martensitic start=388°C, austenitic start=392°C, and austenitic finish=411°C. Seven cylindrical specimens, each 12 mm in length and 6 mm in diameter were cut by electrical discharge machining.

The thermomechanical tests on the compression specimens were performed using a high temperature test setup assembled on a MTS uniaxial test frame. The assembled test setup is shown in Fig. 25. The compression grips on the setup were made out of Inconel, a material which retains its hardness at the high test temperatures. The grips and the specimen were enclosed in a quad lamp elliptical furnace equipped with a temperature controller. The specimen temperature was measured by a thermocouple mounted on the specimen surface and this gave feedback to the controller which in turn adjusted the lamp intensity. The strain on the specimen was measured by a high temperature extensometer of a known gauge length. The ceramic leads of the extensometer were mounted on the grips while the electronics of the extensometer itself were mounted outside the furnace on the frame. The thermal expansion within

the gauge length of the grips were subtracted from the total displacement measured by the extensometer and the displacement and strain from the HTSMA was recorded. Both the extensometer and furnace were water cooled. The load cell measuring the force on the HTSMA was isolated from the furnace by a water cooled jacket. The force, strain, time and temperature during the test were recorded using the MTS software.

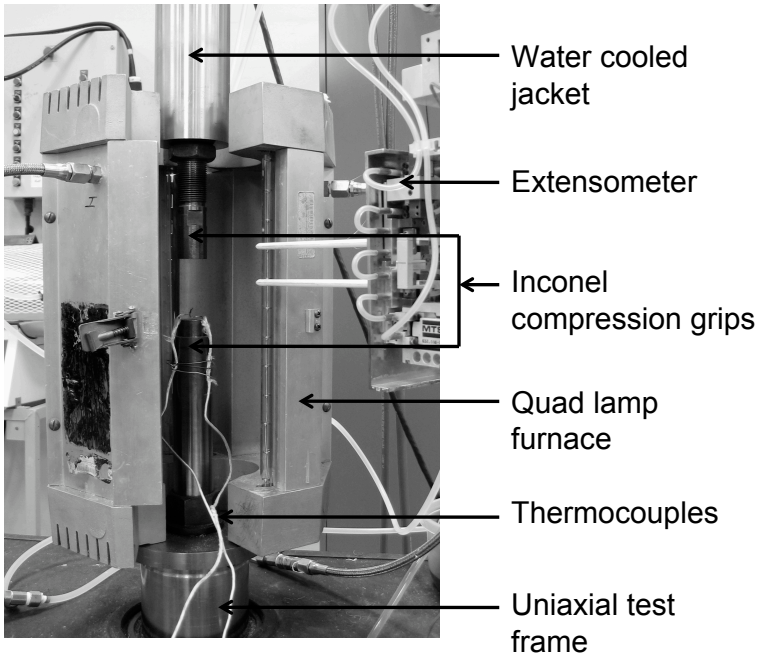

Fig. 25. Thermomechanical test setup showing a uniaxial test frame fitted with a water-cooled furnace, extensometer and Inconel grips for testing at high temperatures.

The high temperature test setup was used to conduct the thermomechanical tests on the compression specimens. Three sets of tests were conducted on the specimen. The first set of tests included uniaxial tests and one thermal cycle to understand the preliminary transformation behavior of the as-processed alloy. Following this, creep tests were conducted at two different stress levels chosen based on the uniaxial

test data. The third set of tests involved constant stress thermal cycling at different heating/cooling rates to capture the simultaneous viscoplastic and transformation behavior of the HTSMA. Test matrices listing all the tests are shown in Table V, Table VI and Table VII. To determine the behavior of the austenite and martensite phases, preliminary uniaxial tests were conducted at room temperature (martensitic state) and at 520°C (austenitic state). For the uniaxial test the specimen was initially held under a constant compressive stress of 5 MPa at the test temperature. Holding the temperature constant, the specimen was loaded at a constant displacement rate equivalent to an initial strain rate of 10^{-4}/sec. The results from the initial uniaxial tests in the martensitic and austenitic states are shown in Fig. 26a. From the uniaxial test in martensite it is observed that martensite reorientation initiates at approximately 300 MPa and macroscopic yielding in the specimen is observed at approximately 1300 MPa. From the austenite response, we observe that yielding occurs at approximately 250 MPa. During the unloading of austenite a preliminary strain increase is observed indicating the influence of viscoplastic behavior. Based on the uniaxial tests, stresses of 200 and 100 MPa were chosen for the creep and thermally induced phase transformation tests. In addition to the uniaxial tests, a thermal cycle under a constant applied stress of 5 MPa was conducted. The strain-temperature response for the constant stress thermal cycle is shown in Fig. 26b. The result shows that the material exhibits a 0.7% fully recoverable transformation strain in the as-processed state.

Table V. Test matrix for $Ti_{50}Pd_{40}Ni_{10}$ - Preliminary compression tests.

Test #	Test type	Applied stress	Temperature	Loading rate
1	Uniaxial loading	-	Room temp.	10^{-4}/sec
2	Uniaxial loading	-	520°C	10^{-4}/sec
3	Thermal cycling	5 MPa	520-300°C	2°C/min

Table VI. Test matrix for $Ti_{50}Pd_{40}Ni_{10}$ - Compression creep tests.

Test #	Test type	Applied stress	Temperature	Loading rate
4	Creep test	200 MPa	520°C	-
	Thermal cycling	5 MPa	520-300°C	2°C/min
5	Creep test	100 MPa	520°C	-
	Thermal cycling	5 MPa	520-300°C	2°C/min

Table VII. Test matrix for $Ti_{50}Pd_{40}Ni_{10}$ - Compression constant stress thermal cycling tests.

Test #	Test type	Applied stress	Temperature	Loading rate
6	Thermal cycling	200 MPa	520-300°C	2°C/min
	Thermal cycling	100 MPa	520-300°C	2°C/min
	Thermal cycling	5 MPa	520-300°C	2°C/min
7	Thermal cycling	200 MPa	520-300°C	20°C/min
	Thermal cycling	100 MPa	520-300°C	20°C/min
	Thermal cycling	5 MPa	520-300°C	2°C/min

1. Creep Tests

The creep tests at both stress levels (200 and 100 MPa), chosen based on the uniaxial tests (Table VI) were conducted at a temperature of 520°C. Since 520°C, corresponds to approximately half the absolute melting temperature, creep was expected to be observed. For these tests, the specimen was initially held under a constant compressive stress of 5 MPa at the test temperature (520°C). Holding isothermal conditions, the specimen was loaded to the desired stress level at 500N/sec. This loading rate was

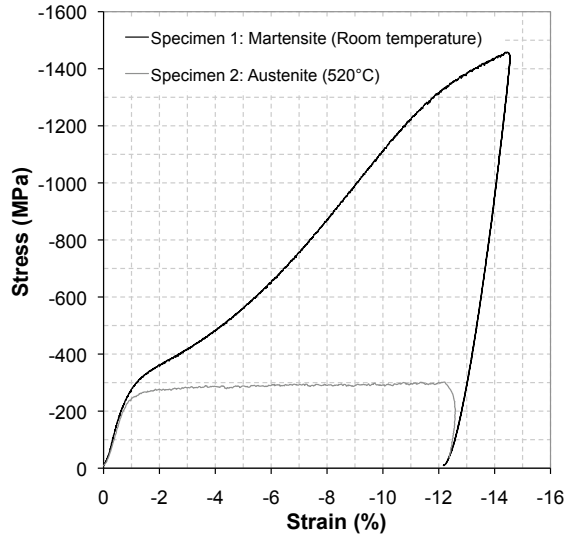

(a)

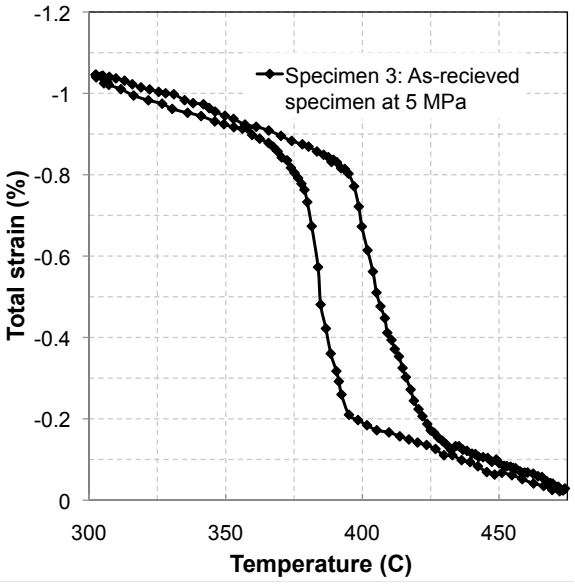

(b)

Fig. 26. **(a)** Uniaxial compression test results in the austenitic and martensitic state for $Ti_{50}Pd_{40}Ni_{10}$ HTSMA. **(b)** Strain-temperature diagram showing the transformation behavior in the as-recieved specimen under a compressive stress of 5 MPa.

fast enough to avoid the influence of creep effects and slow enough to avoid inertial effects. Once the stress level was achieved, the stress was held constant for a period of approximately 2.5 hours and the creep strain evolution with time was recorded, following which the specimen was unloaded to 5 MPa. To observe the effect of the viscoplastic strain generated during the creep test, one thermal cycle (rate of heating/cooling: 2°C/min) at a constant compressive stress of 5 MPa was conducted and the response was compared with the as-processed material behavior. The test was performed at the two stress levels - 100 and 200 MPa (Table VI). Following the thermomechanical tests, thin sections from the 200 MPa creep specimen were machined by low speed diamond saw and TEM specimens were prepared for observation.

2. Constant Stress Thermal Cycling Tests

To study the simultaneous creep and transformation behavior, constant stress thermal cycling was conducted at stress levels of 200 and 100 MPa (specimen 6 and 7 in Table VII). For this test, specimen 6 was initially heated to 520°C under a preload of 5 MPa. This was set as the reference point for the test. The specimen was then loaded to 200 MPa under isothermal condition and holding the stress constant, the specimen was thermally cycled between 520-300°C at 2°C/min. To observe the transformation behavior with a smaller influence of the viscoplastic behavior, the specimen was then unloaded to 100 MPa and a thermal cycle was conducted at the same cooling/heating rate. The specimen was then unloaded and one thermal cycle was conducted at a compressive stress of 5 MPa with a heating/cooling rate of 2°C/min to observe the influence of the simultaneous transformation and viscoplastic behavior on the transformation behavior at 5 MPa. The above loading path was repeated on specimen 7 with a heating/cooling rate of 20°C/min to observe the influence of thermal cycling rate. After the thermomechanical tests, TEM specimens were prepared from the

specimen thermally cycled at a 20°C/min for observing the microstructure in the martensitic and austenitic states.

3. Microstructural Investigation

From the as-received specimen (specimen 3), the 200 MPa creep specimen (specimen 4) and the 20°C/min thermally cycled specimen (specimen 7), thin sections were cut using a low speed diamond saw and specimens were prepared for observation using Transmission Electron Microscopy (TEM). The sections were polished down to 70μm, following which, 3mm discs were punched out from the polished sheets. The discs were dimpled with a 9 micron diamond solution. The central section of the disc was then polished to create a small hole using a Fishione model 1010 low angle ion mill. The samples were then examined with a JEOL 2010 TEM equipped with a heating stage. The microstructure was observed at room temperature (in the martensitic state) and at 523°C and 640°C (austenitic state). Electron Dispersive Spectroscopy (EDS) were Selected Area Diffraction (SAD) was used to index and identify the different phases and regions.

B. Thermomechanical Test Results

1. Creep Test Results

The creep strains generated with time from the creep tests conducted on specimens 4 and 5 (Table VI), are shown in Fig. 27a. The results from the creep tests show that the material enters secondary steady state creep within 15 minutes of the start of the test. Over the 2.5 hour duration, the total irrecoverable creep strain accumulated during the 200 and 100 MPa creep tests are 12.4% and 1.2% and the corresponding steady state creep rates are 1.44 x 10^{-5}/sec and 9.2 x 10^{-7}/sec, respectively. With

the known steady state creep rates and stress levels from the two creep tests (at a test temperature of 520°C), the stress exponent is determined using equation 3.1 where Q is the activation energy, R is the gas constant (R = 0.00831KJ $K^{-1}mol^{-1}$), A is a material constant, and T is the absolute temperature. From the two creep results the steady state creep rates are substituted and the value of the stress exponent is calculated as N_a=4.

$$\dot{\varepsilon} = A\sigma^{N_a} e^{-Q/RT} \tag{3.1}$$

Following the creep tests, the strain-temperature responses from the thermal cycles at a constant stress of 5MPa were compared with the as-processed material behavior (Fig. 27b). From the strain-temperature response in Fig. 27b, it is observed that the transformation behavior for the specimens after the creep tests remains unaltered when compared to the as-processed material behavior even for the 200 MPa creep case where a total irrecoverable viscoplastic strain of 12.4% was generated during the creep test.

2. Constant Stress Thermal Cycling Results

The results (strain-temperature) from the constant stress thermal cycling conducted on specimens 6 and 7 (at stresses of 200 and 100 MPa) are shown in Fig. 28a and Fig. 28b, respectively. From Fig. 28a (specimen 6), it is observed that as the specimen cools at 200 MPa, in the austenitic state, the strain evolution from the point A to B takes a curved path. Following the cooling in austenite, the phase transformation from austenite to martensite initiates at point B. As the cooling continues, the forward transformation is completed at point C and the specimen is cooled in the purely martensite state down to 300°C. As the material is heated in the martensitic

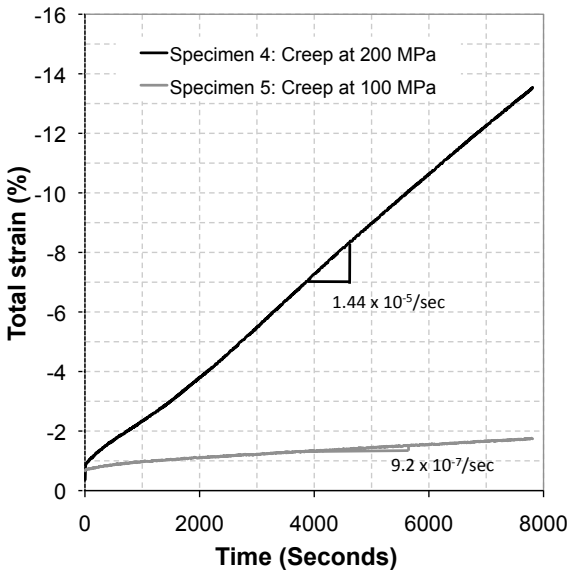

(a)

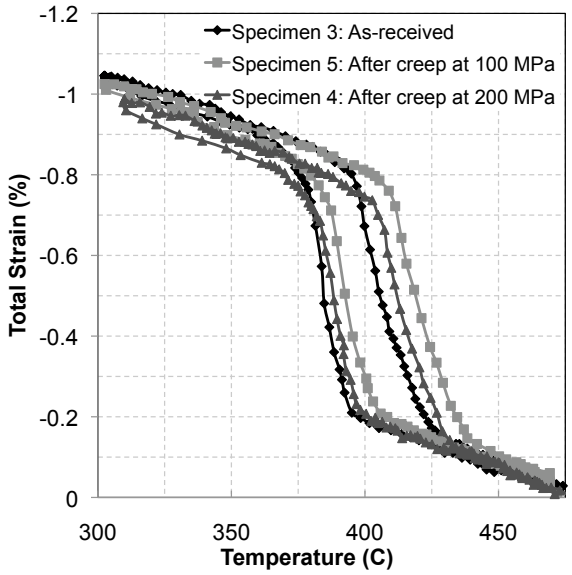

(b)

Fig. 27. **(a)** Strain-time plot showing the creep strain evolution at stress levels of 100 and 200 MPa at a temperature of 520°C. **(b)** Strain-temperature diagram comparing the TWSME after the creep tests with the as-recieved material behavior.

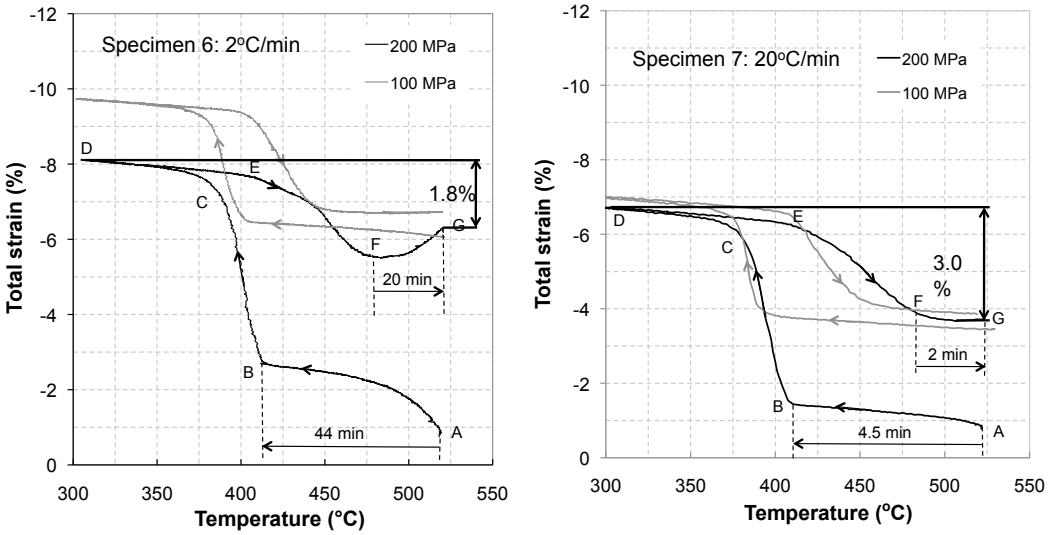

(a) (b)

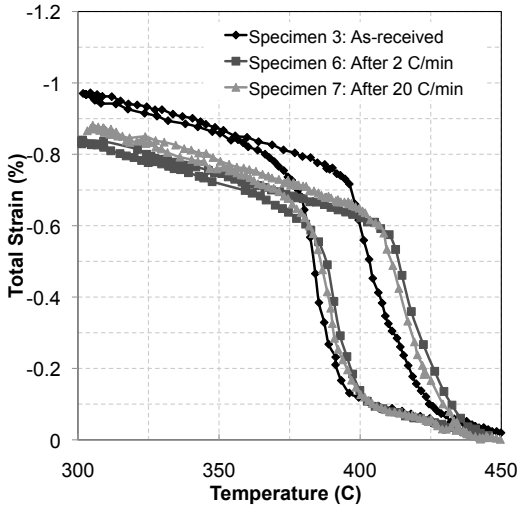

(c)

Fig. 28. Strain-temperature behavior **(a)** of the specimen thermally cycled at 2°C/min at 200 and 100 MPa stress levels; **(b)** of the specimen thermally cycled at 20°C/min at 200 and 100 MPa stress levels; **(c)** comparing the TWSME compared before and after the thermal cycling at different cooling/heating rates with the as-received material behavior.

state from the point D to E, a linear behavior is observed which is contrary to the behavior observed during the cooling in the austenite phase (AB) although both the heating (DE) and cooling (AB) paths take 45 minutes. Upon further heating, the reverse transformation initiates at E and the shape recovery begins. Upon reaching a temperature of approximately 480°C (point F), the strain recovery begins to diminish and the material contracts along the direction of the applied stress (path FG). The heating from F to G occurs over approximately 20 minutes. The behavior observed in specimen 7 (Fig. 28b) at a stress of 200 MPa exhibits a similar trend during the heating and cooling, but the behavior is less pronounced. In the case of specimen 7, with a heating/cooling rate of 20°C/min, the time to cool from A to D or heat from D to G is reduced by a factor of ten.

From the thermal cycling test results conducted at 200 MPa at the two different heating/cooling rates (specimens 6 and 7), the actuation strain (strain during the heating path D to G) and the total irrecoverable (the difference between strain at A and G) strains are calculated and compared. For specimens 6 and 7, the actuation strains at 200 MPa are calculated as approximately 1.8% and 3.0% and are shown in Fig. 28a and Fig. 28b, respectively. At the same stress level of 200 MPa, the irrecoverable strain generated is specimen 6 and 7 are also calculated as 5.3% and 2.8%, respectively.

The strain-temperature behavior at 5 MPa for specimens 6 and 7, after being thermal cycling at 2°C/min and 20°C/min, is compared with the as-processed specimen behavior in Fig. 28c. The results indicated that the transformation strain in the tested specimens (6 and 7) decreased by approximately 20% even though the total irrecoverable strain generated in each case is different. It is also noticed that the total irrecoverable strain generated during the isothermal creep test at 200 MPa shows no change in the transformation behavior at 5 MPa after the creep tests (Fig. 27b), even

though the permanent irrecoverable strain (during the creep tests) is higher than the irrecoverable strain generated in the thermal cycling tests (Fig. 28a and Fig. 28b).

C. Results from Microstructural Investigation

1. Microstructure of the As-received Specimen

Thin sections were prepared from the as-received sample for observation under the TEM. The TEM micrograph from the as-received specimen in the martensitic state (room temperature) is shown in Fig. 29. The zoomed-in interface between two variants and the indexed SAD patterns for the interface region is shown next to the micrograph. The lattice structure of martensite is determined to be B19 orthorhombic martensite, and from the SAD patterns it is observed that the material is primarily comprised of {111} type I Lattice Invariant Shear (LIS) twins (LIS plane is the plane along which shear occurs to form twins during self accommodation). In the micrograph shown in Fig. 29, the matrix and the corresponding twin are shown as two sets of reflections which possess a mirror symmetry about the {111} plane when viewed from the [112] zone axis. Smaller regions comprised of {110} type compound twins were also observed in the microstructure (not shown here). The twinning observed in the $Ti_{50}Pd_{40}Ni_{10}$ microstructure in the current study is similar to those observed in the high Pd content alloys from the work of [43, 44].

2. Microstructure After Creep at 200 MPa

The 200 MPa creep samples was sectioned and prepared for observation in the TEM. The specimen was observed in the martensitic state and the austenite state and the micrographs are shown in Fig. 30 and Fig. 31, respectively. The microstructure of the martensitic state is comprised of martensite with both a spear-like morphology

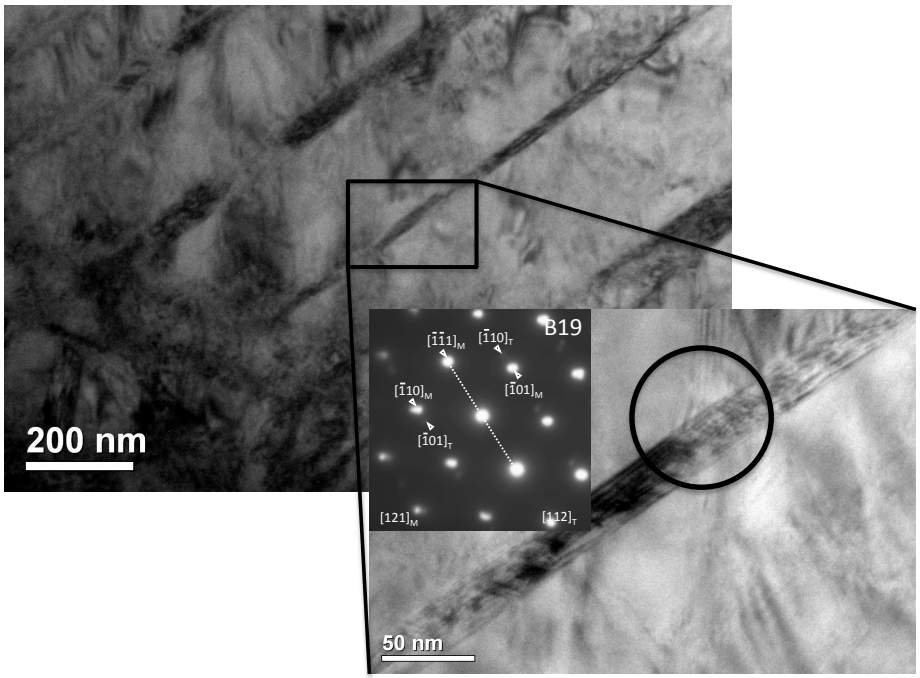

Fig. 29. As-recieved specimen microstructure showing the {111} type I twins observed predominantly in the microstructure.

as well as parallel internal twinned lamellae structure. The twins in the lamellae run diagonally through the width of the martensite plate and alternate twins appear to have the same orientation and width. The martensite structure was identified as B19 orthorhombic and SAD pattens were taken from different regions to identify the type of twinning. The regions and their corresponding SAD patterns are also shown in each micrograph. From the indexed SAD patterns in the martensitic state (Fig. 30a), it is observed that regions 1, 4 and 6 show {011} compound twin structure. These compound twins are predominantly present in the microstructure and are comprised of two sets of reflections which are in mirror symmetry about the {110} plane when viewed from the [100] zone axis. Regions 2 and 3 show {111} Type I twinning which is characterized by two sets of reflections in mirror symmetry about the {111} plane when viewed from the [011] zone axis. Fully detwinned martensite is also observed in region 5. The martensitic microstructure shows regions of both well arranged (Fig. 30b) as well randomly formed twins. The markers A and B in Fig. 30b indicate disappeared twins in the martensitic variant. The region in Fig. 30b was heated to 523°C (80°C above austenite finish) and the resulting microstructure is shown in Fig. 31. The SAD patterns are indexed to a austenite B2 cubic microstructure indicating that the specimen has completely transformed from the product to the parent phase. In the austenitic state an "imprint" is observed that appears to show the same contrast as shown by the martensite twins, although the sample is completely in the austenitic state.

3. Microstructure After Thermal Cycling at 20°C/min

The micrographs for the martensite and austenite microstructures from the 20°C/min constant stress thermally cycled specimen (specimen 7) are shown in Fig. 32 and Fig. 33, respectively. The martensitic microstructure from the simultaneous creep

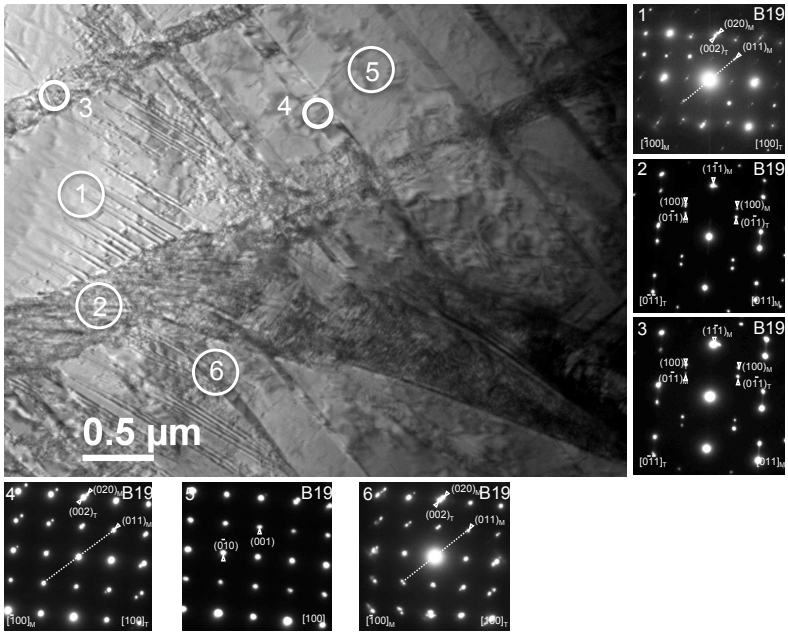

(a)

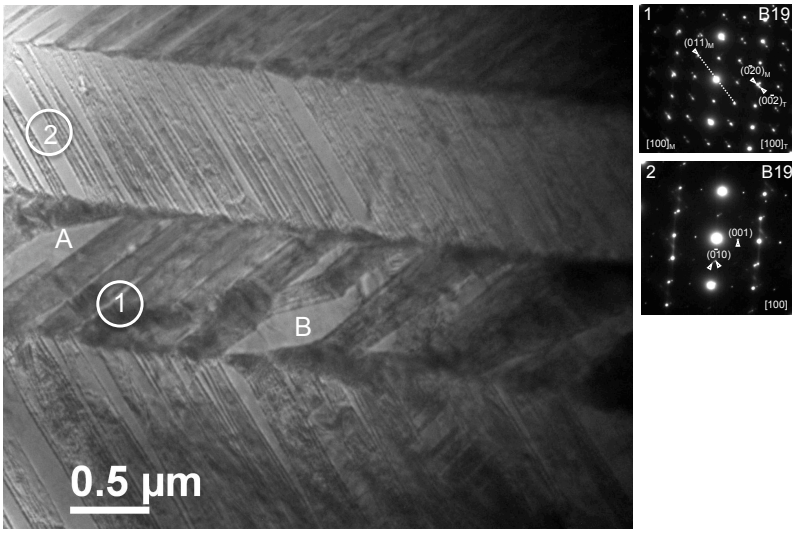

(b)

Fig. 30. TEM image of the specimen after the creep test at 200 MPa **(a)** martensitic structure in a regions showing {011} compound twins (1, 4, and 6), smaller regions of {111} type I twinning (2, 3) and fully detwinned martensite (5); **(b)** Another region in the specimen showing compound twins and within them the disappearance of some twins in regions A and B.

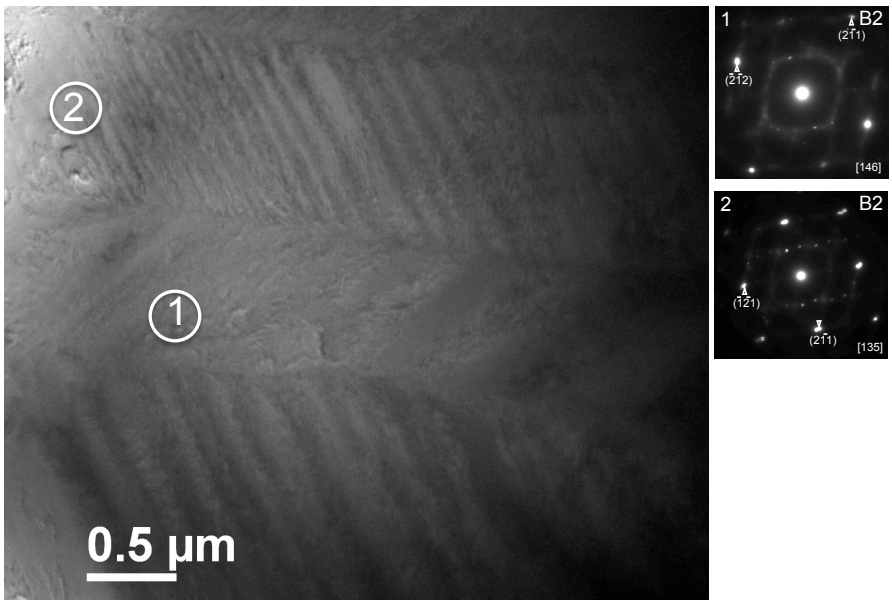

Fig. 31. Region observed in Fig.30b after heating to 523°C. Regions 1 and 2 have completely transformed to austenite.

and transformation specimen shows the same lamellar internally twinned martensite variants as observed in the pure creep specimens (Fig.30). However, in the simultaneous creep and transformation specimen the martensite variants throughout the specimen, are large and continuous with clear twin boundaries unlike what is observed in the pure creep specimen. {111} type I twins are more predominantly observed in the thermally cycled specimen's microstructure along with {110} compound twins (Fig. 32a and Fig. 32b). A specific region of the specimen, the region shown in Fig. 32b, is heated to a temperature of 520°C (Fig. 33a), and the indexed SAD patterns show that the areas 6 and 7 transform completely to austenite. However, the regions 3, 4 and 5, are indexed to the martensitic structure indicating that the entire specimen does not transform to austenite and continue to remain in the martensitic state. It is also observed that regions 3, 4 and 5 appear to be enclosed by a thin band

of piled or pinned dislocations. Upon heating the specimen to 640°C (Fig. 33b), the band begins to disappear and region 5 transforms to austenite while region 3 remains in martensitic state. Additional TEM micrographs from the 200 MPa creep specimen and the thermally cycled specimen (at 20°C/min) are shown in Appendix C.

D. Discussion

From the creep tests conducted at 200 and 100 MPa on specimens 4 and 5, the steady state creep rates show good agreement to the rates observed in Ni-rich 50.7at% NiTi alloys [38, 45] under similar stress and temperature conditions. The creep rates and exponent for the NiTi SMAs tested at similar temperatures and stresses are shown in Table VIII. Using the creep rates from the creep tests (conducted at fixed stress and temp conditions) in equation 1, the stress exponent value can be determined. For the present material system, the stress exponent is calculated as N_a=4. Based on the calculated stress exponent the dominant active creep mechanism can be determined. With a N_a of 4, the dominant active microstructural mechanism is dislocation creep [46]. The variation of the stress exponent from other NiTi alloys compared in Table VIII is associated with the variation in the alloy composition, microstructure and probable presence of precipitates that influences the creep mechanisms in these alloys.

The electron micrograph for the specimens from the pure creep tests indicate a large presence of {110} type compound or deformation twins in the microstructure compared to the {111} twins observed in the as-recieved specimen. Such twinning has been observed in other studies on TiPdNi alloys and typically occurs at nucleation sites such as precipitates or defects [44]. In a specimen undergoing creep, permanent viscoplastic strain occurs as a result of glide of dislocations which, upon encountering an obstacle, undergo climb which is aided by thermal activation and vacancy diffu-

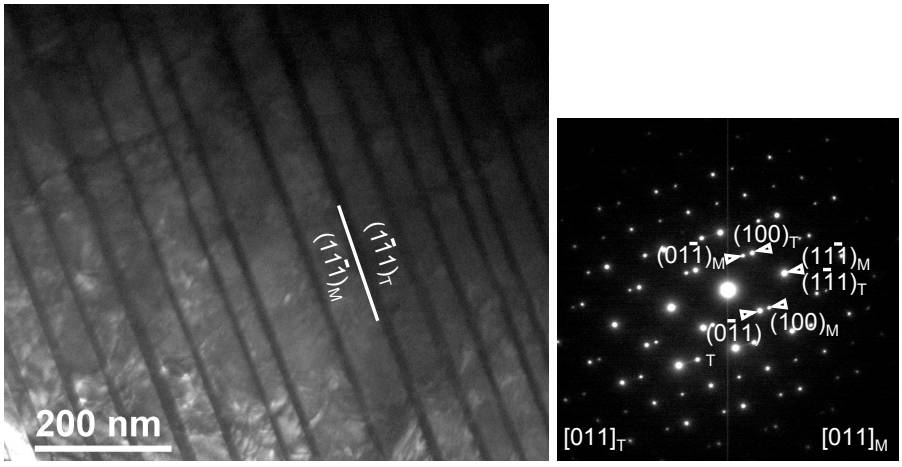

(a)

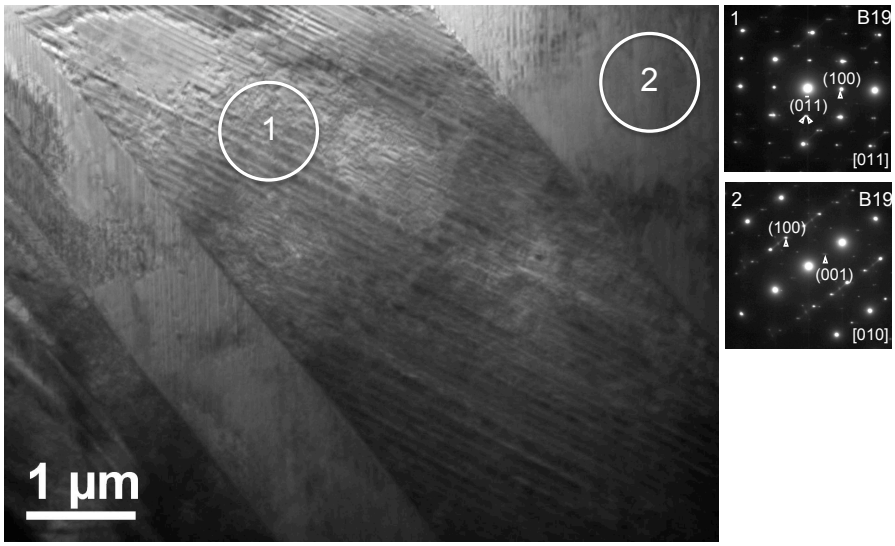

(b)

Fig. 32. TEM image of the specimen after the constant stress thermal cycling at 200 and 100 MPa at a heating/cooling rate of at 20°C/min **(a)** region showing presence of large continuous {111} type I twins; **(b)** region showing well formed continuous compound twins in the material.

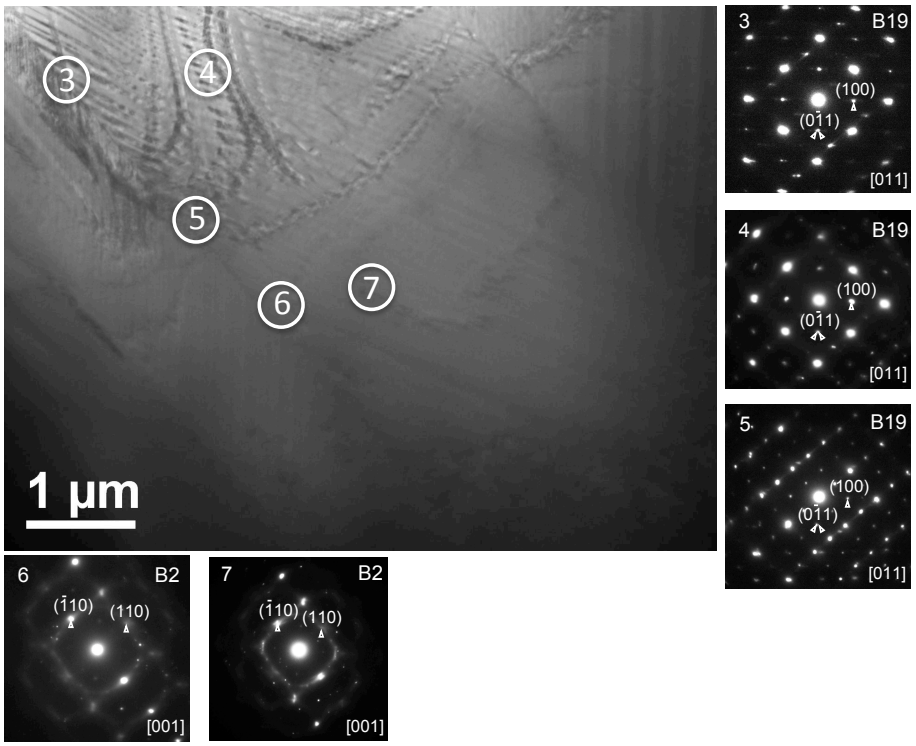

(a)

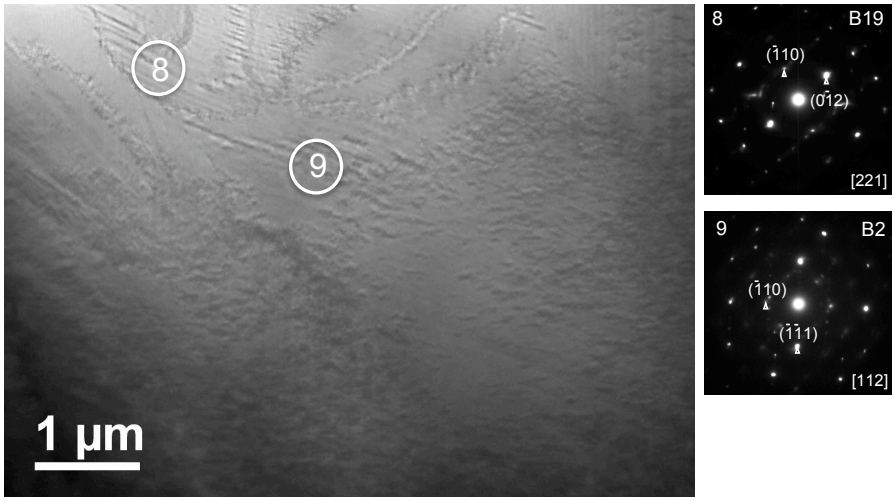

(b)

Fig. 33. TEM image of the region in (Fig. 33b) **(a)** after heating to 523°C. The SAD patterns from regions 3,4 and 5 show retained martensite while the regions 6 and 7 have transformed to austenite; **(b)** after heating to 640°C. region 8 remains in martensite and regions 9 has transformed to austenite.

Table VIII. Summary of creep parameters from the creep tests on NiTi in the literature conducted at similar temperature and stress conditions compared with the values from the current work.

Temperature (°C)	Strain rate (sec^{-1})	Stress (MPa)	N_a	Alloy	Reference
470-530	$2{\cdot}10^{-9}$-$8{\cdot}10^{-6}$	90-150	2	$Ni_{50.7}Ti_{49.3}$	[38]
500-560	$2{\cdot}10^{-7}$-$3{\cdot}10^{-5}$	120-180	5	$Ni_{50.7}Ti_{49.3}$	[45]
520	$9.2{\cdot}10^{-7}$-$1.4{\cdot}10^{-5}$	100-200	4	$Ti_{50}Pd_{40}Ni_{10}$	Present study

sion (dislocation creep). As a consequence of such a deformation mechanism, two primary effects can occur. The first is a random distribution of dislocations throughout the material and the second is the annihilation of existing dislocation pileups (which can be induced by processing or transformation induced plasticity). In the present alloy, since the processing was conducted at 900°C, the dislocation density (or pileup of dislocations) is not as significant as in a cold rolled material. However, the random distribution of dislocations throughout the material can act as multiple nucleation sites forcing the formation of deformation/compound twins. This could be the reason for a higher density of compound twins in the microstructure. The stable transformation behavior at a stress of 5 MPa in Fig. 27b, even after the generation of 12.4% irrecoverable strain during the creep test at 200 MPa suggests that the deformation mechanisms active during the creep process over the duration of the test do not cause a change in the microstructure (e.g. relaxation of stress localizations) significant enough to affect the transformation behavior in the material.

From the constant stress thermal cycling test conducted on specimen 6 at 200 MPa, a curved path is observed during the initial cooling of austenite (AB in Fig. 28a)

and during the reverse transformation (FG). The path observed during the initial cooling from A to B is associated with the creep of the austenitic phase. Starting at 520°C, the creep initiates in the austenitic phase and as the specimen is cooled at 2°C/min, the creep continues to decrease because the creep strain rate decreases as the temperature decreases. As the forward transformation initiates at B and continues towards the martensitic phase during cooling, the creep rate decreases, causing a reduced influence of viscoplasticity on the transformation behavior at lower temperatures. Upon heating (i.e. reverse transformation) the martensite transforms to austenite. However, at higher temperatures, the overlap of the transformation temperatures with the creep regime causes viscoplastic strain generation to occur simultaneously with the transformation. As the temperature approaches 480°C, the creep strain rate begins to exceed the rate at which transformation strain is generated (which is controlled by the rate of heating). As a consequence of this increased creep rate, a portion of the actuation strain (strain generated during heating) is lost to the generated viscoplastic strain. At lower stress levels (with the same heating/cooling rate) the influence of viscoplastic strain generated on the transformation behavior is reduced due to the relatively low creep rates. For specimen 7, it is observed that the total irrecoverable strain, at the end of the thermal cycle, is significantly less and the material exhibits a much higher actuation strain during the heating cycle. These differences between the results for specimens 6 and 7 are due to the sufficiently high heating/cooling rate (for specimen 7) which means there is less time at each temperature for creep to occur. As a result, the influence of the viscoplastic strain on the transformation behavior is decreased.

From the experimental results it is evident that the impact of the viscoplastic behavior on the performance of HTSMA actuators is controlled by the heating/cooling rate. Slow heating/cooling rates could lead to complete loss of actuation. Decreasing

the thermal cycling rate from 20°C/min to 2°C/min in the present study decreases the actuation strain at 200 MPa by 50% due to the generation of an additional 2.5% irrecoverable strain due to creep. Motivated by the experimental observations, a 1-D thermodynamic model was developed to capture the interaction of viscoplasticity with the transformation behavior in HTSMAs. An assumption that the model took into account was that the transformation behavior continues to remain time independent and is not affected by the viscoplastic mechanisms.The model was calibrated using three sets of parameters related to the thermoelastic behavior, the viscoplastic behavior and the transformation behavior. Additional details regarding this work can be found in [47]. The model was validated using the 2°C/min (Fig. 34) data and the predictions of the model at a heating/cooling rate of 20°C/min (for the 200 and 100 MPa case, see Fig. 35) are compared with the experimental results from the test performed on specimen 7. The model shows very good agreement with the experimental results for the thermal cycles conducted at 200 and 100 MPa at a heating/cooling rate of 20°C/min.

With the established thermomechanical model, the loss of actuation strain due to the impact of viscoplasticity at different heating/cooling rates can be predicted for any HTSMA. As an example, for the $Ti_{50}Pd_{40}Ni_{10}$ alloy studied in this chapter, the behavior for thermal cycling at 200 MPa, with a heating/cooling rate of 1°C/min, is predicted and shown in Fig. 36. During the forward cycle, a viscoplastic strain of approximately 3% is generated in the material prior to the initiation of transformation, reducing the actuator total length (since this is a compression behavior prediction). Following this, the forward transformation initiates and is completed as the actuator is cooled to 300°C. During the reverse transformation (actuation), the strain recovery in the HTSMA continues until approximately 470°C. However at a temperatures of approximately 470°C the creep rate due to viscoplasticity begins to overcome the rate

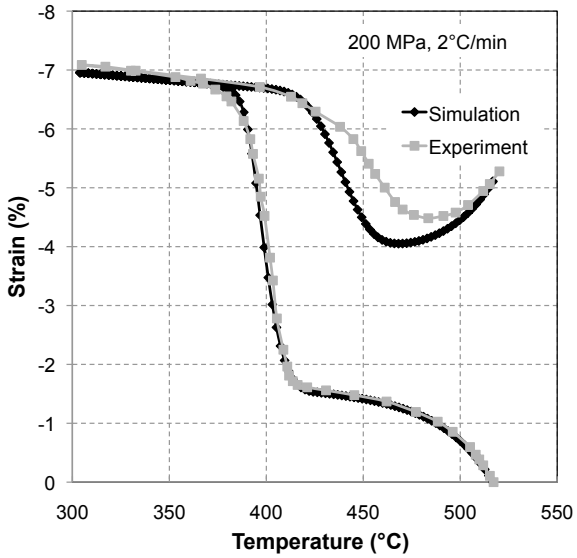

(a)

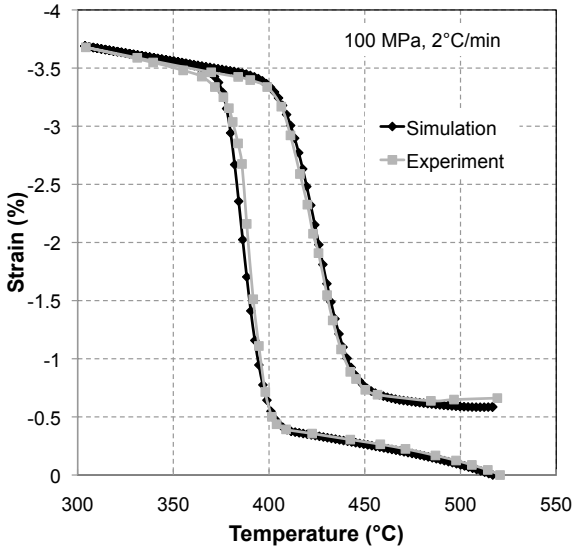

(b)

Fig. 34. Calibration of the developed thermomechanical model compared with the constant stress thermal cycling test results conducted at 2°C/min at a) 200 MPa and b) 100 MPa.

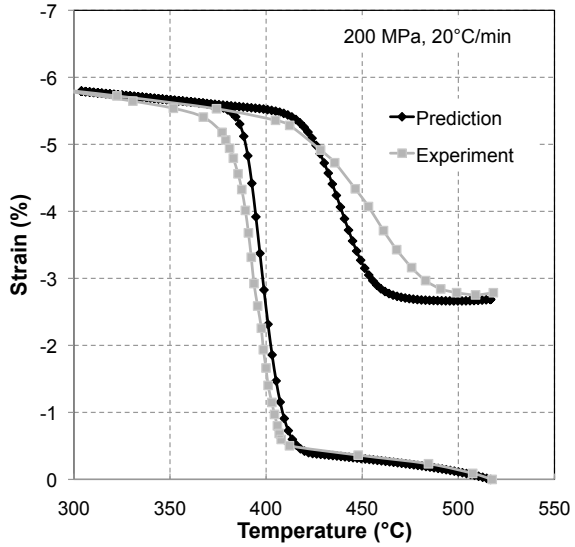

(a)

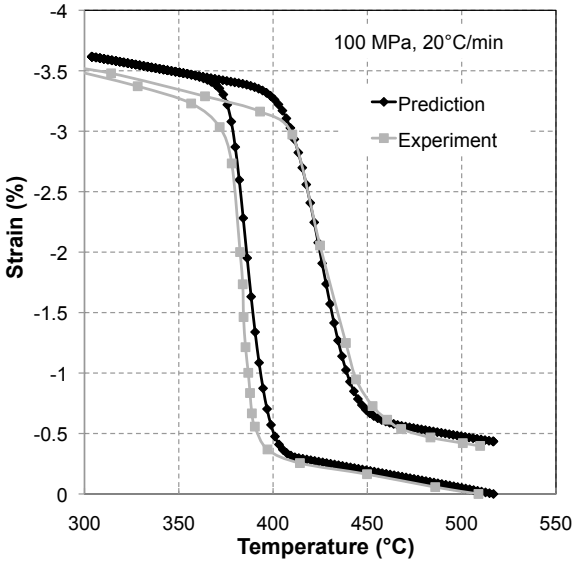

(b)

Fig. 35. Prediction of the developed thermomechanical model compared with the constant stress thermal cycling test results conducted at 20°C/min at a) 200 MPa and b) 100 MPa.

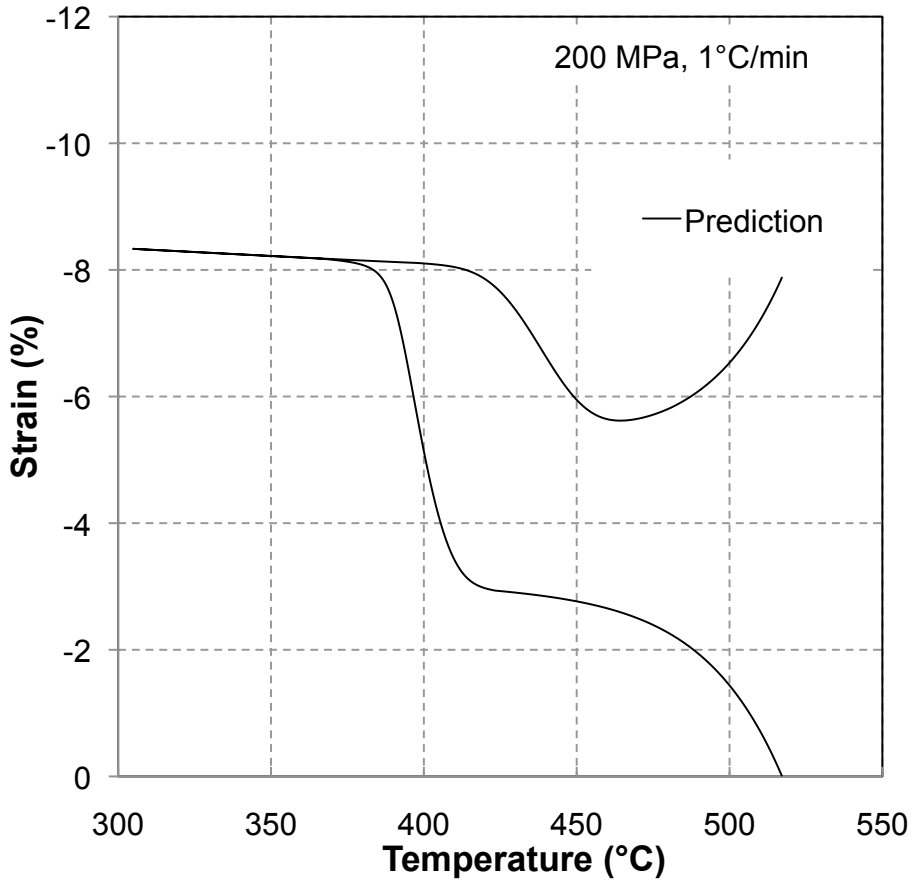

Fig. 36. Prediction of the proposed model: compressive isobaric tests conducted at 1°C/min at 200 MPa.

at which transformation occurs (which is controlled by the heating rate of 1°C/min). As a result, a complete loss of actuation is observed as the temperature is increase over the next 50 minutes.

The results from the TEM micrographs show a mixture of {111} type I twins and deformation twins [43, 48]. Upon heating, the presence of retained martensite is also observed in certain regions of the specimen. Furthermore, the results from the transformation behavior at 5 MPa also show a (Fig. 28c) decrease in the transformation strain of 20% after the thermal cycling at 200 and 100 MPa. If we look at the total

irrecoverable strain generated at the end of the fast thermal cycling test (specimen 7), the small influence of creep at such high heating/cooling rates suggests that the irrecoverable strain is predominantly caused by transformation. From earlier discussion of the creep results, it is observed that the viscoplastic strain generated does not influence the transformation behavior. Combining these observations, it can be stated that the formation of retained martensite is caused by the pinning of martensite due to dislocations developed during the course of the phase transformation. This is further supported by the evidence that some of the retained martensite begins to disappear upon heating to a higher temperature (see Fig. 33b). This retained martensite does not participate in subsequent transformation and, as a result, this can cause a decrease in the transformation strain as observed in the transformation behavior at 5 MPa. The possibility exists that more retained martensite exists in the material, and the observed decrease in the transformation strain at 5 MPa may not account for all the retained martensite present. It is also observed that the decrease in the transformation strain (Fig. 28c) at 5 MPa is identical for both thermally cycled specimens, regardless of rate, even when the permanent irrecoverable strains at the end of thermal cycling for the two cases are different (Fig. 28a and Fig. 28b). This suggests that the rate-independent irrecoverable strain generated due to transformation (resulting in the formation of retained martensite and TRIP) remains unaffected by the rate-dependent viscoplastic strain generated during the course of transformation. Finally, when the SMA is heated to austenite, a template of the martensitic twins is visible in both cases. Although such microstructures have been observed in AuCd and other NiTiPd alloys [41, 49, 50] upon aging in the martensitic state, in the present case the alloy has not been aged in martensite, but has been held in the austenitic state for a period of 2.5 hours under stress at a temperature where defects are mobile. As a result the observation could not be associated with the symmetry conformation of

point defects as described by Otsuka and Ren [49]. Further investigation is necessary to understand this behavior.

E. Summary and Conclusions

Creep tests and constant stress thermal cycling tests were conducted on a chosen HTSMA and the simultaneous viscoplastic and transformation behavior was studied. The experimental testing was followed by TEM characterizaton to understand the associated microstructural changes. From the constant stress thermal cycling tests it is observed that, depending on the rate of actuation, the simultaneous creep occurring during the transformation can significantly impact the actuators performance. The results from the thermomechanical tests on the $Ti_{50}Pd_{40}Ni_{10}$ alloy also indicate that, although the viscoplastic and the transformation induced plastic strain evolve simultaneously with transformation, the two irrecoverable strain generation mechanisms occur independently and do not affect each other. The creep of the alloy causes random distribution of defects, causing multiple nucleation sites to form compound twins. Contrary to this, the transformation induced plastic behavior results in stress localizations due to pinning and pileup of dislocations that leads to the formation of retained martensite, which does not participate in subsequent transformation cycles.

CHAPTER IV

TRANSFORMATION BEHAVIOR AND ACTUATION CHARACTERISTICS OF $TI_{50}PD_{40}NI_{10}$ HIGH TEMPERATURE SHAPE MEMORY ALLOY IN TENSION

This chapter studies the tensile transformation behavior and the actuation characteristics of a $Ti_{50}Pd_{40}Ni_{10}$ high temperature shape memory alloy. The alloy ingot is fabricated by vacuum arc melting, casting and subsequent hot rolling at 900°C, with a 30% reduction in thickness. From the bar, rectangular cross section (3 mm x 1 mm) tensile specimens are cut for thermomechanical testing in a custom high temperature test setup described in Chapter II. The work, or actuation characteristics, of the material is studied by conducting constant stress thermal cycling at different applied stress levels. The effects of an applied pre-strain (to assist with the martensitic re-orientation) on the actuation behavior is also investigated. In all the constant stress thermal cycling test results, a unique two stage expansion is observed during the first thermal cycle (i.e. specimen expanded during heating and cooling) in all the case. In the subsequent cycles, the material contracts upon heating and expands upon cooling as typically expected from tensile material behavior. Based on the observed unique thermomechanical behavior, an associated microstructural mechanism causing the transformation is hypothesized and optical microscopy and X-Ray Diffraction (XRD) is performed at different stages of the loading path to verify and support the hypothesis.

A. Material Fabrication and Thermomechanical Testing

The experimental setup used in the current chapter is the same as described in Chapters II and III the only difference being that instead of the compression grips, tensile

grips made out of Inconel are used. The grips consist of pin holes used to align the specimen and an additional grip section is used to apply force on the specimen using steel screws. The steel screws are replaced after each test to avoid the material from softening during subsequent tests, which could transfer all the force to the pins. A schematic of the tensile grip is shown in Fig. 37. Over the stress levels investigated in this work, the failure in all the specimen occurred within the gauge section and no deformation of the pin holes was observed. Due to this reason, the strain in the gauge length of the tensile specimen was calculated by subtracting the displacement due to the thermal expansion of the grip region within the extensometer from the total displacement measured and then normalizing it by the specimen gauge length. As described earlier, the specimen temperature was measured by a thermocouple fastened onto the specimen surface and a feedback controller was used to control the specimen temperature. A schematic of the test setup assembly is shown in Fig. 38.

The $Ti_{50}Pd_{40}Ni_{10}$ tensile specimens were machined from the same hot rolled bar as described in Chapter III. The transformation temperatures for the rolled bar, M_f, M_s, A_s and A_f, (measured by the tangent intersection method from the DSC data) are 360°C, 388°C, 392°C and 411°C respectively. Specimens with a 8 mm x 3 mm x 1 mm gauge length were machined by EDM. The specimens were machined along the rolling and the transverse directions and a picture of the machined specimen is shown in Fig. 39.

Uniaxial tensile loading was conducted on the tensile specimens at room temperature (martensitic state) and at 450°C (30°C above A_f, in austenitic state). For each test, the specimens were loaded at a constant strain rate of 10^{-4} sec^{-1} under isothermal conditions up to failure or a strain of 15% to avoid exceeding the limit of the extensometer. The stress-strain response was then used to choose the stress levels for studying the cyclic actuation behavior. A thermal cycle was also conducted

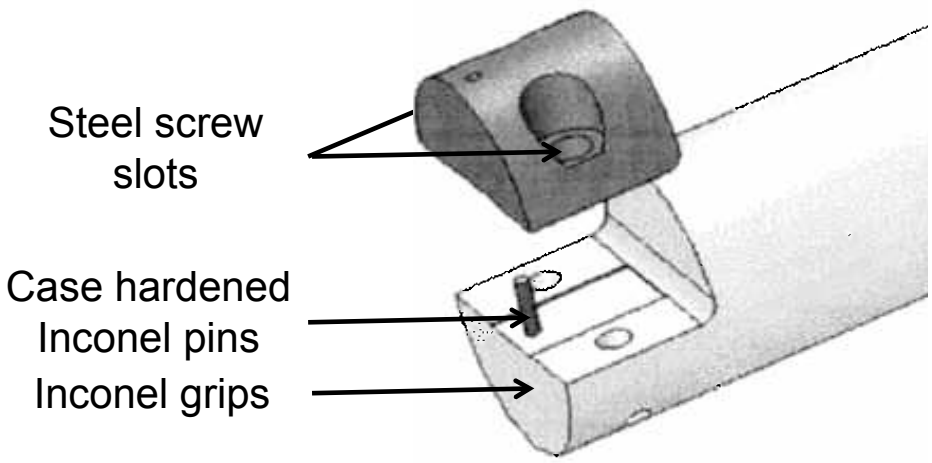

Fig. 37. A schematic of the tensile Inconel grip.

under an applied stress of 10 MPa to study the preliminary transformation behavior of the as-processed material. The strain-temperature response of the material was recorded.

The actuation behavior of the HTSMA was characterized by conducting thermally induced transformation cycles at different constant applied stress levels. For this study, the specimen was initially held at 10 MPa and at a temperature below M_f. The specimen was isothermally loaded to the desired applied stress level at a constant strain rate of 1 x 10^{-4} sec^{-1}. The specimen was then held at this stress level and thermally cycled through a complete transformation.

A Preliminary thermal cycling test conducted on a tensile specimen at a stress of 250 MPa showed that upon heating the specimen from 350°C, at a heating rate of 10°C/min, the specimen rapidly creeps and fails in 4 minutes (Fig. 40). The associated stress-strain behavior and the strain-time evolution of the creep strain is shown in Fig. 40a and Fig. 40b, respectively.

To avoid any viscoplastic strain contribution [51] and failure of the specimen,

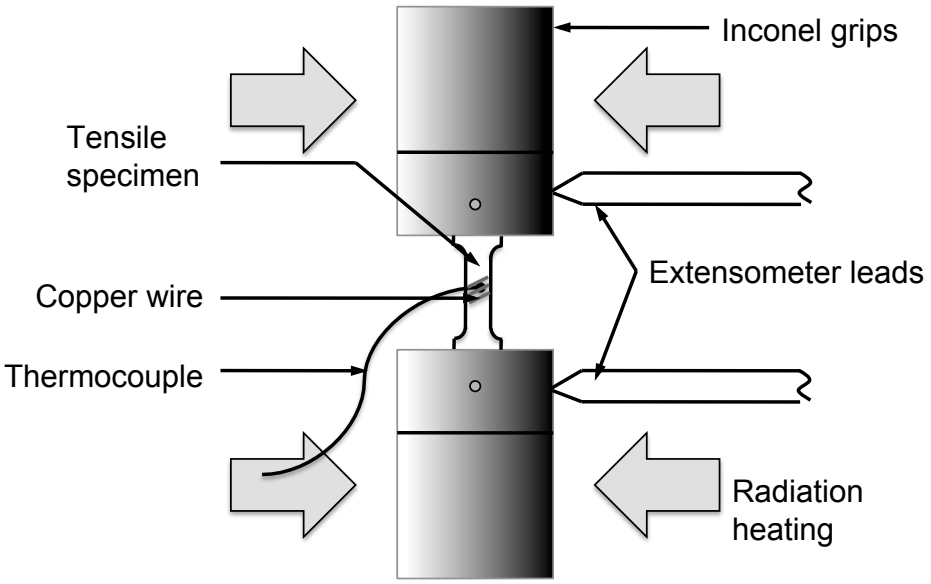

Fig. 38. A schematic of the tensile test setup on the uniaxial test frame.

a heating/cooling rate of 50°C/min was chosen for the thermal cycling tests. The heating or cooling was reversed after the strain evolution stabilized. After performing ten consecutive thermal cycles, the specimen was isothermally unloaded to 10 MPa. Holding the stress constant, the specimen was thermally cycled to recover any residual martensite and to also observe any induced TWSME. The loading path described above is shown in the phase diagram (Fig. 41) as the path $A-(C-D-C)_{10}-(E-F-E)_4$. The subscripts to $(C-D-C)$ and $(E-F-E)$ represent the number of cycles performed along that path. A 3-D representation of this loading path was shown earlier in Chapter II in Fig. 7. A specimen cut along the rolling direction was also tested along this loading path for comparison. The actuation strain and the irrecoverable strain values under different applied stress levels were plot for each cycle.

The effect of pre-strain (to re-orient the martensite) on the actuation behavior was also studied. For this purpose a specimen was held at a temperature below M_f at

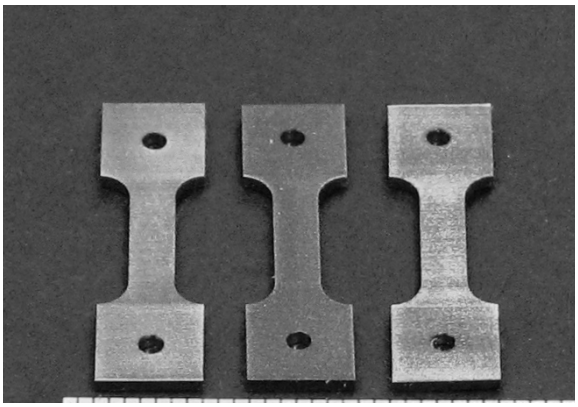

Fig. 39. A picture showing the tensile specimens machined by EDM from the hot rolled $Ti_{50}Pd_{40}Ni_{10}$ bar.

a constant stress of 10 MPa. The specimen was isothermally loaded to a desired pre-strain level and the material was subsequently unloaded to the desired actuation stress level. Under a constant stress, the specimen was thermally cycled through complete transformation at a rate of 50°C/min for 10 thermal cycles. The specimen was subsequently unloaded to 10 MPa and was thermally cycled through the transformation temperatures under a constant stress to recover any residual martensite in the material and to observed any induced TWSME. The loading path for the pre-straining case is depicted in the phase diagram as the path $A-B-(C-D-C)_{10}-(E-F-E)_4$. A 3-D representation of this loading path was shown earlier in Chapter II in Fig. 9. The actuation and the irrecoverable strains from the pre-strain case were compared with the strains from isobaric thermal cycling results. A consolidated thermomechanical test matrix is shown in Table IX.

B. Results from the Thermomechanical Testing

The stress-strain behavior for the uniaxial response in martensite and austenite is shown in Fig. 42. The stress σ is the uniaxial force on the specimen applied over the

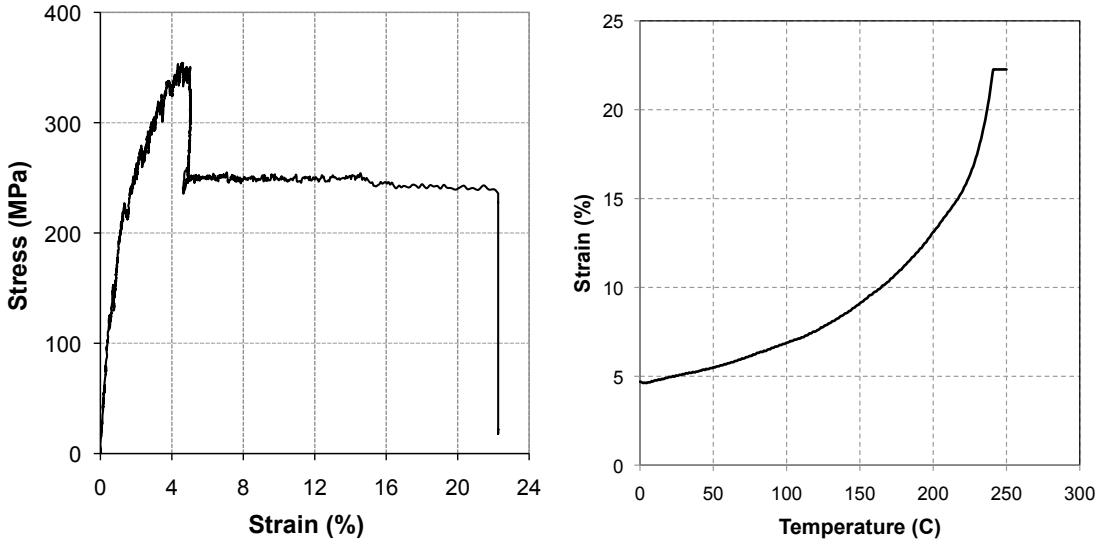

(a) (b)

Fig. 40. Results from the thermal cycling at 250 MPa constant stress; **(a)** Stress-strain diagram showing the creep until failure under a constant stress of 250 MPa; **(b)** strain-time behavior of the specimen upon heating the specimen from 350°C at 10°C/min under a constant stress of 250 MPa.

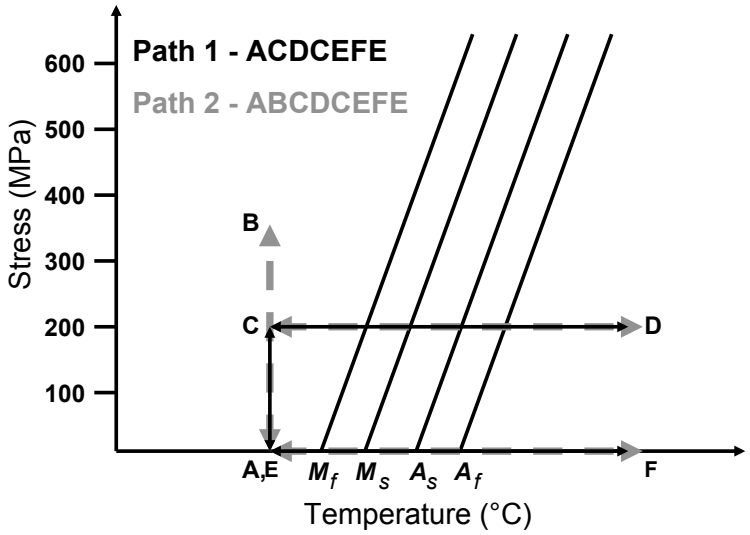

Fig. 41. Schematic of the phase diagram indicating the two loading paths for investigating the effect of applied stress and pre-strain on the actuation characteristics of the HTSMA.

cross sectional area of the SMA. The strain ε represents the change in the length of the specimen along the direction of the applied load normalized by the original length. For the test performed in the martensitic state, no distinct detwinning start or end region is observed before the failure of the specimen. From the behavior of austenite (at 450°C), no distinct pseudoelastic behavior is observed and the loading results in permanent yielding of the material. The tangent modulus for the martensitic and austenitic phases, determined from the loading slope of martensite and the unloading slope of austenite, are $E_m \simeq 57$ GPa and $E_a \simeq 32$ GPa respectively. From the test results, it is also noted that the yield stress for austenite is lower than martensite.

The strain-temperature response of the as-processed specimen, thermally cycled at 10 MPa, is shown in Fig. 43. The result indicates a fully recoverable transformation strain of $\simeq$1.5%. The transformation in the tensile specimen is characterized by an expansion upon heating and contraction upon cooling, similar to the transformation behavior under compression loading. The lack of a smooth transformation may be

Table IX. Test matrix for parametric study on the effect of total applied stress and applied strain on the transformation behavior.

Test #	Pre-strain	Applied stress	# of thermal cycles	Cut direction
1	-	100 MPa	10	Transverse
	-	10 MPa	4	
2	-	150 MPa	10	Transverse
	-	10 MPa	4	
3	-	200 MPa	10	Transverse
	-	10 MPa	4	
4	-	150 MPa	10	Rolling
	-	10 MPa	4	
5	5.0%	150 MPa	10	Transverse
	-	10 MPa	4	

associated with thermal fluctuations in the specimen due to the high heating/cooling rate. As a consequence, the strain and the temperature exhibit a higher standard deviation over the course of transformation. The nature of the transformation suggests the presence of compression favored martensitic variants that remain unbiased by the 10 MPa applied tensile stress.

The transformation behavior and the actuation characteristics of the alloy, were studied by isobaric thermal cycling tests. Since the trend in the material behavior was similar for all the test cases, the isobaric thermal cycling at 150 MPa will be described in detail. The stress-strain behavior for the test case is shown in Fig. 44. In this loading case, the specimen was initially maintained at a constant temperature of 260°C in the martensitic state (point A). The specimen was then isothermally loaded to a stress level of 150MPa (point C_1 in Fig. 44). At this constant stress the specimen

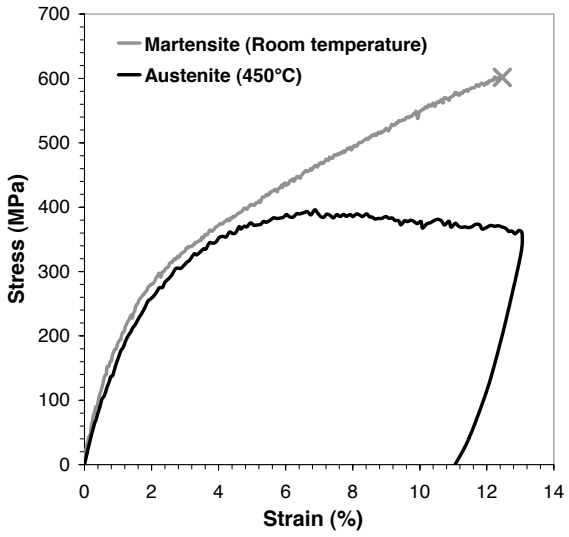

Fig. 42. Uniaxial stress-strain response of $Ti_{50}Pd_{40}Ni_{10}$ alloy (M_f=360°C, A_f=411°C) in the martensitic and austenitic state.

was thermally cycled from 260°C to 510°C at 50°C/min. The evolution of strain with the change in temperature is shown in Fig. 45a. During the first heating cycle the specimen gauge length expanded by 3% (point D_1). Upon cooling, the specimen expanded by an additional 4% (point C_2) resulting in a total expansion in the specimen gauge length by 7% during the first thermal cycle. In the subsequent nine thermal cycles, the specimen contracted upon heating and expanded upon cooling. At the end of twelve consecutive thermal cycles (point C_{13}), the specimen, at 260°C, was unloaded to 10 MPa stress (point E_1). The specimen was then subjected to thermal cycling at 10MPa to recover any residual martensite and to observe any TWSME. The strain-temperature diagram for the thermal cycling is shown in Fig. 45b. During the first cycle at 10MPa, upon heating to 510°C, the specimen contracted by 5% of its original length (point F_1). Cooling to 260°C, resulted in a further contraction by 4% (point E_2). Subsequent thermal cycles caused an expansion upon heating and contraction upon cooling, similar to the initially observed transformation behavior.

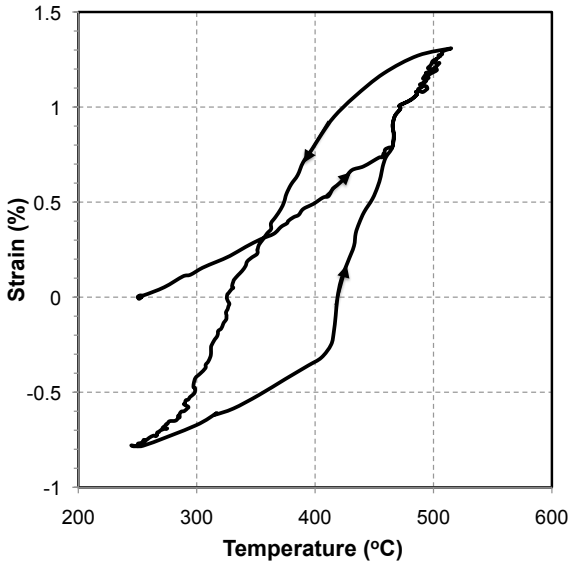

Fig. 43. Transformation behavior observed during the thermal cycle in the as-processed tensile specimens.

However the associated transformation strain at 10 MPa in the specimen was 4.5% compared to the 1.5% initially observed in the as-processed specimen. This concluded the loading path for the isobaric thermal cycling at a stress of 150 MPa. Similar tests were conducted for all the other test stress levels, the specimen cut along the rolling direction (at 150 MPa) and the pre-strained specimen (at 150 MPa). The results for those tests (stress-strain and strain-temperature data are shown in Appendix E). From all the above tests, the actuation strain (i.e. the strain measured during the heating cycle) and the irrecoverable strain (i.e. the strain between the start or end of two consecutive thermal cycles) were recorded and plotted.

The actuation strain in each cycle, for all the isobaric thermal cycling cases (with and without the pre-strain), is shown in Fig. 47a. During the first thermal cycle under constant stress, the specimen expands upon heating and cooling along the direction of applied load. Due to the unidirectional nature of the strain generated in the first thermal cycle, the actuation strain for the first cycle is taken as the sum

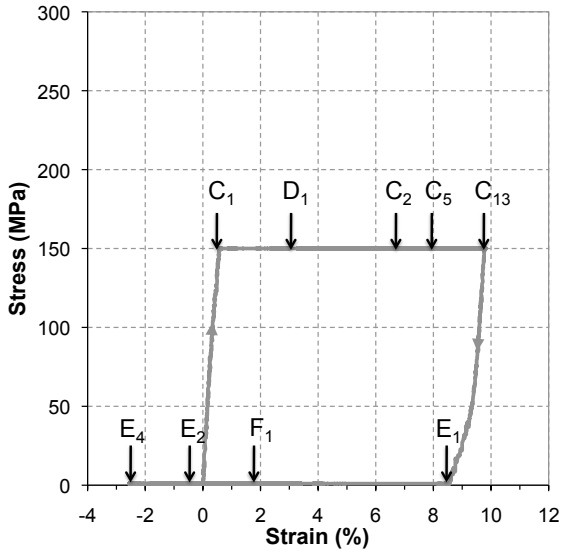

Fig. 44. Stress-strain diagram for the thermal cycling under a constant stress of 150 MPa and subsequent thermal cycling under 10 MPa.

of the strains generated during the heating and the cooling stage. As a result, the actuation during the first thermal cycle is higher than all subsequent cycles. In the next 9 cycles, the material contracts upon heating and expands upon cooling with a consistent 4-5% actuation strain. The specimens cycled at 100 and 150 MPa went through 10 consecutive cycles. However, the specimen tested at 200 MPa and the specimen cut along the rolling direction failed during the sixth and seventh cycle, respectively (see the test results shown in Appendix E). The irrecoverable strains generated during each thermal cycle for the different cases was also compared. The irrecoverable strain evolution for the different cases is shown in Fig. 47b. Based on the manner in which the irrecoverable strain is defined, the strain value in the first cycle is high compared to all subsequent cycles. It is noted from Fig. 47b that all specimens exhibit irrecoverable strains below 1% in each cycle except the specimen tested at 200 MPa and the specimen cut along the rolling direction. This higher permanent strain accumulation in each cycle could have caused the early failure in the specimen cut

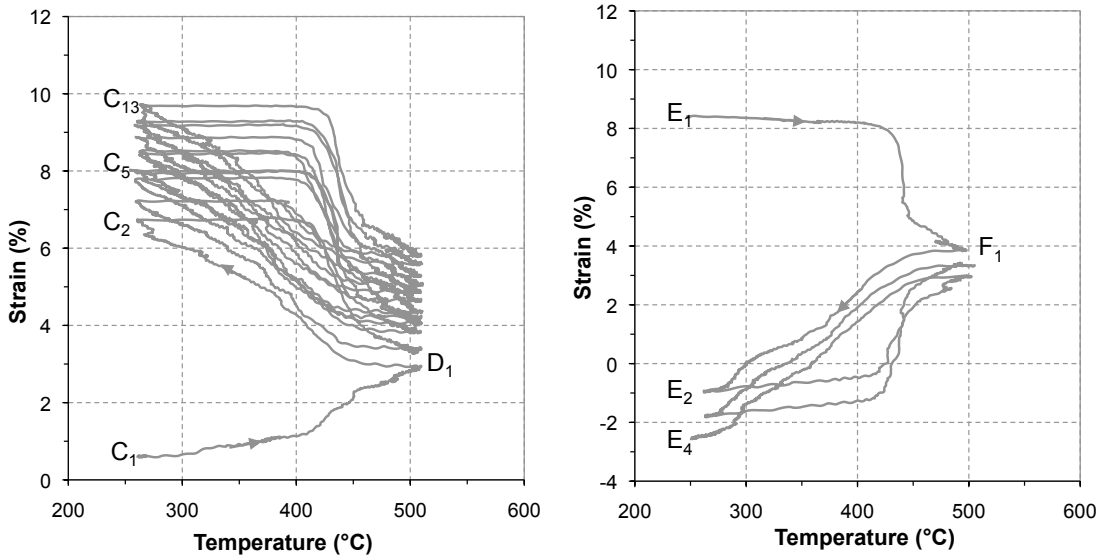

(a) (b)

Fig. 45. Strain-temperature diagram for the thermal cycling **(a)** at 150 MPa. **(b)** at 10 MPa.

along the rolling direction and the specimen tested at 200 MPa (see appendix E). For the specimen cut along the rolling direction, the relatively high irrecoverable strain in each cycle could be associated with the unfavorably oriented martensitic variants. Dislocations that accumulate with each subsequent transformation eventually lead to failure of the SMA. Optical microscopy on the specimen cut along the rolling direction revealed the presence of several micro cracks (see Fig. 46) on the specimen surface, some of which grew or coalesced to cause failure.

For the specimen thermally cycled at 200 MPa, a similar accumulation of irrecoverable strain is observed. This is due to the material's low critical stress for slip in the austenitic state. In the cases of the pre-strained specimen, no difference was observed in the actuation and irrecoverable strains generated in each cycle. This shows that pre-straining does not significantly impact the martensitic re-orientation

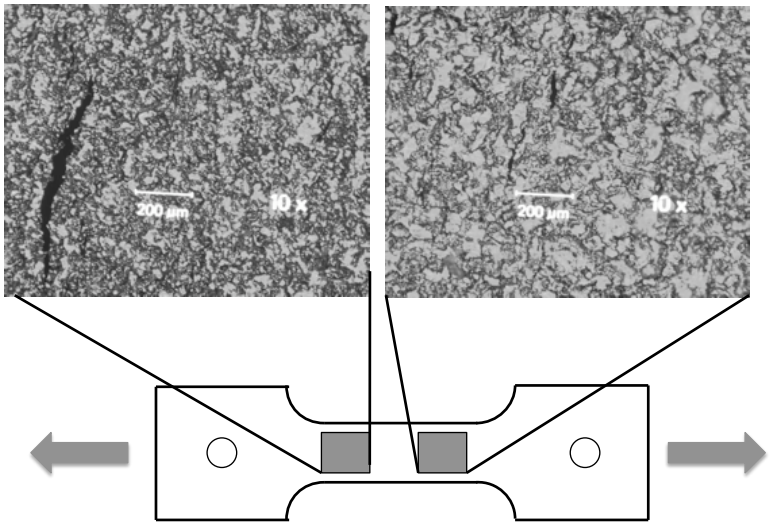

Fig. 46. Micro cracks observed on the surface of the failed specimen, which was cut along the rolling direction and thermally cycled at a constant applied stress of 150 MPa.

in this material.

A second observation is for the 100 and 150 MPa cases where the irrecoverable strain does not reduce but remains constant over the 10 cycles of testing. Typically in SMAs, repeated thermal cycling under a constant applied stress results in saturation of the irrecoverable strain generation, a process more commonly known as training. In the present $Ti_{50}Pd_{40}Ni_{10}$ HTSMA, thermal cycling does not show a decrease in the irrecoverable strain generation. Instead the irrecoverable strain remains constant over the 10 thermal cycles. From the previous, chapter it has already been shown that at the high temperature of operation, microstructural effects such as dislocation annihilation and creep due to climb become factors that affect the material behavior. In the present test results, the constant irrecoverable strain generated in each subsequent cycle suggests that annihilation of dislocations occurs at these high temperatures leading to an inability to train the alloy.

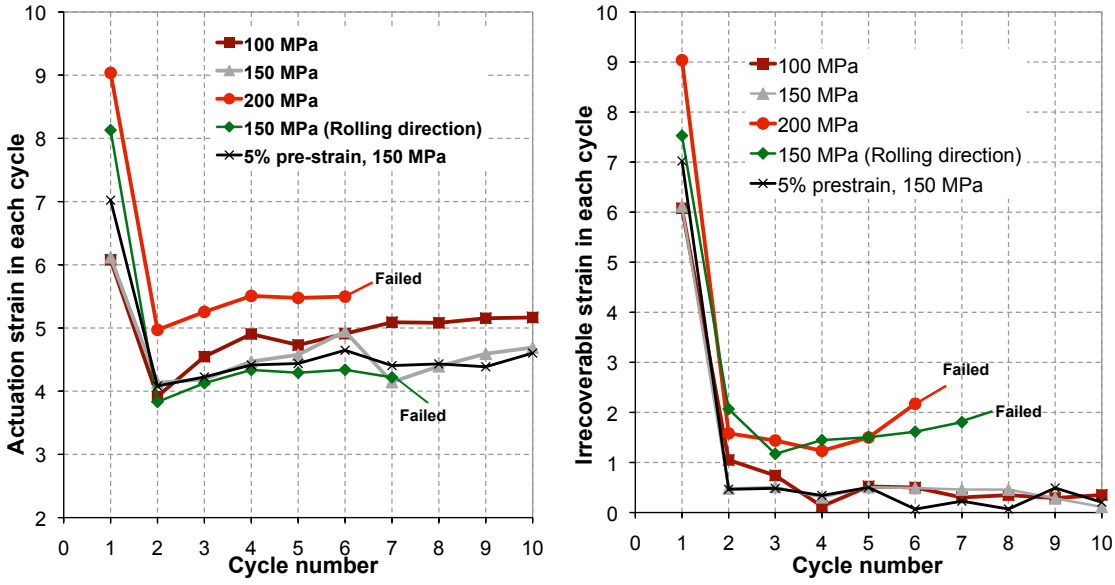

(a) (b)

Fig. 47. Transformation and irrecoverable strain evolution with thermal cycling under the loading path 1. **(a)** Transformation strain observed in each cycle for different initial applied stress levels. **(b)** Irrecoverable strain observed in each cycle for different initial applied stress levels.

C. Microstructural Characterization and Results

Two observations were made during the thermomechanical tests. The first is that the thermal cycling conducted at 10 MPa stress shows a transformation behavior which is characterized by an expansion upon heating and contraction upon cooling. This is contrary to what is typically observed in a tensile SMA specimen. A similar transformation behavior has been observed in cold rolled Ni-rich TiNi and TiNiFe alloys along specific orientations [52]. However, the behavior was attributed to the stress fields of Ni_4Ti_3 precipitates that biased the formation of specific R-phase variants.

The second observation is that during the actuation study at different stress levels a unidirectional transformation is observed during the first thermal cycle (i.e. expansion during heating and cooling) in the presence of an applied stress. Such a unidirectional transformation behavior has also been observed in CoNi single crystals under stress [53, 54]. The behavior in CoNi was associated with the multiple possibilities for the reverse transformation to occur between the Face Centered Cubic $< FCC >$ parent phase and Hexagonal Close Packed $< HCP >$ martensite phase. As a result, the transformation proceeded along the direction of the applied stress. However, the transformation in CoNi crystals was irrecoverable and the behavior ceased after a few thermal cycles [54]. In the current TiPdNi alloy, following the strain generation due to expansion at a higher stress level, the specimen undergoes a two stage contraction during the first thermal cycle at 10 MPa, resulting in a shape recovery.

To address the observed expansion upon heating, contraction upon cooling behavior in the as-received specimen and the cause for the unique two stage transformation observed in the first isobaric thermal cycle under stress and in the absence of stress, microprobe, optical microscopy and X-Ray Diffraction (XRD) studies were

conducted on the specimen. For the microprobe analysis, a specimen sample was embedded in an epoxy matrix and polished to a 3 micron surface finish. The specimen was then carbon coated to achieve a conductive surface. The composition of the matrix and the precipitate was determined at different regions. Precipitates 1 - 2μm in size were observed and these precipitates were identified as $Ti_2(Pd, Ni)$ with small quantities of oxygen, using microprobe analysis. A Back Scattered Electron (BSE) image of the alloy with the precipitates distributed in the matrix and the composition measurements in specific regions is shown in Fig. 48. Such precipitates have been commonly observed in previous studies on TiPdNi HTSMAs and, from their size and nature (i.e. oxide stabilized), it is known that the precipitates are not coherent and, as a result, there are no internal stresses caused by their presence which could bias certain martensitic variants in the material. Since no other thermomechanical treatments was conducted and no other precipitates were observed in the alloy, it can be concluded that the nature of the transformation (i.e. expansion upon heating, contraction upon cooling) is a result of compression favored martensitic variants biased by the defects induced during the thermomechanical processing.

To study the microstructural changes associated with the unique two stage expansion observed during the first thermal cycle under stress, the specimen microstructure was studied using a combination of mechanical polishing and thermomechanical testing. This technique was preferred because etching TiPdNi samples with a relatively high Palladium content consumes a long time period and results in chemical scarring which leads to unclear macrostructural features. To overcome this issue, a simpler solution was adopted which involved mechanically polishing the specimen to a 3 micro surface finish followed by performing a preliminary thermal cycle at a constant stress of 10 MPa. This preliminary cycle causes some of the martensite variants to deform out of plane which makes it easier to observe the preliminary material microstructure

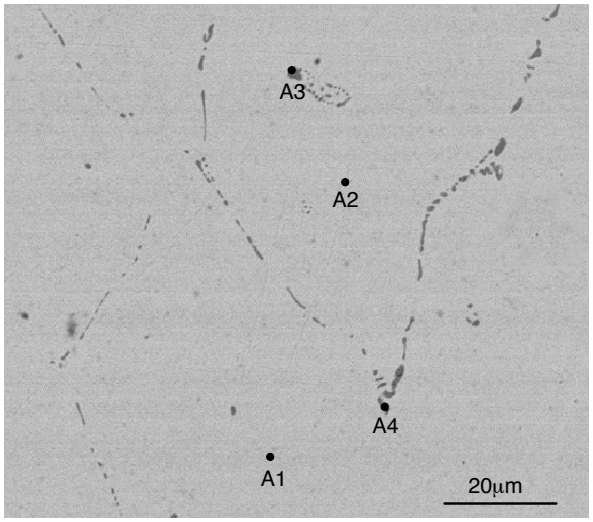

Position	Ti(at.%)	Pd(at.%)	Ni(at.%)
Matrix(A1)	45.97	43.05	10.92
Matrix(A2)	45.84	42.88	11.13
Precipitate(A3)	61.08	24.21	14.63
Precipitate(A4)	63.28	19.01	17.59

Fig. 48. BSE image showing the distribution of $Ti_2(Pd, Ni)$ oxide stabilized precipitates in the matrix.

using optical microscopy. The specimen was then tested along a similar loading path as shown in Fig. 45a and optical microscopy and XRD were conducted at stages A, E_1 and E_2. The optical micrographs and the indexed XRD patterns at the different stages are shown in Fig. 49 (Additional micrographs of the as-received specimen are shown in Appendix C) and Fig. 50, respectively. The XRD patterns were indexed to a B19 martensitic structure with lattice parameters a=2.78Å, b=4.53Å and c=4.78Å.

Based on the nature of the as-received transformation behavior (at 10 MPa) and transformation during the first cycle under stress (at 100, 150 or 200 MPa), the following hypothesis explaining the mechanism is presented. The nature of the transformation (at 10 MPa) in the specimen suggests the presence of compression favored martensitic variants. The associated XRD pattern for this state is shown in

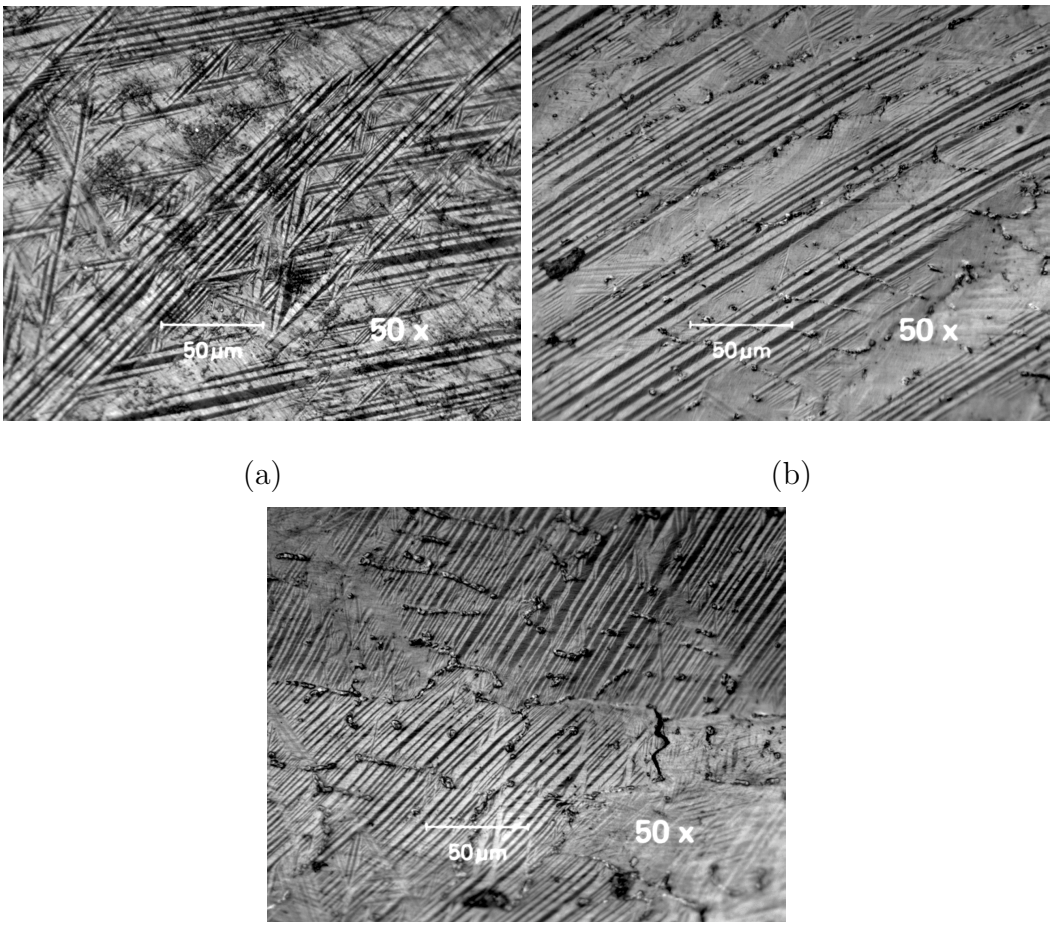

(a) (b)

(c)

Fig. 49. Microstructure of the specimen at various stages through the loading path. **(a)** Microstructure of the as-processed specimen before testing (point A) showing regions of self accommodated variants in a triangular morphology; **(b)** Microstructure of specimen after unloading from a loading path (point E_1) showing predominantly re-oriented martensitic variants; **(c)** Microstructure of the specimen after unloading, heating above A_f and cooling (point E_2). The microstructure continues to show the presence of predominantly re-oriented martensitic variants.

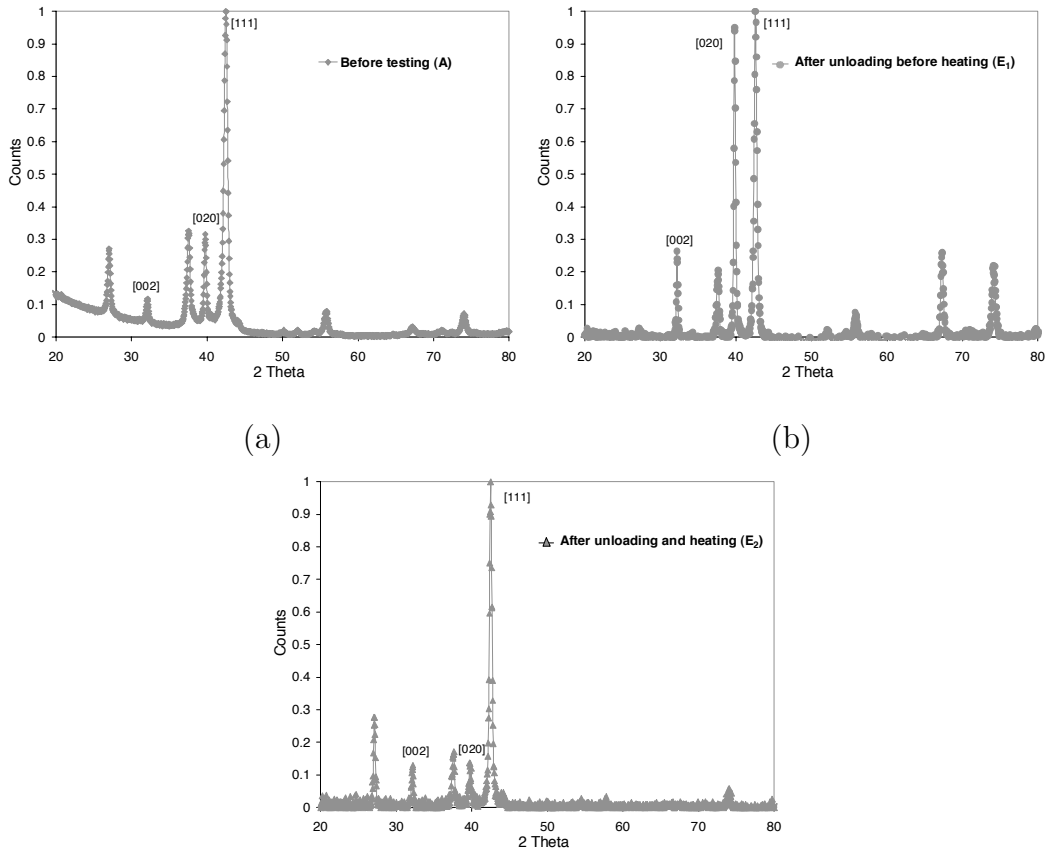

Fig. 50. XRD patterns of the specimen at various stages during the loading path in the martensitic state. **(a)** XRD pattern of the as-processed specimen before testing(point A); **(b)** XRD pattern of specimen after unloading (point E_1); **(c)** XRD pattern of specimen after unloading and heating above A_f (point E_2).

Fig. 50a. Upon heating the SMA under a constant stress of 150MPa, these compression favored martensitic variants transform to austenite by expansion. However, upon cooling, the presence of a tensile bias stress favors the formation of tension favored martensitic variants resulting in a further expansion. This hypothesis is supported by the change in the relative intensities of the [020] and the [111] peaks before and after one thermal cycle at 150MPa, indicating a change in the texture of the preferred martensitic variants formed (Fig. 50b, measured at point E_1). Due to the presence of the tensile bias stress, the transformation in subsequent cycles occurs between the tensile favored variants and austenite. Following the thermal cycles under stress, the sample is elastically unloaded in the martensitic state to 10 MPa. At this stage, the sample has the variants that were formed under a tensile bias stress. Upon heating to $T > A_f$, under a constant 10MPa, the tensile variants revert to austenite causing a contraction. When cooled, the austenite forms compression favored variants, as in the original as-processed material. This transformation causes an additional contraction and subsequent thermal cycling results in a similar transformation behavior to that observed in the as-received material. The hypothesized change back to compression favored variants is supported by the change in the [020] and [111] intensities again after heating and cooling at 10MPa (Fig. 50c, point E_2). The XRD pattern at the point E_2 very closely resembles the pattern observed at A which shows that the material has returned to a similar textured state. It is also observed from the tests that even after performing multiple thermal cycles under a tensile stress, the material reverts to the as-received transformation behavior upon completion. This suggests that the internal stresses in the microstructure that bias the formation of specific variants in the as-processed specimen remain stable even after significant thermal cycling under a bias stress.

The TWSME also shows a significant increase after the thermal cycling when

compared to the as-received material behavior (Fig. 51). The increase in the TWSME may be associated with the formation of additional compression favored variants stabilized by the thermal cycling. This is supported by the optical micrographs which show predominantly detwinned variants after cycling (Fig. 49c) in contrast to the as-processed specimen that shows a mixture of detwinned and self accommodated variants (Fig. 49a).

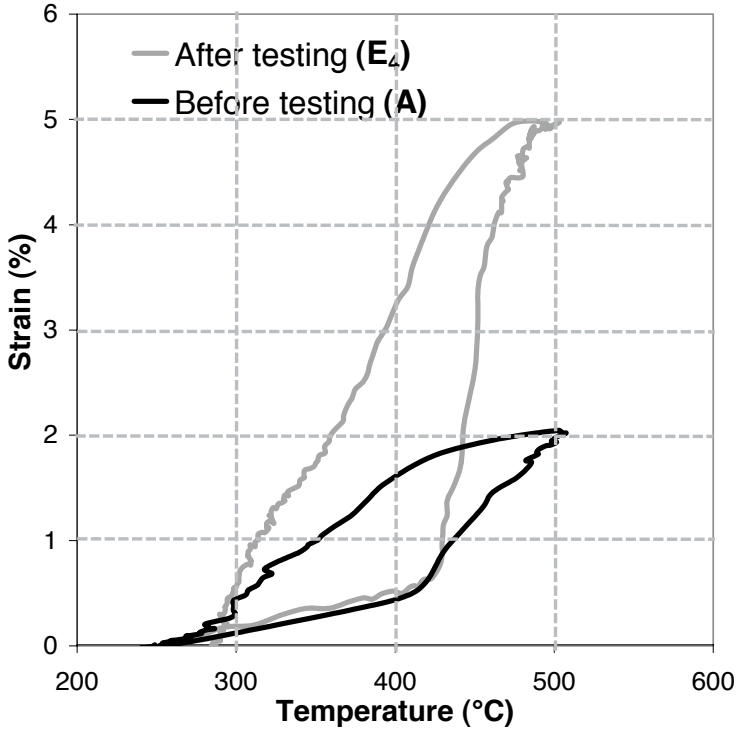

Fig. 51. The TWSME from the tensile specimen before and after the thermal cycling.

D. Summary and Conclusions

Thermomechanical studies were performed in tension to determine the actuation properties of a $Ti_{50}Pd_{40}Ni_{10}$ HTSMA. The studies revealed an unique unidirectional transformation behavior, that was observed during the first thermal cycle under a

tensile applied stress between the range of 100 and 200 MPa, and this unidirectional transformation was recoverable following a thermal cycle under a relatively, lower stress of 10 MPa. Microstructural studies were also conducted at different stages during thermomechanical loading to study the associated microstructural changes. Analyzing the thermomechanical and microstructure of the material, it is concluded that the unique transformation behavior observed in the alloy during the first actuation cycle is a consequence of the material behavior induced due to processing. The as-processed or as-received tensile material behavior indicates a unique TWSME characterized by expansion upon heating and contraction upon cooling. Microstructural studies indicate this behavior to be induced due to dislocation stress fields that bias certain compression favored martensitic variants over the others when hot rolled at 900°C. When a specimen exhibiting this TWSME is actuated under an applied tensile stress, the compression favored variants transform to austenite causing an expansion. When cooled, the presence of the tensile bias stress causes the austenite to form tensile favored martensitic variants which, in turn, results in a second stage of expansion. As a result, the first actuation cycle under an applied tensile stress exhibits a large actuation strain. Such a large actuation strain can be used for a wide variety of actuator applications. Upon unloading and heating, the alloy reverts from the tensile favored variants to austenite by contraction and cooling results in the formation of compression favored variants again resulting in additional contraction. Thus, a significant portion of the the large transformation strains generated under a relatively high applied tensile stress of 100 MPa is recoverable under small stress conditions (10 MPa in this case). A total actuation strain of approximately 7% is a significant improvement in the performance of high temperature actuation behavior. In addition, the material is also capable of resetting the shape in the stress free state. The material in subsequent cycles generates a consistent 3.5-4.5% actuation strain

due to the SME behavior for stress levels between 100 and 150 MPa. For stress levels exceeding the critical stress for slip (200 MPa), the material generated relatively high irrecoverable strain which accumulated and led to failure.

From the diffraction and microscopy studies it was concluded that the unique unidirectional transformation behavior is a result of compression favored martensitic variants (causing a unique transformation in the as-received material) transforming to austenite (by expansion) followed by the austenite, upon cooling, transforming back to tension favored martensitic variants due to the applied bias stress (by expansion again). This leads to the two stage expansion observed during the first thermal cycle under stress. In the absence of stress, after unloading, a two stage reverse transformation occurs from the tension favored variants to austenite and then to the compression favored martensitic variants which appears as strain recovery.

CHAPTER V

CONCLUSIONS

The plasticity occurring simultaneously during detwinning and/or during thermally induced transformation was studied for a $Ti_{50}Pd_{30}Ni_{20}$ HTSMA under a constant stress thermal cycling load path with and without a pre-strain. Analyzing the test results the following conclusions are drawn.

- The detwinning (pre-strain) accompanied by plasticity leads to the generation of internal stresses in the alloy which increases the transformation temperatures and as a consequence shifts the forward and reverse phase transformation surfaces.

- This shift in the transformation surface necessitates heating to a higher temperature during the second cycle to complete the actuation.

- The increased transformation temperatures were mapped with an equivalent stress (which corresponds to an internal stress) using the as-received material phase diagram. A trend for the equivalent internal stress as a function of the applied stress and accumulated plastic strain was established. Such a function can be implemented into thermomechanical models to more accurately capture the behavior of HTSMAs during cyclic actuation.

- Finally although the pre-strain or detwinning causes a shift in the transformation surfaces which affects actuation behavior in subsequent cycles, a notable advantage is the ability to achieve higher transformation strains compared to constant stress thermal cycling tests actuated at the same stress level.

In $Ti_{50}Pd_{40}Ni_{10}$ HTSMA which has the transformation temperatures in the regime where creep occurs, simultaneous creep and transformation behavior of the HTSMA has been observed for the first time. Transformation induced plasticity (TRIP) and viscoplasticity mechanisms (during the course of a constant stress actuation thermal cycle) cause different changes (as mentioned below) to the microstructure which in turn affect the actuation behavior of the SMA.

- Viscoplatic strains generated in the HTSMA cause the formation of deformation twins or compound twins in the material since the climb mechanism facilitates multiple defect sites for nucleation. However the creep behavior did not impact the phase transformation behavior in the SMA.

- The rate independent irrecoverable strain generated in the HTSMA was in part associated with the formation of retained martensite in the microstructure which causes a decrease (for the present $Ti_{50}Pd_{40}Ni_{10}$ HTSMA, this decrease was approximately 20%) in the transformation strain of the HTSMA.

Finally the actuation characteristics of $Ti_{50}Pd_{40}Ni_{10}$ HTSMA was studied under tensile loading. The study revealed a two stage unidirectional transformation behavior (i.e. expansion or contraction during heating and during cooling) when thermally cycled under constant stress in tension.

- XRD and microstructural studies revealed that the two-stage unidirectional transformation under the applied tensile stress was associated with the transformation of compression favored martensitic variants (causing the TWSME in the as-received material) to austenite to tensile favored martensitic variants (formed due to the applied bias stress). In subsequent cycles the SMA only transformed between the tensile martensitic variants and austenite.

- Upon unloading, and thermal cycling at 10 MPa, the reverse transformation occurred with the tensile favored martensitic variants transforming to austenite and back to the compression favored martensitic variants.

- The nature of the transformation behavior (i.e. expansion during heating and cooling) can improve the actuation strain (in the present case by 100%) and consequently the work that can be generated by a HTSMA at these high operating temperatures.

A. Future Work

Although techniques are being developed to quantify the influence of plasticity on the transformation behavior and thermomechanical treatments and alloying techniques have been investigated in the past for TiPdNi alloys as a means to increase the critical stress for slip, a renewed focus is required to improve the material properties by adopting techniques such as alloying, grain refinement and thermomechanical processing to improve the critical stress for slip of the martensitic phase.

The present work has shown that creep that occurs during the course of transformation, depending on the heating/cooling rate, can significantly affect the actuation behavior of HTSMAs. However, these studies have been limited to one actuation cycle. For the continued performance of actuators over multiple cycles, it is necessary to study the impact of thermal cycling rate and the associated creep strain generated over multiple or repeated actuation cycles.

Newer Co based HTSMAs [55] have been developed that exhibit pseudoelastic behavior to temperatures as high as 200°C. In these newer HTSMAs, the influence of loading rate and the associated influence of the viscoplasticity on the pseudoelastic behavior must be investigated.

While such a characterization methodology helps in understanding the simultaneous creep and phase transformation behavior from a materials perspective, methods to reduce creep in such HTSMAs without sacrificing the actuation capability of the material must be developed. Techniques such as precipitation hardening, grain refinement, and alloying to increase the melting temperature which have been implemented to minimize creep in Ti-alloys, steels and Ni-super alloys can be carefully reviewed and suitable or custom modified methods can be adopted to try to minimize creep in HTSMAs.

REFERENCES

[1] S. Wu, C. Wayman, Martensitic transformations and the shape-memory effect in $Ti_{50}Ni_{10}Au_{40}$ and $Ti_{50}Au_{50}$ alloys, Metallography (1987) 359.

[2] P. Lindquist, C. M. Wayman, Shape memory and transformation behavior of martensitic Ti-Pd-Ni and Ti-Pt-Ni alloys, Engineering Aspects of Shape Memory Alloys, Butterworth-Heinemann, London, 1990.

[3] Z. Pu, H. Tseng, K. Wu, Martensite transformation and shape-memory effect of NiTi-Zr high- temperature shape-memory alloys, in: SPIE proceedings, Vol. 2441, 1995, p. 171.

[4] P. E. Thoma, J. J. Boehm, Effect of composition on the amount of second phase and transformation temperatures of $Ni_xTi_{90-x}Hf_{10}$ shape memory alloys, Materials science and engineering A (1999) 273–275.

[5] T. Biggs, M. B. Cortie, M. J. Witcomb, L. A. Cornish, Platinum alloys for shape memory applications, Platinum Metals Rev 47 (4) (2003) 142–156.

[6] H. C. Doonkersloot, V. Vucht, Martensitic transformations in Au-Ti, Pd-Ti and Pt-Ti alloys, Journal of Less Common Metals 20 (1970) 83–91.

[7] V. Khachin, V. Grunter, V. Sivokha, A. Savvinov, in: Proceedings of International Conference on Martensitic Transformation, Cambridge, MA, 1979, p. 474.

[8] V. Khachin, N. Matveeva, V. P. Sivokha, D. Chernov, High-temperature shape memory effects in TiNi-TiPd system alloys, Doklady Akademii Nauk SSSR 257 (1) (1981) 167 – 169.

[9] K. Enami, T. Hoshiya, in: Proceedings of Material Technology, Helsinki, Finland, 1990.

[10] K. Otsuka, K. Oda, Y. Ueno, M. Piao, The shape memory effect in a $Ti_{50}Pd_{50}$ alloy, Scripta Metallurgica et Materialia 29 (1993) 1355–1358.

[11] D. Golberg, Y. Xu, Y. Murakami, K. Otsuka, T. Ueki, H. Horikawa, High-temperature shape memory effect in $Ti_{50}Pd_{50-x}Ni_x(x = 10, 15, 20)$ alloys, Materials Letters 22 (1995) 241–248.

[12] D. Golberg, Y. Xu, Y. Murakami, S. Morito, K. Otsuka, T. Ueki, H. Horikawa, Characteristics of $Ti_{50}Pd_{30}Ni_{20}$ high-temperature shape memory alloy, Intermetallics 3 (1995) 35–46.

[13] Q. Tian, J. Wu, Tensile behavior of $Ti_{50.6}Pd_{30}Ni_{19.4}$ alloy under different tensile conditions, Materials Science and Engineering 325 (2002) 249–254.

[14] Q. Tian, J. Wu, Characterisation of phase transformation in $Ti_{50+x}Pd_{30}Ni_{20-x}$ alloys, Intermetallics 10 (2002) 675–682.

[15] D. Golberg, Y. Xu, Y. Murakami, S. Morito, K. Otsuka, T. Ueki, H. Horikawa, Improvement of a $Ti_{50}Pd_{30}Ni_{20}$ high-temperature shape memory alloy by thermomechanical treatment, Scripta Metallurgica et Materialia 30 (10) (1994) 1349–1354.

[16] Y. Suzuki, S. Ya Xu, S. Morito, K. Otsuka, K. Mitose, Effects of boron addition on microstructure and mechanical properties of Ti-Pd-Ni high-temperature shape memory alloys, Materials Letters 36 (1998) 85–94.

[17] T. Sawaguchi, M. Sato, A. Ishida, Microstructure and shape memory behavior of $Ti_{51.2}(Pd_{27.0}Ni_{21.8})$ and $Ti_{49.5}Pd_{28.5}Ni_{22.0}$ thin films, Materials Science and

Engineering 332 (2002) 47–55.

[18] S. Padula II, G. Bigelow, R. Noebe, D. Gaydosh, A. Garg, Challenges and progress in the development of high-temperature shape memory alloys based on NiTiX compositions for high-force actuator applications, in: Proceedings of the International Conference on Shape Memory and Superelastic Technologies, ASM International, Metals Park, OH, 2006.

[19] K. N. Melton, O. Mercier, Fatigue of NiTi thermoelastic martensites, Acta Metallurgica 27 (1979) 137–144.

[20] G. Eggeler, E. Hornbogen, A. Yawny, A. Heckmann, M. Wagner, Structural and functional fatigue of NiTi shape memory alloys, Materials Science and Engineering A (378) (2004) 24–33.

[21] J. L. McNichols, P. C. Brooks, NiTi fatigue behavior, Journal of Applied Physics 52 (1981) 7442–7444.

[22] H. Tobushi, T. Hachisuka, S. Yamada, P. H. Lin, Rotating-bending fatigue of a TiNi shape-memory alloy wire, Mechanics of Materials 26 (1997) 35–42.

[23] H. Tobushi, T. Hachisuka, T. Hashimoto, S. Yamada, Cyclic deformation and fatigue of a TiNi shape memory alloy wire subjected to rotating bending, Journal of Engineering Materials and Technology 120 (1998) 64–70.

[24] J. M. Young, K. J. Van Vliet, Predicting in vivo failure of pseudoelastic NiTi devices under low cycle, high amplitude fatigue, Journal of Biomedical Materials Research B (2005) 17–26.

[25] S. Miyazaki, Engineering aspect of shape memory alloys, Butterworth-Heinemann, London, 1990.

[26] S. Miyazaki, K. Mizukoshia, T. Uekib, T. Sakumac, Y. Liu, Fatigue life of Ti 50 at.% Niand Ti 40Ni 10Cu (at.%) shape memory alloy wires, Materials Science and Engineering A 273-275 (1999) 658–663.

[27] D. Miller, Thermomechanical characterization of plastic deformation and transformation fatigue in shape memory alloys, Ph.D. Dissertation, Texas A&M University (2000).

[28] D. A. Miller, D. C. Lagoudas, Influence of cold work and heat treatment on the shape memory effect and plastic strain development of NiTi, Material Science & Engineering A 308 (2001) 161–175.

[29] K. Gall, H. J. Maier, Cyclic deformation mechanisms in precipitated NiTi shape memory alloys, Acta Materialia 50 (2002) 4643–4657.

[30] O. W. Bertacchini, D. C. Lagoudas, Fatigue life characterization of shape memory alloys undergoing thermomechanical cyclic loading, in: Proceedings of SPIE, Vol. 5053, 2003, pp. 612–624.

[31] M. J. Bigeon, M. Morin, Thermomechanical study of the stress assisted two way memory effect fatigue in TiNi and CuZnAl wires, Scripta Materialia 35 (12) (1996) 1373–1378.

[32] S. Miyazaki, T. Imai, Y. Igo, K. Otsuka, Effect of cyclic deformation on the pseudoelasticity characteristics of Ti-Ni alloys, Metallurical Transactions A 17 (1986) 115–120.

[33] B. Strnadel, S. Ohashi, H. Ohtsuka, T. Ishihara, S. Miyazaki, Cyclic stress-strain characteristics of Ti-Ni and Ti-Ni-Cu shape memory alloys, Material Science & Engineering A 202 (1995) 148–156.

[34] A. K. Mukherjee, High-temperature-creep mechanism of TiNi, Journal of Applied Physics 39 (5) (1968) 2201–611.

[35] G. Eggeler, J. Khalil-Allafi, K. Neuking, A. Dlouhý, Creep of binary Ni-rich NiTi shape memory alloys and the influence of pre-creep on martensitic transformations, Zeitschrift für Metallkunde 93 (1993) 397–411.

[36] C. Lexcellent, P. Robinet, J. Bernardini, D. L. Beke, P. Olier, High temperature creep measurements in equiatomic Ni-Ti shape memory alloy, Materialwissenschaft und Werkstofftechnik 36 (10) (2005) 509–512.

[37] S. M. Oppenheimer, A. R. Yung, D. C. Dunand, Power-law creep in near-equiatomic nickel-titanium alloys, Scripta Materialia 57 (2007) 377–380.

[38] G. Eggeler, J. Khalil-Allafi, K. Neuking, A. Dlouhy, Creep of binary Ni-rich NiTi shape memory alloys and the influence of pre-creep on martensitic transformations, Zeitschrift fuer Metallkunde 93 (2002) 654–660.

[39] R. Noebe, S. Padula II, G. Bigelow, O. Rios, G. Anita, B. Lerch, Properties of a $Ni_{19.5}Pd_{30}Ti_{50.5}$ high-temperature shape memory alloy in tension and compression, in: Proceedings of SPIE, Vol. 6170, 2006, pp. 279–291.

[40] G. Bigelow, Effects of palladium content, quaternary alloying, and thermomechanical processing on the behavior of Ni-Ti-Pd shape memory alloys for actuator applications, Master's thesis, Colorado School of Mines (2006).

[41] W. Cai, K. Otsuka, M. Asai, Martensitic aging effects in Ti-Pd and Ti-Pd-Ni high temperature shape memory alloys, Materials Transactions, JIM 40 (9) (1999) 895–898.

[42] G. Ghosh, Nickel – Palladium – Titanium, Light Metal Ternary Systems: Phase Diagrams, Crystallographic and Thermodynamic Data, Landolt-Borntein New Series IV, Springer-Verlag, Berlin, 2006.

[43] P. Lindquist, Structure and transformation behavior of martensite Ti-(Ni, Pd) and Ti-(Ni, Pt) alloys, Ph.D. dissertation, University of Illinois at Urbana-Champaign (1988).

[44] R. Delville, D. Schryvers, Z. Zhang, R. D. James, Transmission electron microscopy investigation of microstructures in low-hysteresis alloys with special lattice parameters, Scripta Materialia 60 (2009) 293–296.

[45] E. E. Kobus, K. Neuking, G. Eggeler, I. Wittkamp, The creep behaviour of a NiTi-alloy and the effect of creep deformation on it's shape memory properties, Practical Metallography 39 (4) (2002) 177–186.

[46] G. E. Dieter (Ed.), Mechanical Metallurgy, 3rd Edition, McGraw-Hill Science Engineering, New York 1986.

[47] D. C. Lagoudas, G. Chatzigeorgiou, P. K. Kumar, Modeling and experimental study of simultaneous creep and transformation in polycrystalline high-temperature shape memory alloys, Journal of Intelligent Material Systems and Structures 20 (18) (2009) 2257–2267.

[48] M. Nishida, T. Hara, Y. Morizono, A. Ikeya, H. Kijima, A. Chiba, Transmission electron microscopy investigation of twins in martensite in Ti-Pd shape memory alloy, Acta Materialia 45 (11) (1997) 4847–4853.

[49] X. Ren, K. Otsuka, Universal symmetry property of point defects in crystals, Physical Review Letters 85 (5) (2000) 1016–1019.

[50] W. Cai, K. Otsuka, Martensitic aging effects in a Ti50Pd50 high temperature shape memory alloy, Scripta Materialia 41 (12) (1999) 1311–1317.

[51] D. C. Lagoudas, G. Chatzigeorgiou, P. K. Kumar, Modeling and experimental study of simultaneous creep and transformation in polycrystalline high temperature shape alloys, Journal of Intelligent Material Systems and Structures 20 (18) (2009) 2257–2267.

[52] J. J. Wang, T. Omori, Y. Sutou, R. Kainuma, K. Ishida, Two-way shape memory effect induced by cold-rolling in Ti-Ni and Ti-Ni-Fe alloys, Scripta Materialia 52 (2005) 311–316.

[53] Y. Liu, G. Tan, S. Miyazaki, Y. Liu, B. Jiang, Thermomechanical behavior of $FCC \leftrightarrow HCP$ martensitic transformation in coni, Journal of Physics IV 112 (2003) 1025–1028.

[54] Y. Liu, H. Yang, G. Tan, S. Miyazaki, B. Jiang, Y. Liu, Stress induced $FCC \leftrightarrow HCP$ martensitic transformation in coni, Journal of Alloys and Compounds 368 (2004) 157–163.

[55] H. E. Karaca, I. Karaman, Y. I. Chumlyakov, D. C. Lagoudas, X. Zhang, Compressive response of a single crystalline conial shape memory alloy, Scripta Materialia 51 (2004) 261–266.

APPENDIX A

CALCULATIONS AND STUDIES TO ACCOUNT FOR THERMAL EXPANSION AND HEAT TRANSFER DURING THERMOMECHANICAL TESTING

One of the primary concerns while conducting thermomechanical tests is to accurately measure the strain on the specimen. Additionally, if the setup is enclosed in a furnace, the effects of thermal expansion need to be subtracted. A schematic of the current test setup assembly with the extensometer leads, grips and the specimen is shown in Fig. 52. From the schematic, it is noticed that the extensometer leads rest on the grips surface when assembled, due to the large gauge length of the extensometer. As a result during a typical actuation cycle (i.e. constant stress thermal cycling) this total strain (ε_{tot}) includes the strain due to transformation (ε_t), thermal expansion of the specimen (α_s) and the grips (α_g) as well as the elastic strain due to the applied stress (σ). The elastic strain due to the grips is not taken into consideration because the grips are significantly larger in diameter than the specimen and as a result can be ignored. In order to obtain the transformation strain due to the HTSMA, it is necessary to subtract the strains due to thermal expansion of the grips and the specimen and elastic strain (due to applied stress) from the recorded total strain. With the thermal expansion of the SMA (in the present case this is measured from an individual test) and the grips (we know the thermal expansion coefficient for 718 precipitation hardened Inconel) known and the knowledge of the grips lengths (measure after assembly as l1 and l2) and specimen length (known, l3) within the extensometer gauge length, the transformation strain (ε_t) due to SMA can be calculated using the equation A.1 below.

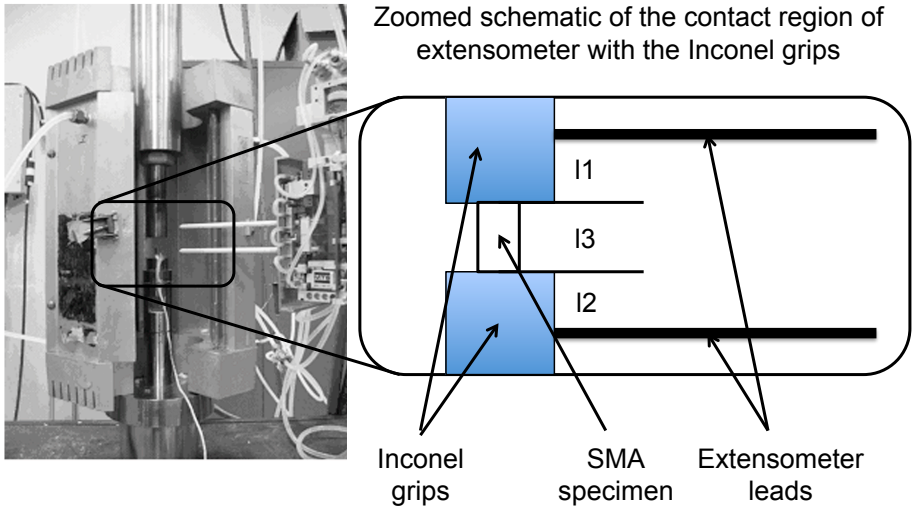

Fig. 52. A schematic showing the assembly of the extensometer onto the Inconel grips during thermomechanical testing.

$$\varepsilon_t = 1/l3(\varepsilon_{tot}(l1 + l2 + l3 - (l1\alpha_g\delta T + l2\alpha_g\delta T + l3\alpha_s\delta T + (l3\sigma/E_m)) \qquad \text{(A.1)}$$

where α_g and α_s are the thermal expansion coefficients of the grips and the SMA, respectively. δT is the temperature range through which the specimen is actuated. l1 and l2 represent the length of the top and the bottom grip respectively within the gauge length of the extensometer. E_m is the elastic modulus of the SMA when in the martensitic state (since the material is loaded when in martensite), and σ is the actuation stress level. In the case of a uniaxial isothermal loading, since thermal expansion is not an issue, the strain is directly calculated by dividing the recorded total strain by the scaling factor which is defined as the ratio of the extensometer gauge length to the specimen length.

The other issue during thermomechanical testing of a SMA is the heat transfer

during thermal cycling. Depending on the dimensions of the SMA, and the capability of the setup, it is necessary to determine what is the safest rate to heat and cool an SMA to capture the actual material behavior and the phase transformation temperature without any influence from heat transfer effects. Such effects can occur in the case of large specimens where the temperature is measured on the surface using a thermocouple. In such cases, during a high heating rate, the specimen temperature may not be uniform through the thickness (due to insufficient time to equilibrate) and as a result the specimen may have a higher outside temperature compared to the interior. In such a case, during a reverse transformation (from martensite to austenite) it may appear that the transformation is occurring at a temperature higher that the actual phase transformation temperature. In order to avoid this, for the present test setup, studies were conducted by heating/cooling a test specimen at 3 different rates of 2°C/min, 5°C/min and 10°C/min. The results from the tests showed that at thermal cycling rates of 2°C/min and 5°C/min no significant deviation in the transformation behavior/temperatures was observed (± 1°C). However a deviation of 2-3°C was observed for the 10°C/min heating/cooling rate. As a result for all the thermomechanical tests, the thermal cycling rate was limited to 5°C/min (except for the study of simultaneous creep and viscoplasticity).

APPENDIX B

DATA FROM THE PARAMETRIC STUDY TO STUDY THE WORK CHARACTERISTICS UNDER APPLIED STRAIN AND ACTUATION STRESS LEVELS FOR $TI_{50}PD_{30}NI_{20}$ HTSMA IN COMPRESSION

The test data from the parametric actuation study for the different applied strains of 3.5%, 4%, 4.5% and 5% followed by actuation at 100, 150 and 200 MPa is shown below. A typical test matrix for such a loading path is also listed in Table X.

Table X. A typical loading path for the parametric study of the action behavior of the $Ti_{50}Pd_{30}Ni_{20}$ HTSMA in compression. The case shown below is for a constant applied strain of 4% followed by Isobaric thermal cycling tests at 100, 150 and 200 MPa.

Test type	Applied stress/strain	Temperature	Loading rate
Uniaxial loading	4%	180°C	10^{-4}/sec
Thermal cycling	100 MPa	180-380°C	5°C/min
Thermal cycling	10 MPa	180-380°C	5°C/min
Uniaxial loading	4%	180°C	10^{-4}/sec
Thermal cycling	150 MPa	180-380°C	5°C/min
Thermal cycling	10 MPa	180-380°C	5°C/min
Uniaxial loading	4%	180°C	10^{-4}/sec
Thermal cycling	200 MPa	180-380°C	5°C/min
Thermal cycling	10 MPa	180-380°C	5°C/min

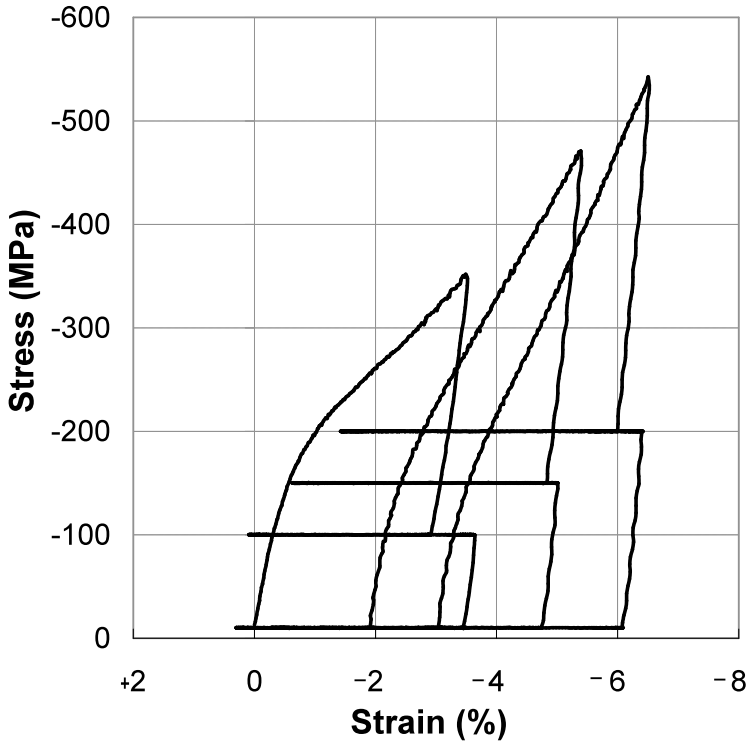

Fig. 53. Stress-strain diagram showing the detwinning by a 3.5% applied strain followed by unloading and actuation at 100 MPa. Following the actuation the specimen is unloaded to 10 MPa and one thermal cycle is conducted to recover any remnant detwinned martensite. The loading path is then repeated with subsequent actuation cycles at 150 and 200 MPa.

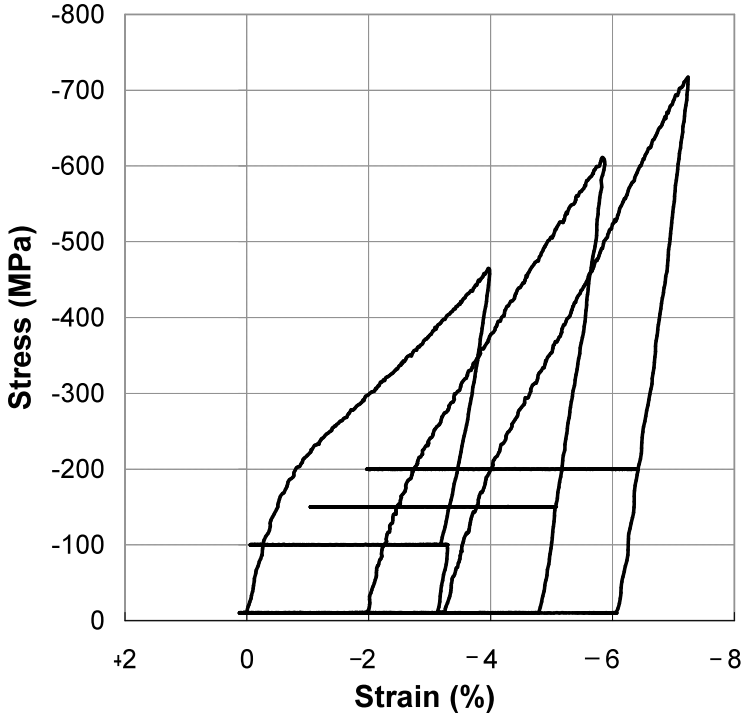

Fig. 54. Stress-strain diagram showing the detwinning by a 4% applied strain (repeatability check) followed by unloading and actuation at 100 MPa. Following the actuation the specimen is unloaded to 10 MPa and one thermal cycle is conducted to recover any remnant detwinned martensite. The loading path is then repeated with subsequent actuation cycles at 150 and 200 MPa.

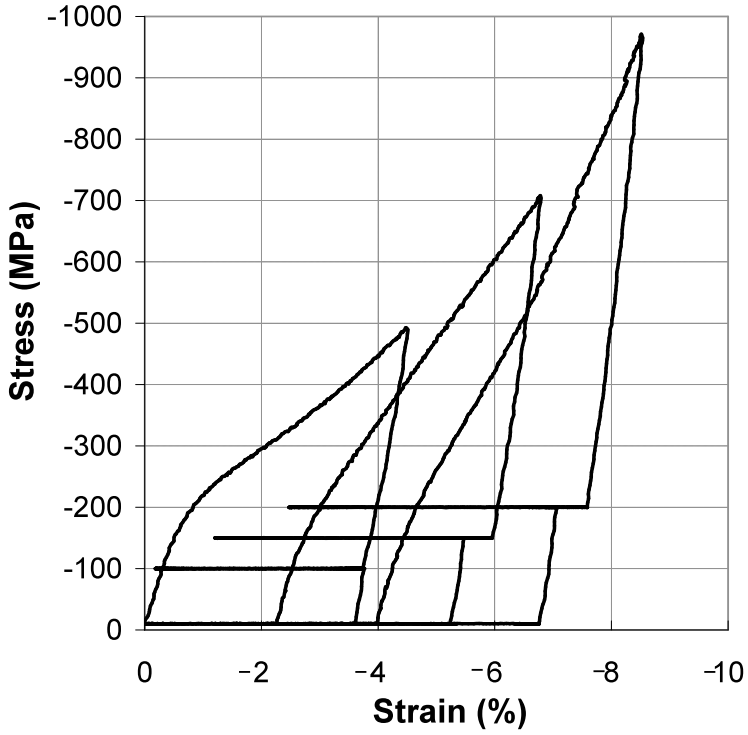

Fig. 55. Stress-strain diagram showing the detwinning by a 4.5% applied strain followed by unloading and actuation at 100 MPa. Following the actuation the specimen is unloaded to 10 MPa and one thermal cycle is conducted to recover any remnant detwinned martensite. The loading path is then repeated with subsequent actuation cycles at 150 and 200 MPa.

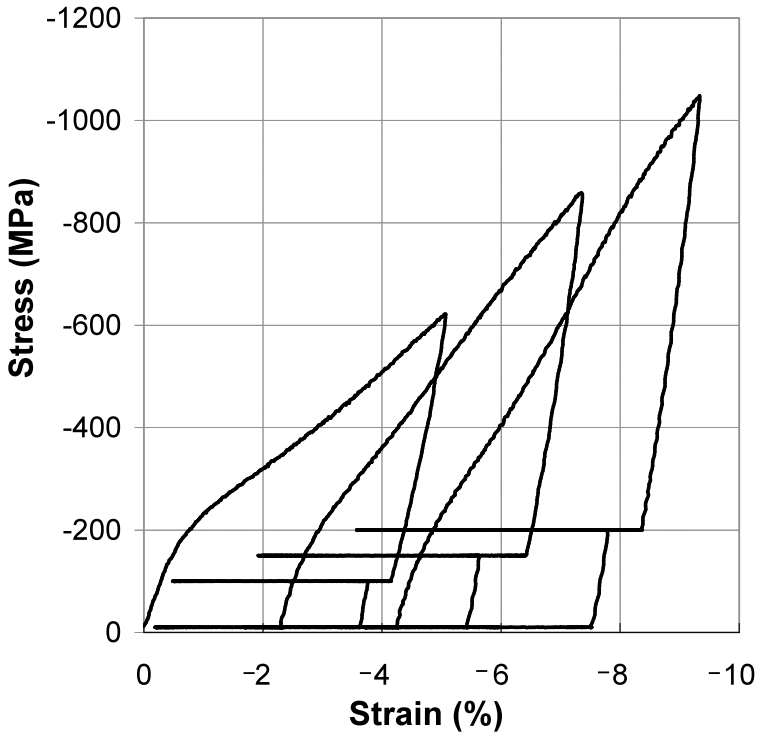

Fig. 56. Stress-strain diagram showing the detwinning by a 5% applied strain (repeatability check) followed by unloading and actuation at 100 MPa. Following the actuation the specimen is unloaded to 10 MPa and one thermal cycle is conducted to recover any remnant detwinned martensite. The loading path is then repeated with subsequent actuation cycles at 150 and 200 MPa.

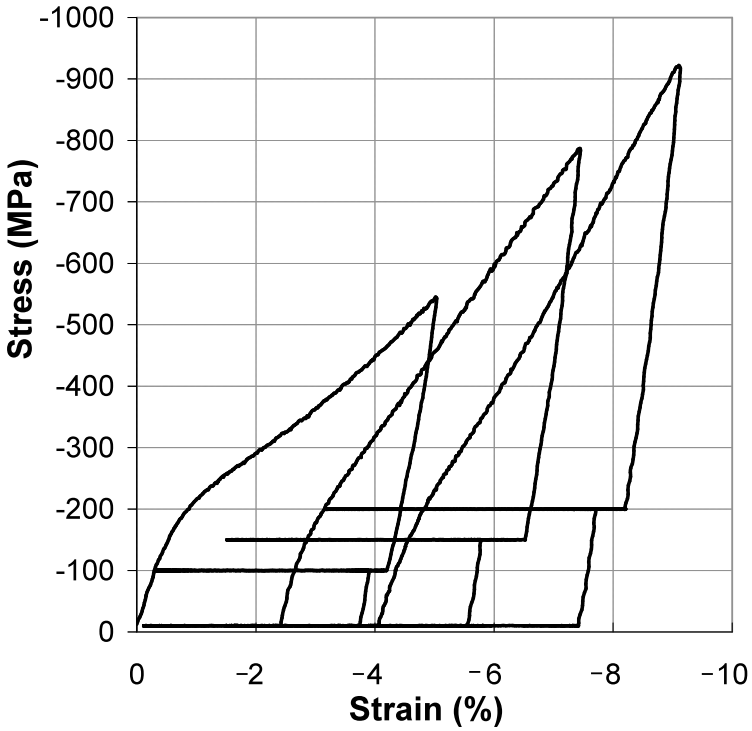

Fig. 57. Stress-strain diagram showing the detwinning by a 5% applied strain followed by unloading and actuation at 100 MPa. Following the actuation the specimen is unloaded to 10 MPa and one thermal cycle is conducted to recover any remnant detwinned martensite. The loading path is then repeated with subsequent actuation cycles at 150 and 200 MPa.

APPENDIX C

MICROGRAPHS FROM THE $TI_{50}PD_{40}NI_{10}$ HTSMA SPECIMENS

This appendix covers the additional micrographs for Chapters III and IV. Additional TEM micrographs from the specimens after the creep tests and the constant stress thermal cycling tests are shown from Chapter III. Additional optical micrographs of the as-received specimen are shown from Chapter IV.

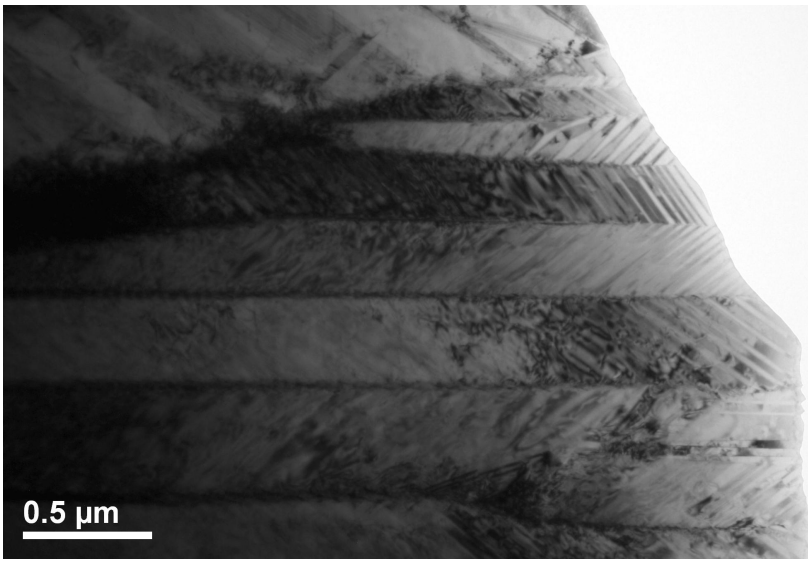

(a)

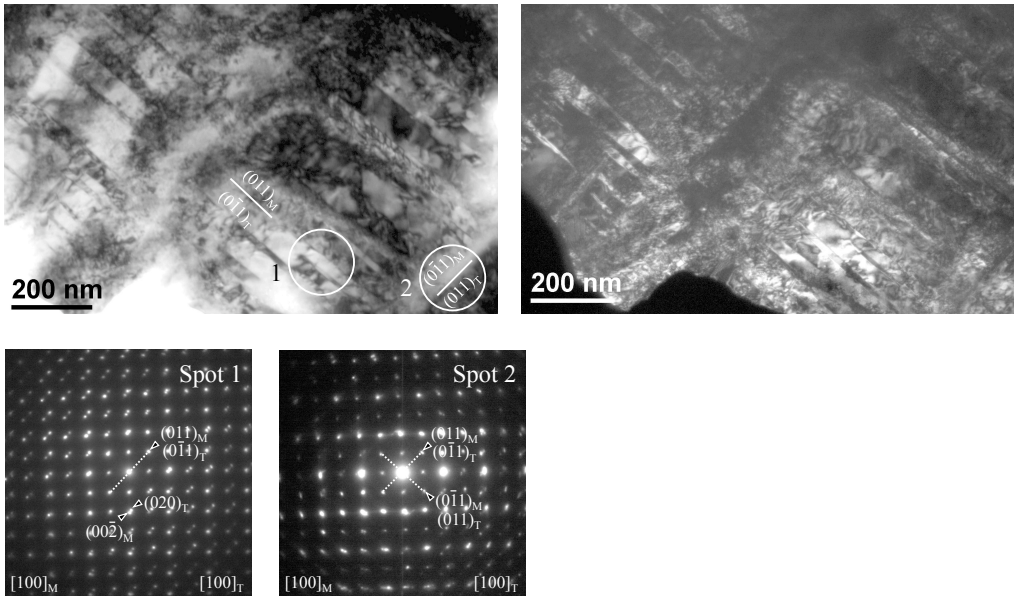

(b)

Fig. 58. TEM image of the specimen after the creep test at 200 MPa **(a)** Martensite twinning structure in the specimen; **(b)** Another region in the specimen showing {110} compound twins.

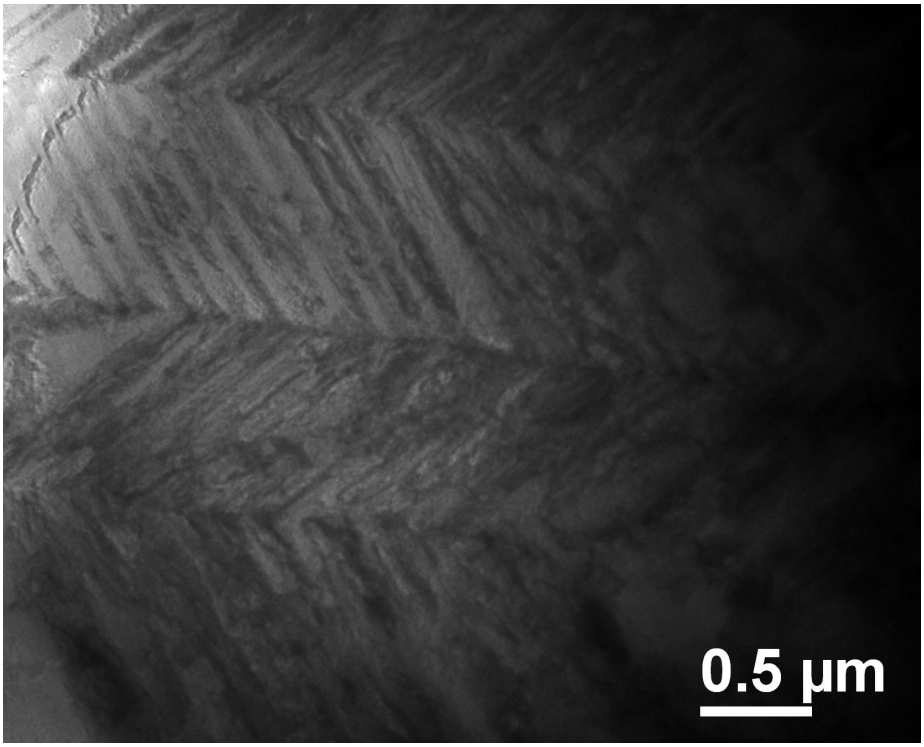

Fig. 59. 200 MPa specimen after the creep tests showing a twinning type structure even when heated to a temperature of 800°C (350°C above A_f).

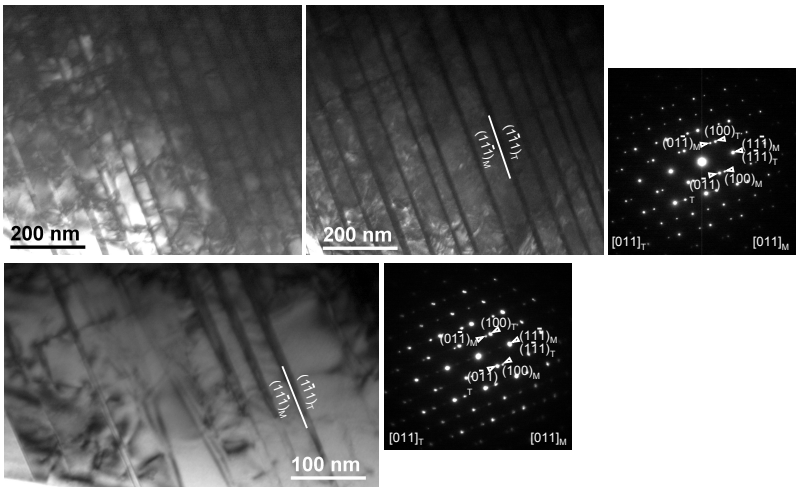

(a)

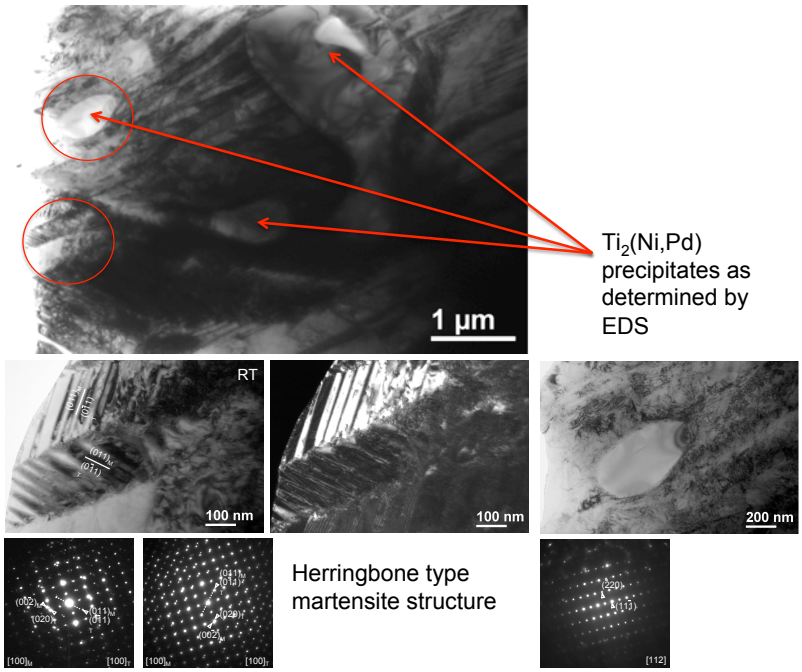

(b)

Fig. 60. TEM image of the specimen after thermal cycling at 20°C/min **(a)** {111} Type I twinning observed in regions of the specimen; **(b)** Another region in the specimen showing compound twins and $Ti_2(Pd, Ni)$ tetragonal precipitates in the specimen as determined by Electron Diffraction Spectroscopy (EDS).

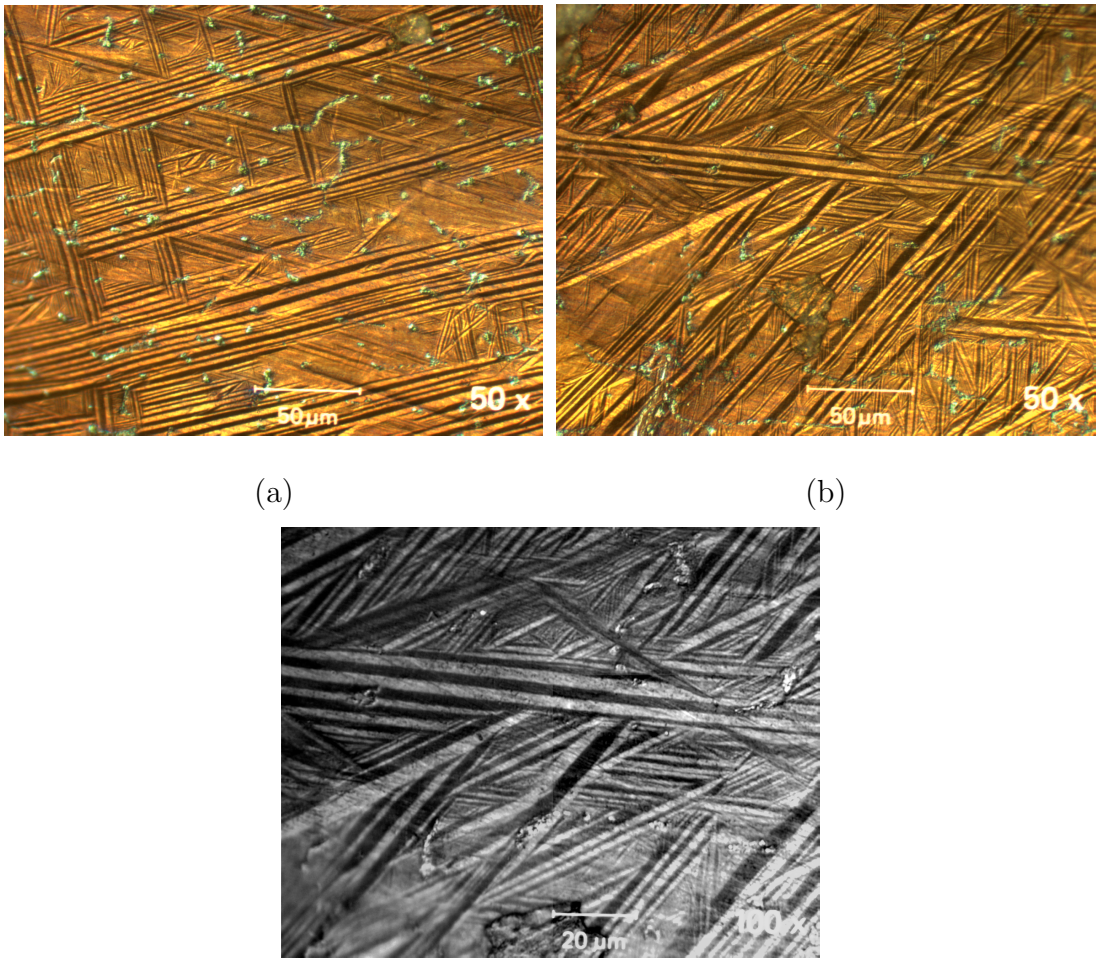

(a) (b)

(c)

Fig. 61. For Chapter IV, micrographs of the $Ti_{50}Pd_{40}Ni_{10}$ tensile HTSMA in the as-received condition **(a)** A region showing a mixture of reoriented martensite as well as small regions of self accommodated martensite; **(b)** A regions showing self accommodated martensite present predominantly in the same specimen; **(c)** A zoomed view of the self accommodated martensite from the previous figure.

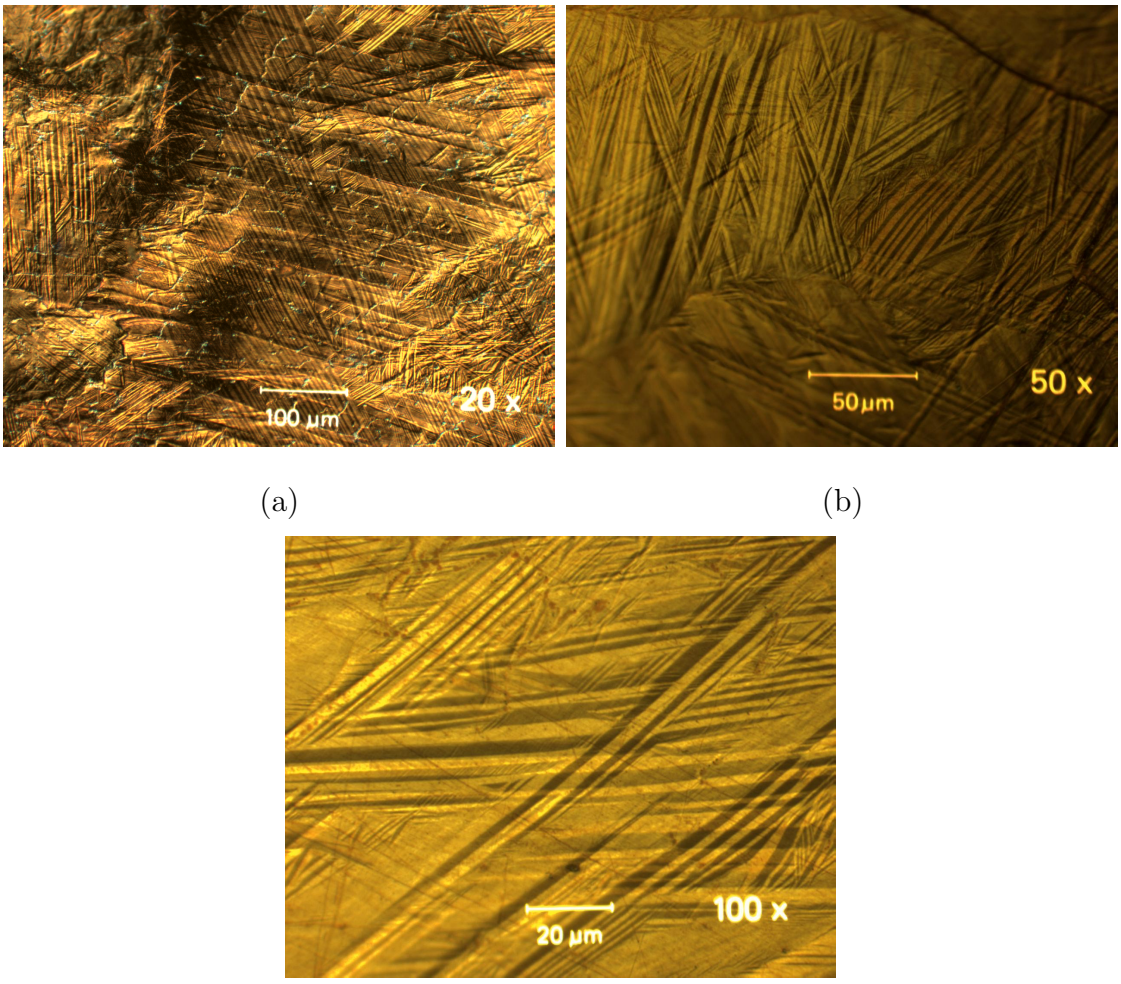

(a) (b)

(c)

Fig. 62. For Chapter IV, micrographs of the $Ti_{50}Pd_{40}Ni_{10}$ tensile HTSMA in the as-received condition **(a)** A region showing different grains with the martensite twins within them; **(b)** A more zoomed image showing the grain size of the specimen and the interaction of grain boundaries; **(c)** A closeup view of the twins some of which show significantly smaller internal twinning.

APPENDIX D

INFLUENCE OF THE HIGH OPERATING TEMPERATURE ON THE OXIDATION BEHAVIOR OF HTSMAS

One of the primary concerns with testing HTSMAs at the high test temperatures is the influence of oxidation and its impact on the actuation characteristics. The present study was conducted prior to all the thermomechanical studies conducted on the HTSMAs. For this study two rectangular specimens of a $Ti_{50}Pd_{40}Ni_{10}$ HTSMA, 10 mm x 10 mm in cross section were used. One of the rectangular specimen was in the as-cast condition while the second specimen was from the bar, hot rolled at 900°C for 1.5 hours and then furnace cooled. The time, 1.5 hours, was associated with reducing the thickness of the bar by 30%. The hot rolling process was performed at Ames laboratory. The specimens were then encased in an one inch diameter epoxy cylinder and allowed to set. The two specimens were then polished first using silicon carbide paper and subsequently using a diamond suspension liquid to a 1 micron surface finish. The specimens were then coated with a thin carbon layer to enable conduction when studied in the microprobe analysis. The specimens were analyzed in the microprobe and the composition of different regions were studied for the as-cast and the hot rolled specimen. To check if the layer formed on the hot rolled specimen was consistent with what could be observed on a similar test specimen, a 6 mm diameter x 12 mm length cylindrical specimen was heat treated in a furnace at 900°C for 1.5 hours and then furnace cooled. The new specimen diameter was then measured using a Lasermike which sent out a laser beam. By placing the specimen in the path of the laser beam, a portion of the beam was cut of and was not measure by the receiver. This measured cut off section gave the diameter of the specimen up to

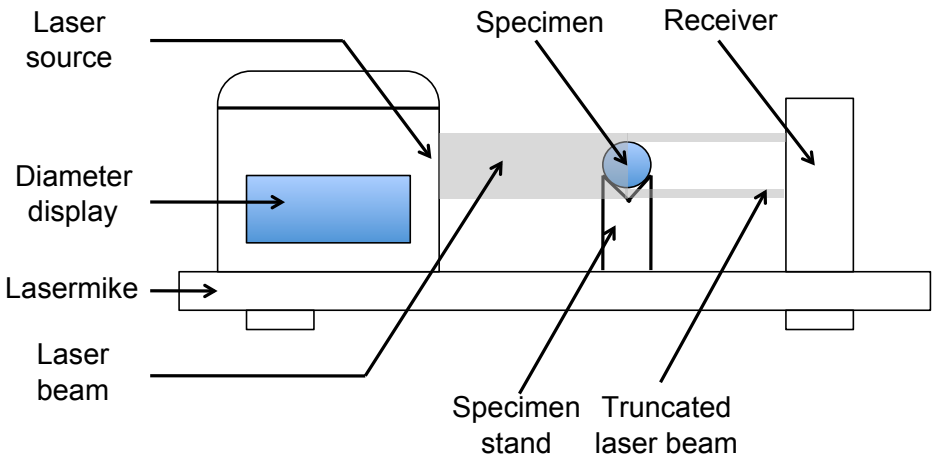

Fig. 63. A schematic illustrating the specimen setup and operation of a Lasermike measurement system.

a six decimal place accuracy. Six measurements were conducted by laterally moving and rotating the specimen on the Lasermike specimen holder to get a average change in the diameter of the specimen. A schematic of the test setup is shown in Fig. 63.

The results from the measurement of the as-cast and the hot rolled specimen compositions are shown in the two Back Scattered Electron (BSE) images Fig. 64 and Fig. 65. The different regions where measurements were taken are marked on the micrograph and the composition in these regions are listen below the micrograph. From the as-cast material BSE image (Fig. 64), it is noticed that apart from a small amount of SiO_2 present in the material surface most of the alloy has a uniform composition starting from the edge of the cast specimen. The total width of the specimen as shown in the micrograph spans 15-20 microns. The outer oxide region of the sample is approximately 1 micron thick and is shown as the black and white contrasted region on the left edge of the sample. The oxide is typically TiO_2. In the case of the rolled specimen (Fig. 65) a gradient of different layers within the edge 40

microns is observed. Different regions in each of these layers are analyzed to study the composition distribution and the effect of oxidation. The composition in the different regions of the micrograph are shown in the figure caption. It is noticed that the specimen begins with a small distribution of Ni and Ti oxide (A8) followed by a heavy distribution of almost completely pure TiO_2 which extends for approximately 20 microns into the specimen thickness (A7). Following this there are three regions (A6, A5 and A4) which show a gradient of colors and correspond to a decreasing Palladium to Nickel ratio. The composition of Titanium in these regions could not be exactly determined. Small SiO_2 precipitates were observed in certain regions (A3). After a depth of approximately 40 microns from the surface, the specimen reaches the desired matrix compositions of $Ti_{50}Pd_{40}Ni_{10}$. The distribution of each individual element in the composition was also determined by an X-ray scan over the chosen rectangular specimen surface section as shown in the micrograph in Fig. 65. The scan for different elements shows that oxygen and titanium and heavily concentrated at the TiO_2 region as expected. This is associated with the high affinity of Ti to oxygen. However the diffusion of Ti to react with oxygen leads to an almost complete absence of Titanium over the next 20 microns which is then predominantly dominated by pure Palladium or Nickel that have their own regions. This unique distribution of the elements on the surface of the specimen raised the question if the oxide diffused into the surface of the specimen or if the material diffused out to form the oxide region.

The Lasermike measurement of the heat treated specimen addressed this question. Precise measurement of the specimen diameter before and after heat treatment were conducted and the recorded values from the Lasemike are shown in Table XI. The second column shows the diameter before heat treatment. The third column shows the diameter of the specimen after heat treatment and half the difference in the diameters (i.e. the thickness) is shown in the fourth column. The average of all

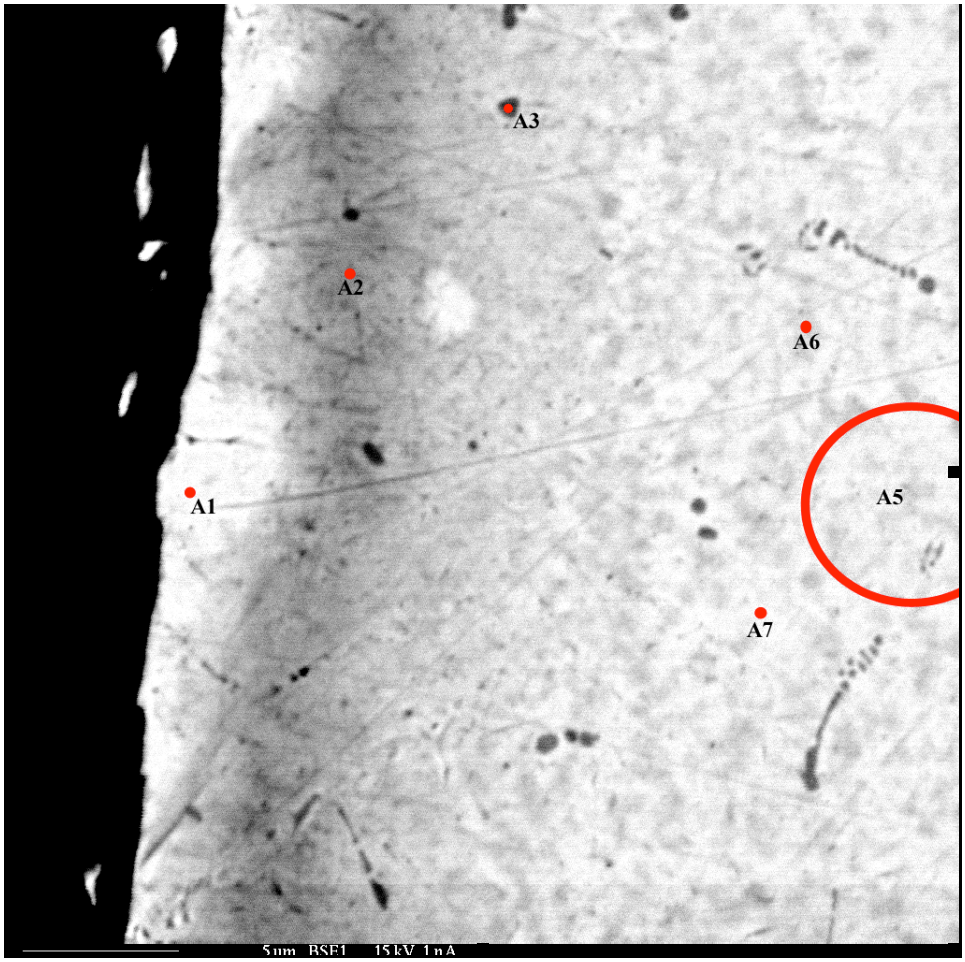

Fig. 64. Quantitative study based on Back Scattered Electron imaging technique of the as-cast TiPdNi sample. A1- TiPdNi, A2- TiPdNi (Si), A3 Ti rich precipitate, A5 TiPdNi, A6 TiPdNi (Si rich), A7 TiPdNi (Si poor).

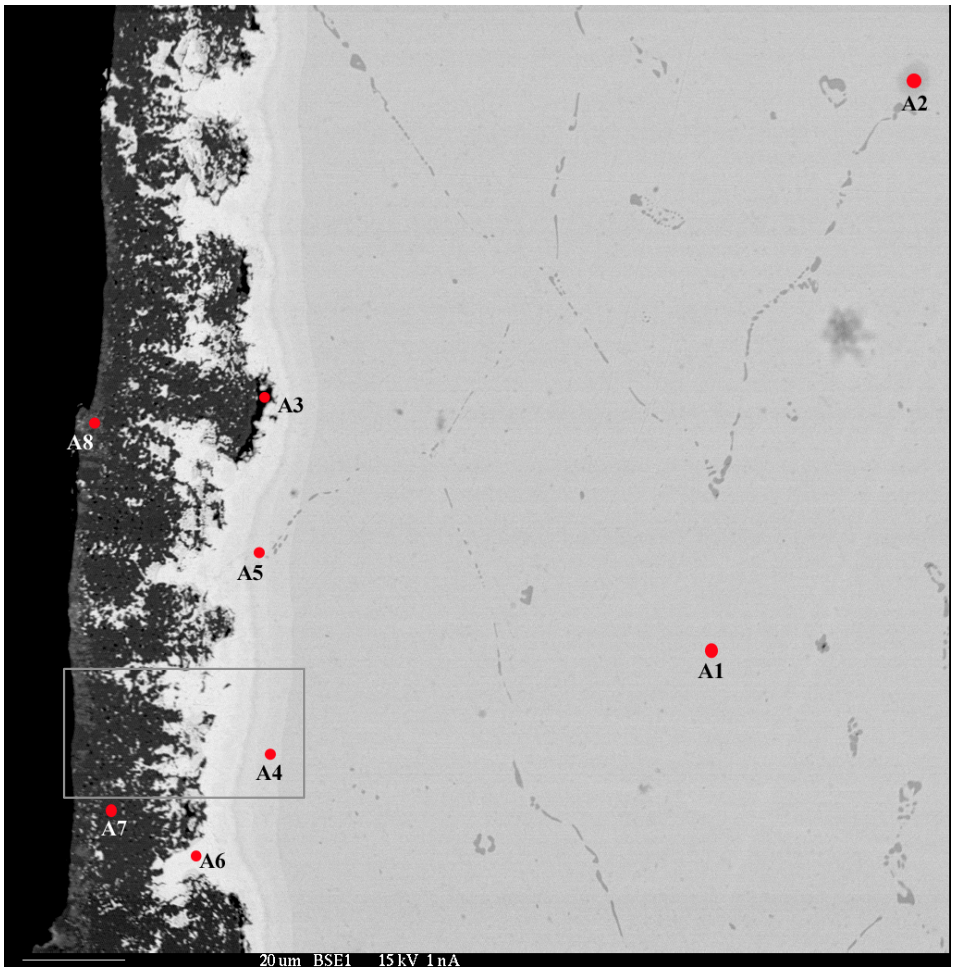

Fig. 65. Quantitative study based on Back Scattered Electron imaging technique of the rolled TiPdNi sample. A1- TiPdNi, A2- TiPdNi (O), A3 SiO2 precipitate, A4 Ti-60PdNi, A5 Ti-65PdNi, A6 Ti-90PdNi, A7 TiO2, A8 (Ti,Ni)O.

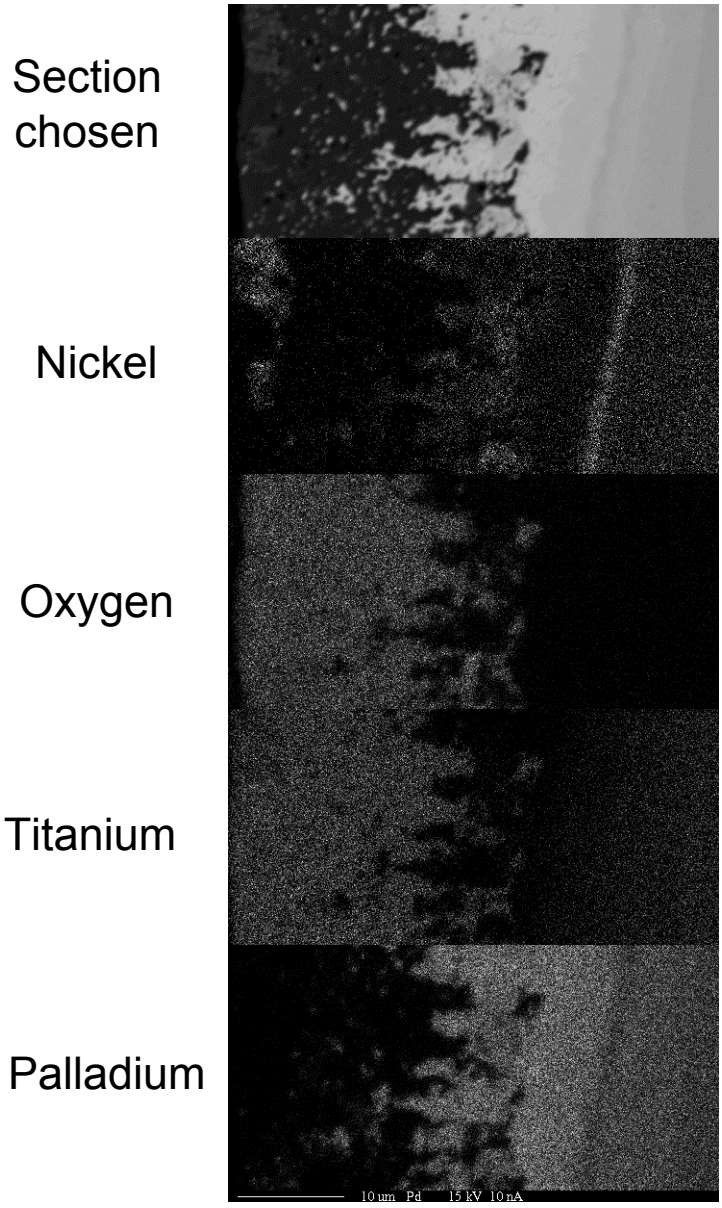

Fig. 66. Quantitative study based on Back Scattered Electron imaging technique of the rolled TiPdNi sample. A1- TiPdNi, A2- TiPdNi (O), A3 SiO2 precipitate, A4 Ti-60PdNi, A5 Ti-65PdNi, A6 Ti-90PdNi, A7 TiO2, A8 (Ti,Ni)O.

the thicknesses (ignoring the 3rd value) is 0.02363 mm. This shows that the specimen thickness has increase by approximately 20 micron, equivalent to the thickness of the TiO_2 layer as seen in Fig. 65. This suggests the the Titanium diffuses out of the matrix, reacts with oxygen to form the titanium-oxide layer on the surface. A consequence of this is depleted titanium in the matrix over the next 20 micron. For the tests conducted in the current work, the effect of oxidation is not of significant concern due to the relatively large specimen size and the maximum temperature exposed too. However the effects of oxidation must be considered when use of thin strips or wire HTSMAs for actuation applications.

Table XI. Diameters recorded from the Lasermike measurements. All dimensions are in mm.

Reading	Dia. before	Dia. after	Thickness
1	3.321338	3.3922631	0.035462633
2	3.290087	3.3366964	0.0233045
3	3.323844	3.3296352	0.0028956
4	3.317562	3.3908238	0.0366310
5	3.286557	3.3378394	0.0256413
6	3.322726	3.3584134	0.0178435

APPENDIX E

DATA FROM THE STUDY OF THE CYCLIC ACTUATION BEHAVIOR OF $TI_{50}PD_{40}NI_{10}$ HTSMA IN TENSION

The stress-strain data and the strain temperature data from the actuation under the applied stress and at 10 MPa is shown for all the test cases listed in Table XII.

Table XII. Test matrix for parametric study on the effect of total applied stress and applied strain on the transformation behavior.

Pre-strain	Applied stress	# of thermal cycles	Cut direction
-	100 MPa	10	Transverse
-	200 MPa	10	Transverse
4.0%	150 MPa	10	Transverse
5.0%	150 MPa	10	Transverse
-	150 MPa	10	Rolling

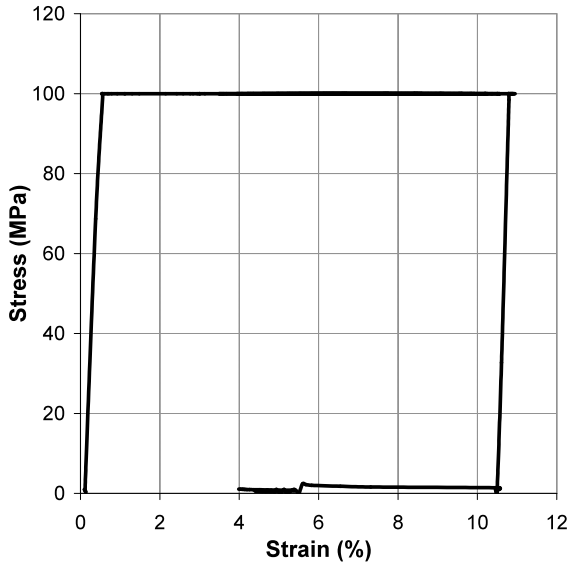

Fig. 67. Stress-strain diagram for the thermal cycling under a constant stress of 100 MPa and subsequent thermal cycling under 10 MPa.

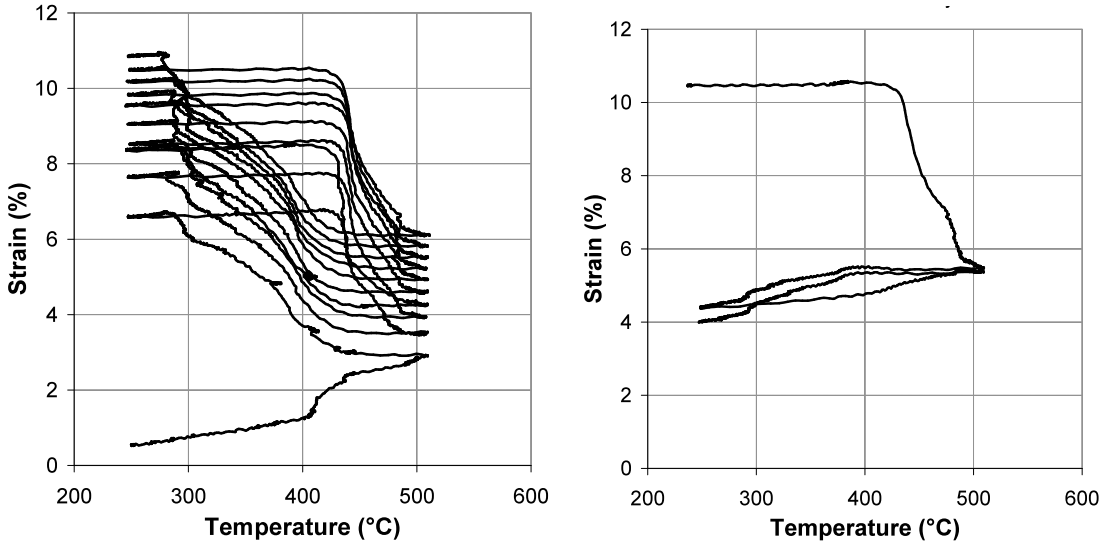

(a) (b)

Fig. 68. Strain-temperature diagram for the thermal cycling **(a)** at 100 MPa. **(b)** at 10 MPa.

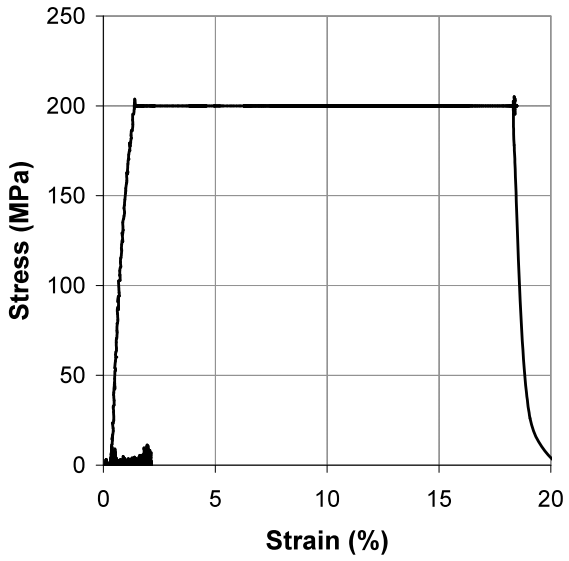

Fig. 69. Stress-strain diagram for the thermal cycling under a constant stress of 200 MPa and subsequent thermal cycling under 10 MPa.

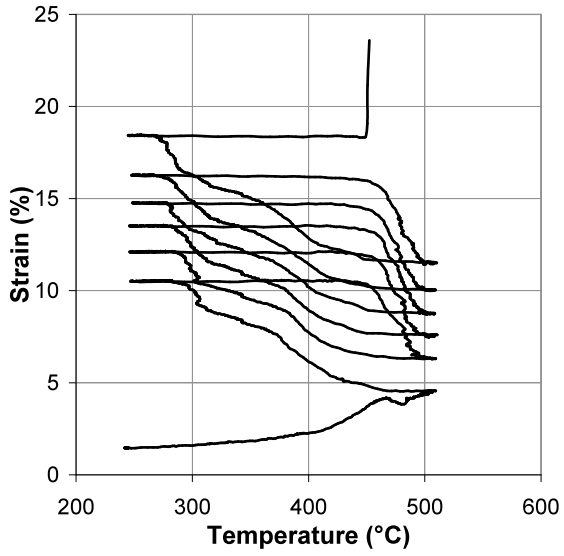

Fig. 70. Strain-temperature diagram for the thermal cycling at 200 MPa. The specimen fails after 7 thermal cycles.

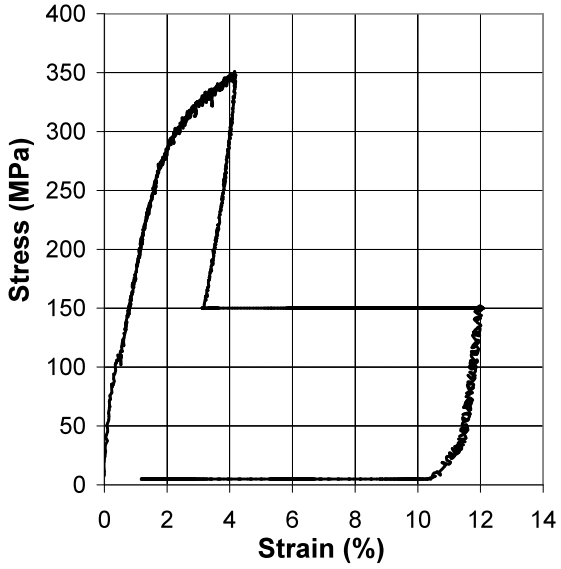

Fig. 71. Stress-strain diagram showing the detwinning to 4% strain followed by unloading and thermal cycling under a constant stress of 150 MPa. The specimen was subsequently unloaded and thermally cycled under 10 MPa.

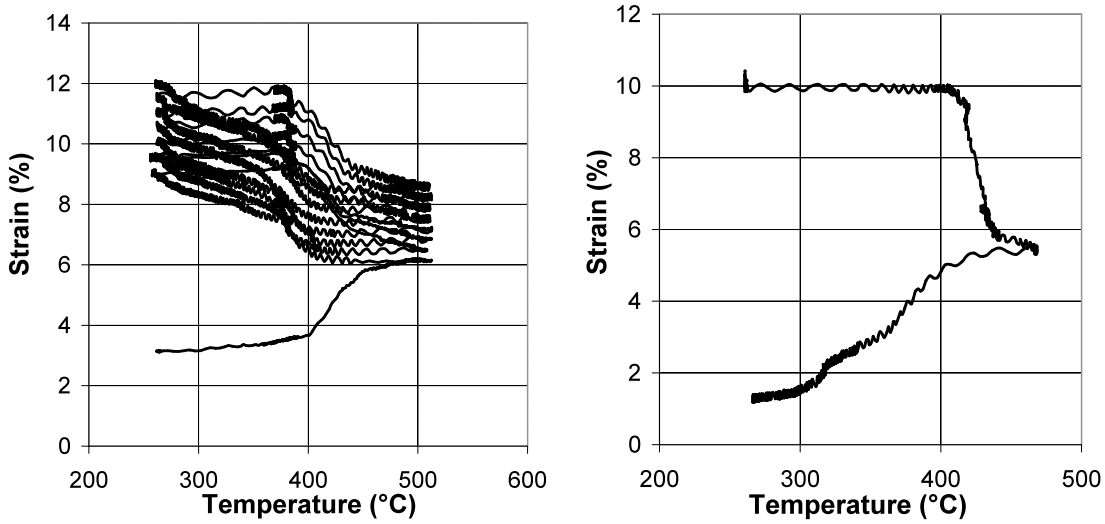

(a) (b)

Fig. 72. Strain-temperature diagram for the thermal cycling (after the 4% applied detwinning) **(a)** at 150 MPa. **(b)** at 10 MPa.

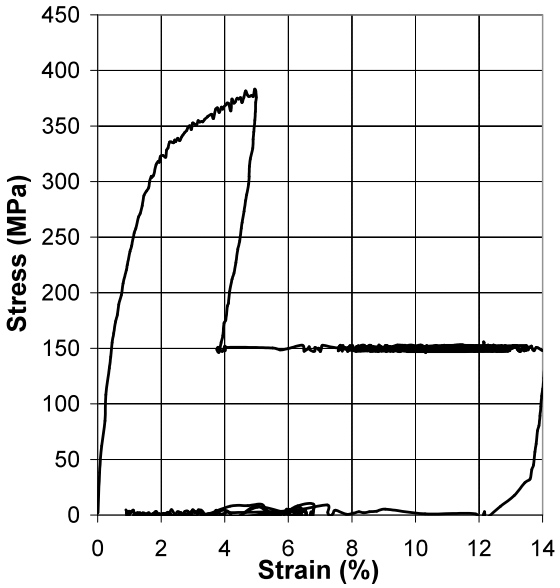

Fig. 73. Stress-strain diagram showing the detwinning to 5% strain followed by unloading and thermal cycling under a constant stress of 150 MPa. The specimen was subsequently unloaded and thermally cycled under 10 MPa.

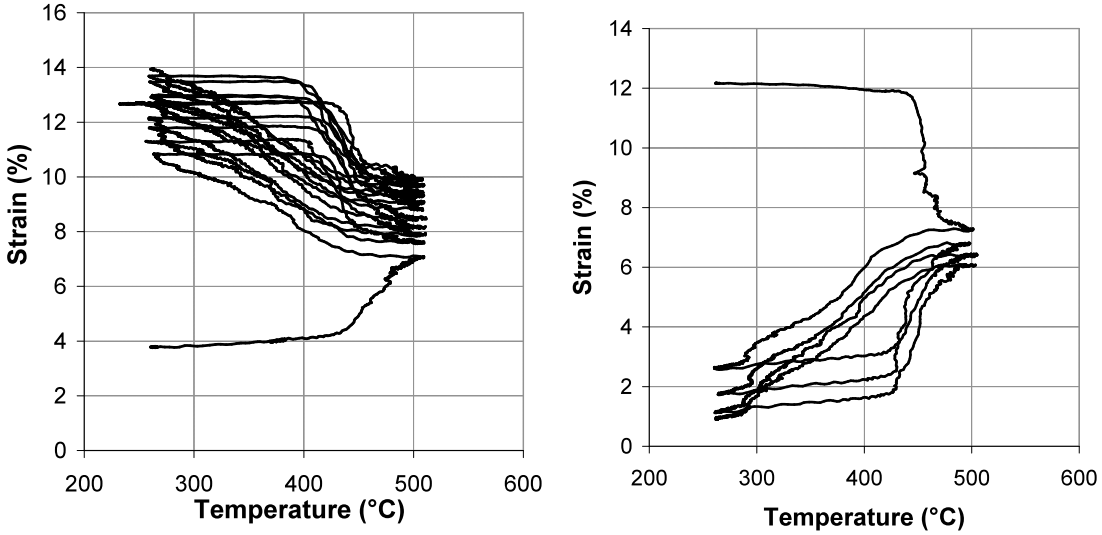

(a) (b)

Fig. 74. Strain-temperature diagram for the thermal cycling (after the 5% applied detwinning) **(a)** at 150 MPa. **(b)** at 10 MPa.

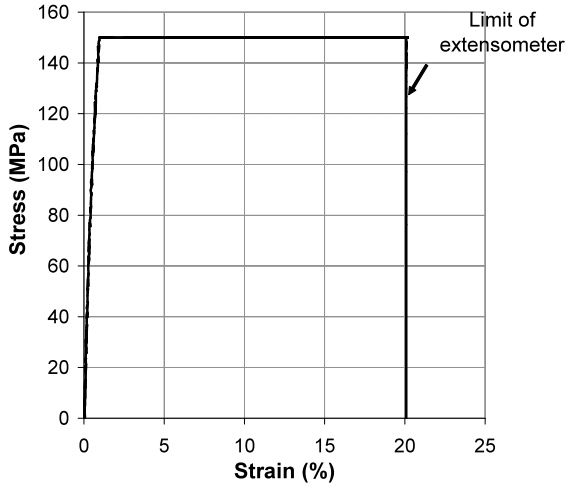

Fig. 75. Stress-strain diagram for the thermal cycling under a constant stress of 150 MPa and subsequent thermal cycling under 10 MPa stress. This specimen was cut along the rolling direction.

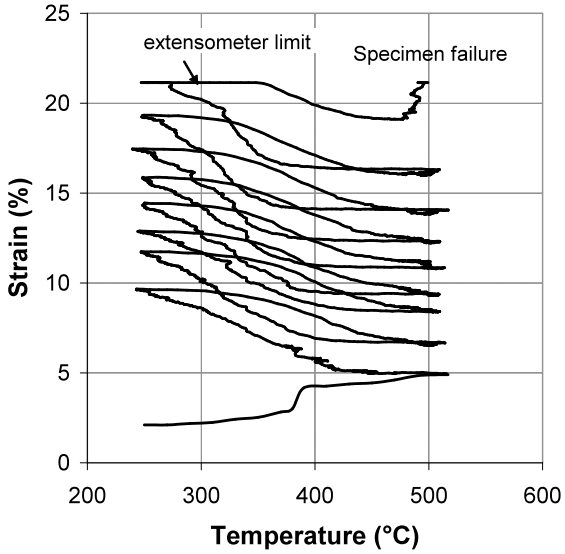

Fig. 76. Strain-temperature diagram for the thermal cycling at 150 MPa. The specimen fails after 7 thermal cycles.

VITA

Parikshith K. Kumar is the son of G. Krishna Kumar and Shanti Krishna Kumar, and brother to Prathima Kumar. He was raised in Chennai, India where he attended Madras University and completed his B.E. in mechanical engineering. He then enrolled in the graduate program of aerospace engineering at Texas A&M University, completed his M.S. in May of 2005 and continued to pursue - to receive his Ph.D. under the guidance of Dr. Dimitris C. Lagoudas. His research interests include thermomechanical and microstructural testing and characterization of SMAs and HTSMAs. An extended resume can be found at http://smart.tamu.edu. Mr. Kumar can be reached at his permanent address:

Department of Aerospace Engineering H.R. Bright Building, Rm. 701, Ross Street - TAMU 3141 College Station TX 77843-3141
His email address is parik@tamu.edu.

The typist for this dissertation was Parikshith K. Kumar.